Pro gradu -tutkielma, geofysiikka
Examensarbete, geofysik
Master's thesis, Geophysics

# 3D-modeling of snow in the Saariselkä region during the winter 2015-2016

Arttu Jutila
2017

Ohjaaja | Handledare | Supervisor
Matti Leppäranta

Tarkastajat | Examinatorer | Examiners
Matti Leppäranta
Ivan Mammarella

HELSINGIN YLIOPISTO
FYSIIKAN LAITOS

HELSINGFORS UNIVERSITET
INSTITUTIONEN FÖR FYSIK

UNIVERSITY OF HELSINKI
DEPARTMENT OF PHYSICS

HELSINGIN YLIOPISTO — HELSINGFORS UNIVERSITET — UNIVERSITY OF HELSINKI

| Tiedekunta/Osasto — Fakultet/Sektion — Faculty | Laitos — Institution — Department |
|---|---|
| Faculty of Science | Department of Physics |

Tekijä — Författare — Author
Arttu Jutila

Työn nimi — Arbetets titel — Title
3D-modeling of snow in the Saariselkä region during the winter 2015-2016

Oppiaine — Läroämne — Subject
Geophysics

| Työn laji — Arbetets art — Level | Aika — Datum — Month and year | Sivumäärä — Sidoantal — Number of pages |
|---|---|---|
| Master's thesis | April 2017 | 68 + 7 |

Tiivistelmä — Referat — Abstract

Studying and modelling the snow distribution processes is important because snow influences the ground, flora, and fauna by affecting among other things the energy balance both in large and small scales and the near-surface atmospheric conditions due to its highly reflective and insulating properties.

The aim of the study was to use the spatially distributed high-resolution snow-evolution modelling system SnowModel to simulate the snow conditions in winter 2015–2016 in the Saariselkä region in Northern Finland and assess the model's performance. SnowModel has not been used to study a domain in Finland before, and the model gives information about variables that are hardly measured in Finland, such as snow sublimation.

The simulations were first run without snow water equivalent assimilation and then assimilating the available snow water equivalent (SWE) observations. The simulation results show that in the default mode the model needs assimilation and SWE observations, preferably more frequent observations towards the spring, to produce physically sensible results. The domain averaged simulated end-of-winter maximum SWE value of 220 mm was reached on 21 April 2016. The simulated SWE patterns match with known elevation and vegetation dependencies. Timing of the first snow, the beginning of the snow season and the end-of-winter SWE are simulated well, whereas the melt and the snowfree date depend on the amount of snow. The assimilation run suggests that the needed summed precipitation is as much as 18 % larger than the observed increasing towards the northeast. Similarly, the simulated summed melt reaches locally up to 70 % larger values compared to the non-assimilation run. Blowing-snow sublimation takes place in open areas and its simulated summed value is up to 27 mm. Simulated static-surface sublimation varies between 4-22 mm. The simulated sublimation from the canopy-intercepted snow peaks at 110 mm. Up to 16 % of the precipitation is returned to the atmosphere by sublimation.

The simulation results could be improved by utilizing more detailed data of the study domain and modifying the hard-coded variables to suit the surroundings, which could in turn decrease the need for assimilating SWE observations.

Avainsanat — Nyckelord — Keywords
modeling, snow distribution, snow water equivalent, snow sublimation

Säilytyspaikka — Förvaringsställe — Where deposited
Kumpula Campus Library

Muita tietoja — övriga uppgifter — Additional information

HELSINGIN YLIOPISTO — HELSINGFORS UNIVERSITET — UNIVERSITY OF HELSINKI

| | |
|---|---|
| Tiedekunta/Osasto — Fakultet/Sektion — Faculty<br>Matemaattis-luonnontieteellinen tiedekunta | Laitos — Institution — Department<br>Fysiikan laitos |

Tekijä — Författare — Author

Arttu Jutila

Työn nimi — Arbetets titel — Title

3D-modeling of snow in the Saariselkä region during the winter 2015-2016

Oppiaine — Läroämne — Subject

Geofysiikka

| | | |
|---|---|---|
| Työn laji — Arbetets art — Level<br>Pro gradu -tutkielma | Aika — Datum — Month and year<br>Huhtikuu 2017 | Sivumäärä — Sidoantal — Number of pages<br>68 + 7 |

Tiivistelmä — Referat — Abstract

Lumen alueelliseen jakautumiseen liittyvien prosessien tutkiminen ja mallintaminen on tärkeää, sillä lumi vaikuttaa suuren heijastavuutensa ja pienen lämmönjohtokykynsä avulla maankamaraan, kasveihin ja eläimiin muun muassa suuren ja pienen skaalan energiataseen kautta sekä muokkaamalla pinnanläheisen ilmakehän olosuhteita.

Tutkimuksen tavoitteena oli tarkkaa spatiaalista SnowModel-lumimallisysteemiä käyttämällä simuloida talven 2015–2016 lumioloja Saariselän alueella Pohjois-Suomessa ja arvioida mallin sopivuutta kyseisiin olosuhteisiin. SnowModelia ei ole aiemmin käytetty Suomessa sijaitsevan tutkimusalueen simulointiin, mutta malli antaa tietoja sellaisista suureista, joita Suomessa harvoin mitataan, kuten lumen sublimaatiosta.

Ensimmäinen simulaatio tehtiin ilman lumen vesiarvojen assimilointia ja toinen lumen vesiarvohavainnot assimiloiden. Tulokset osoittavat että oletusarvoisia käyttäjän määrittämiä muuttujia käytettäessä malli tarvitsee assimilointia ja lumen vesiarvohavaintoja, mieluiten tihenevästi kevättä kohti, jotta tulokset olisivat fysikaalisesti mielekkäitä. Tutkimusalueella simuloidun lumen vesiarvon aluekeskiarvo saavutti maksiminsa 220 mm 21.4.2016. Lumen vesiarvon jakautuminen noudattaa tunnettuja maastonkorkeus- ja kasvillisuusriippuvuuksia. Ensilumen, pysyvän lumen alkamisen ja lumen vesiarvon maksimin ajoitus mallintuu hyvin, mutta sulaminen riippuu lumen määrästä. Assimilaatiomallinnuksen mukaan jopa 18 % suurempi vuosisadanta tarvitaan havaittujen lumiolosuhteiden toistamiseksi, ja sadanta kasvaa kohti tutkimusalueen koillisosia. Vastaavasti vuosisulanta on assimilaatiomallinnuksessa enintään 70 % suurempi kuin ilman assimilaatiota. Lumituiskusta sublimoituu lunta aukeilla alueilla yhteensä enintään 27 mm vuoden aikana, kun taas lumipeitteen pinnalta simulaation mukaan sublimoituu 4-22 mm. Puihin interseptoituneesta lumesta simulaatiossa sublimoituu yhteensä jopa 110 mm. Yhteensä sadannasta enintään 16 % sublimoituu takaisin ilmakehään.

Mallin tuloksia voisi parantaa keräämällä yksityiskohtaisempaa dataa tutkimusalueelta ja muokkaamalla malliin koodattuja muuttujia ja vakioita olosuhteisiin sopiviksi, jolloin tarve assimiloida lumen vesiarvoja voisi vuorostaan vähentyä.

Avainsanat — Nyckelord — Keywords

mallinnus, lumen alueellinen jakautuminen, lumen vesiarvo, lumen sublimaatio

Säilytyspaikka — Förvaringsställe — Where deposited

Kumpulan kampuskirjasto

Muita tietoja — övriga uppgifter — Additional information

# Contents

# List of figures

# List of tables

# List of symbols and acronyms

| | |
|---|---|
| $a$ | Canopy flow index |
| $\alpha_p$ | Snow particle albedo |
| $\alpha_s$ | Surface albedo |
| $\alpha_{sf}$ | Albedo for melting snow under forest canopy |
| $\alpha_{snf}$ | Albedo for melting snow in non-forested areas |
| AWS | Automatic weather station |
| $\beta$ | Terrain slope |
| $C_e$ | Canopy exposure coefficient |
| $\chi$ | Precipitation adjustment factor |
| $C_p$ | Specific heat of air |
| $C_v$ | Vegetation snow holding capacity |
| $D$ | Diffusivity of atmospheric water vapour |
| $d$ | Julian Day |
| $D_e$ | Exchange coefficient for latent heat |
| $\delta$ | Solar declination angle |
| $D_h$ | Exchange coefficient for sensible heat |
| $d_r$ | Day of summer solstice |
| $d_y$ | Average number of days in a year |
| $\eta$ | Curvature length scale |
| $e$ | Atmospheric vapour pressure |
| $e_0$ | Vapour pressure of surface |
| $\varepsilon_0$ | Surface emissivity |
| $\varepsilon_a$ | Atmospheric emissivity |
| $e_s$ | Saturation vapour pressure |
| $f$ | Equilibrium-fetch distance |
| $F_c$ | Canopy fraction |
| FMI | Finnish Meteorological Institute |
| $F_s$ | Depth-fraction of vegetation covered by snow |
| $G$ | Canopy gap fraction |
| $g$ | Gravitational acceleration |
| $\Gamma$ | Air temperature lapse rate |
| $\Gamma_d$ | Dewpoint temperature lapse rate |
| $\Gamma_{RH}$ | Relative humidity offset |
| $\gamma_c$ | Topographic curvature weighting factor |
| $\gamma_s$ | Topographic slope weighting factor |
| $H$ | Atmospheric scale height |
| $h$ | Hour of the day |
| $h_*$ | Saltation layer height |
| $h_c$ | Canopy height |
| $h_w$ | Snow water equivalent |

| | |
|---|---|
| $h_w^*$ | Weight of snow |
| $I$ | Canopy-intercepted load |
| $i$ | Angle between the slope normal and the direct solar radiation |
| $k$ | Vegetation-dependent extinction coefficient |
| $\kappa$ | von Kármán's constant |
| $k_{eff}$ | Effective thermal conductivity |
| $\mathrm{LAI}^*$ | Effective leaf area index |
| $\lambda$ | Vapour pressure coefficient |
| $\lambda_t$ | Thermal conductivity of the atmosphere |
| $L_f$ | Latent heat of freezing |
| $L_m$ | Melt-unloading rate |
| $L_s$ | Latent heat of sublimation |
| $M$ | Model simulated melt |
| $m$ | Particle mass |
| $M_{assim}$ | Melt required to simulate the observations |
| $\bar{m}$ | Mean particle mass |
| $M_{fact}$ | Melt correction factor |
| $M_p$ | Potential snow melt |
| $\mu$ | Solar azimuth |
| $M_w$ | Molecular weight of water |
| Nu | Nusselt number |
| $\Omega_c$ | Curvature |
| $\Omega_s$ | Slope in the direction of the wind |
| $P$ | Water-equivalent precipitation rate |
| $p_0$ | Reference sea level pressure |
| $p_a$ | Atmospheric pressure |
| $P_{assim}$ | Precipitation forcing required to simulate the observations |
| $P_{fact}$ | Precipitation adjustment factor |
| $\phi$ | Latitude |
| $\phi$ | Mass concentration distribution |
| $\phi^*$ | Concentration scaling parameter |
| $\phi_r$ | Mass concentration of the turbulent-suspension layer at reference level |
| $\phi_s$ | Mass concentration of the saltation layer |
| $\phi_T$ | Latitude of the Tropic of Cancer |
| $\phi_t$ | Mass concentration of the turbulent-suspension layer |
| $P_r$ | Interpolated station precipitation |
| $P_s$ | Snow precipitation |
| $\Psi$ | Sublimation-loss rate coefficient |
| $\Psi_{dif}$ | Diffuse net sky transmissivity |
| $\Psi_{dir}$ | Direct net sky transmissivity |
| $\Psi_s$ | Sublimation-loss rate coefficient of the saltation layer |
| $\Psi_t$ | Sublimation-loss rate coefficient of the turbulent-suspension layer |
| $Q_c$ | Conductive energy transport |
| $Q_{cs}$ | Sublimation of canopy-intercepted snow |
| $Q_e$ | Turbulent exchange of latent heat |
| $Q_h$ | Turbulent exchange of sensible heat |
| $Q_{le}$ | Emitted longwave radiation |
| $Q_{li}$ | Incoming longwave radiation |
| $Q_{lif}$ | Incoming longwave radiation underneath the forest canopy |

| | |
|---|---|
| $Q_m$ | Energy flux available for melt |
| $Q_p$ | Solar radiation absorbed by a snow particle |
| $Q_{salt}$ | Mass-transport rate of saltation |
| $Q_{si}$ | Incoming solar radiation |
| $Q_{sif}$ | Incoming solar radiation underneath the forest canopy |
| $Q_{turb}$ | Mass-transport rate of turbulent-suspended snow |
| $Q_v$ | Sublimation rate of transported snow |
| $R$ | Universal gas constant |
| $r$ | Radius of a spherical ice particle |
| $\bar{r}$ | Mean radius of a particle |
| $R_d$ | Gas constant for dry air |
| Re | Reynolds number |
| $\rho_a$ | Air density |
| $\rho_i$ | Ice density |
| $\rho_{ns}$ | New snow density |
| $\rho_s$ | Snow density |
| $\rho_v$ | Saturation density of water vapour |
| $\rho_w$ | Water density |
| $\rho_{wo}$ | Wind-related density offset |
| RH | Relative humidity |
| Ri | Bulk Richardson number |
| $R_{melt}$ | Relative contribution of melt |
| $R_{prec}$ | Relative contribution of precipitation |
| $S^*$ | Solar constant |
| Sh | Sherwood number |
| $\sigma$ | Stefan-Boltzmann constant |
| $\sigma_c$ | Cloud-cover fraction |
| $\sigma_r$ | Atmospheric undersaturation of water vapour at the height of the relative humidity observations |
| $\sigma_s$ | Snow hardness |
| $\sigma_{us}$ | Atmospheric undersaturation of water vapour with respect to ice |
| $S_p$ | Potential snow sublimation |
| SWE | Snow water equivalent |
| SYKE | Finnish Environmental Institute |
| $t$ | Time |
| $T_0$ | Surface temperature |
| $T_a$ | Air temperature |
| $\tau$ | Hour angle measured from local solar noon |
| $\tau_v$ | Fraction of incoming solar radiation transmitted through the forest canopy |
| $T_c$ | Canopy temperature |
| $T_d$ | Dewpoint temperature |
| $T_f$ | Freezing temperature of water |
| $T_g$ | Temperature at the snow-ground interface |
| $\theta$ | Wind direction |
| $\theta_d$ | Wind direction diverting factor |
| $\theta_t$ | Terrain-modified wind direction |
| $T_r$ | Air temperature at reference height |
| $T_s$ | Snow temperature |
| $T_{stn}$ | Station air temperature |
| $T_{wb}$ | Wet-bulb temperature |
| $u$ | Zonal wind component |

| | |
|---|---|
| $u_*$ | Wind-shear velocity |
| $u_{*t}$ | Threshold surface shear velocity |
| $u_c$ | Wind speed under the canopy |
| $u_p$ | Horizontal particle velocity within the saltation layer |
| $v$ | Kinematic viscosity of air |
| $u_r$ | Wind speed at reference height |
| UTC | Coordinated Universal Time |
| UTM | Universal Transverse Mercator |
| $v$ | Meridional wind component |
| $V_s$ | Ventilation velocity of the saltation layer |
| $V_t$ | Ventilation velocity of the turbulent-suspension layer |
| $V_v$ | Ventilation velocity |
| $W$ | Wind speed |
| $\bar{w}$ | Mean terminal-fall velocity of suspended snow |
| $w_f$ | Fall velocity of a particle |
| $W_t$ | Terrain-modified wind speed |
| $w_t$ | Interpolation weighting factor |
| $W_w$ | Wind weighting factor |
| $x$ | Horizontal east coordinate |
| $\xi_s$ | Terrain slope azimuth |
| $y$ | Horizontal north coordinate |
| $Z$ | Solar zenith angle |
| $z$ | Vertical coordinate/topographic height |
| $z_0$ | Surface roughness length |
| $\zeta$ | Non-dimensional stability function |
| $\zeta_s$ | Snow depth |
| $z_r$ | Reference height |
| $z_{RH}$ | Height of the relative humidity observations |
| $z_{stn}$ | Station elevation |
| $z_t$ | Turbulent-suspension layer height |
| $z_W$ | Height of the wind observations |

# Chapter 1

# Introduction

I have always been fascinated by snow: how it sounds under one's shoe, its uniqueness, and its beautifying, illuminating and cleansing effect on nature. Not until my university studies did I realise the profound complexity of snow, and how little about it is actually understood. One of the topics I became most curious about was the wind-induced blowing snow.

A loose and dry snow particle 1-2 mm in diameter can already be picked up from the snow surface by rather light winds speeds, about 2 m $s^{-1}$. Two distinct layers are found in blowing snow. Closest to the surface is a *saltation* layer, approximately 5 cm thick, where snow particles frequently impact back to the surface due to gravity. The impact loosens more particles, and the process continues. Most of the mass transport occurs in the saltation layer. Above the saltation layer is a *turbulent-suspension* layer, which is a two-phase mixture of air and snow particles. The layers are coupled, and there is turbulent suspension provided that saltation is occurring. When airborne, the snow particles interact with the atmosphere and sublimate. (McKay and Gray, 1981; Kind, 1981; Liston, 1991).

Studying the physics of blowing and drifting snow or some parts of the process started properly and extensively in the 1960s. Reviews of those studies can be found for example in Mellor (1965, 1970); Kind (1981), and Schmidt (1982a). One of the first modelling efforts for blowing snow was by Finney (1934), who used sawdust and flake mica in wind tunnels. Tabler (e.g. 1975; 1980) has developed empirical models on snowdrift profiles. For quite some time the blowing snow research was mainly observational until the computational models started to become more common, e.g. Berg and Caine (1975) and Berg (1986). (Kind, 1981; Liston, 1991) In the 1990s Liston started developing his models, which include the models that are today known as SnowModel and MicroMet. Those two models are widely used around the world in snow covered regions and they also form the core of this study. Other modern blowing snow models are for example the Prairie and Distributed Blowing Snow Models (PBSM and DBSM, respectively) by Pomeroy et al. (1993, 1997), the many versions of PIEKTUK by Déry and Yau (2001), and the Alpine3D by Lehning et al.

(2006), which includes a drifting snow module and is used for avalanche forecasting.

Snow research in Finland began already in the 1800s when snow depth, snow density and snow season length monitoring started in the wake of increased interest in natural sciences. Other motivations were for example water system management and traffic on snow. Monitoring dominated until the mid-1900s when research questions started to arise. The modern snow science research in Finland is concentrated among other things on water resource monitoring, remote sensing techniques, and modelling in the polar regions and conducted by the Finnish universities and state institutions.(Simojoki, 1978; Leppäranta et al., 2001).

The snow conditions of Finnish Lapland in addition to the interannual variability and trends in winter weather over the years 1946-2012 were investigated by Merkouriadi et al. (2017). The description of the climatological conditions is based on the most recent 30-year period 1982-2011. Their findings show large interannual and regional variability, but averaged long-term temperature and precipitation trends were positive. However, the increased precipitation was counteracted by the atmospheric warming, which resulted in no significant trends in snow depth. The average snow season length was 206±14 days during the 30-year period.

Modelling of snow distribution is important at both large and small scales. Snow reflects solar radiation back to space more than snow-free areas and therefore affects large scale air temperature and circulation patterns. At smaller scales snow alters the energy budget between the ground and the atmosphere acting as an insulating barrier, and influences both flora and fauna. Snow distribution affects also the timing and magnitude of the snowmelt-runoff in the spring. (McKay and Adams, 1981; Liston, 1995; Liston and Elder, 2006a).

The main objective of the thesis is to assess how well SnowModel performs in the varying topography and vegetation of Northern Finland, where the climate is temperate and rapidly changing. The simulation results are compared with snow water equivalent (SWE) observations, which are assimilated to the model in the later stage. Besides SWE, the length of the snow season, precipitation and melt are studied. The model also gives information on what is hardly measured in Finland: sublimation. The second objective is to put the theory and physics of the models in the present state together in a single document instead of numerous articles describing the development of the model.

The outline of the thesis is the following: first, a summary of the physics included in SnowModel, its submodels, and MicroMet is presented in Chapter 2. Then, in Chapter 3 the study domain and the input data are described. The results of the simulations are presented and discussed in Chapter 4, and finally concluded in Chapter 5.

# Chapter 2

# Model description

This study utilizes two models, a spatially distributed snow evolution modelling system SnowModel and a meteorological distribution model MicroMet, both by Dr. Glen E. Liston (Cooperative Institute for Research in the Atmosphere (CIRA), Colorado State University). The models were originally developed for nonforested surroundings but later modified to forested areas as well. (Liston and Elder, 2006a,b) This chapter describes concisely the two models and the physics included in them. SnowModel requires spatially distributed temporally varying meteorological forcing data, which is provided by MicroMet and hence that process is described first. The description follows closely the notation of several original articles, in which the development of the models and their submodels are reported. In places some variables had to be given a different symbol to avoid double definitions but also to standardise the notation between the articles. The reader is advised to refer to the detailed list of symbols and acronyms starting on page x if necessary.

## 2.1 MicroMet

The quasi-physically based meteorological distribution model MicroMet has been designed to produce high-resolution temporally and spatially continuous atmospheric forcing data, which is required to run terrestrial models. The horizontal grid size can be as small as 1 m. The model is based on known relationships between meteorological variables and the surrounding landscape (i.e. topography and vegetation). MicroMet also includes a data preprocessor, which controls the data quality and corrects deficiencies of hourly data. (Liston and Elder, 2006b).

MicroMet assumes that at least one value of each of the input variables is available at each time step within or somewhere near the simulation domain. The minimum input variables are: air temperature, relative humidity, wind speed, wind direction, and precipitation. In addition to the aforementioned variables, MicroMet creates distributed fields of incoming solar and longwave radiation, and surface pressure. If there are radiation and/or pressure observations available, they can be merged with the model-generated distributions. (Liston and Elder, 2006b).

The following sections describe the preprocessor, spatial interpolation of the data, and how the distributed variables are corrected to match the surrounding landscape.

### 2.1.1 Data preprocessor

The data preprocessor comprises of three steps (Liston and Elder, 2006b):

1. Filling missing time slots with an undefined value.
2. Quality assurance/quality control tests following Meek and Hatfield (1994).
    (a) Check for values outside acceptable limits.
    (b) Check for consecutive values that exceed acceptable increments.
    (c) Check for constant consecutive values.
3. Filling missing data with calculated values.
    (a) One missing data value gets the average value of the preceding and following data points in the time series.
    (b) For missing data segments of 2–24 hours, missing values get the average value of the values from 24 hours before and after, which preserves the diurnal cycle.
    (c) For missing data segments larger than 24 hours, an autoregressive integrated moving average (ARIMA) model (Box and Jenkins, 1976) is used to forecast and backcast values into the data gap, which are then linearly interpolated following the ideas of Walton (1996).

The quality control at step 2 ensures that the instruments measuring the meteorological variables have worked properly. For example, non-physical or constant values could indicate a broken instrument. For step 3 it is assumed that air temperature, relative humidity, wind speed, wind direction, and precipitation all have a diurnal cycles, since weather on a given day usually resembles the weather on the day before and after (Jolliffe and Stephenson, 2003). (Liston and Elder, 2006b).

The MicroMet preprocessor was tested in Liston and Elder (2006b), and the results show that the filling of data works well over a short period of time, for example less than three days. For longer time spans, up to approximately six days, the performance of the data-filling procedure is still satisfactory. Of course, stable and strong diurnal variations are easier to predict than those which have more irregular fluctuations.

### 2.1.2 Spatial interpolation

The model uses a Barnes objective analysis scheme, which is described more closely in Barnes (1964, 1973) and Koch et al. (1983), to horizontally interpolate the irregularly spaced station data to a regular grid. The interpolation in the Barnes scheme is based on a Gaussian distance-dependent weights, $w_t$,

$$w_t = \exp\left[-\frac{r^2}{f(dn)}\right], \tag{2.1}$$

where $r$ is the distance between a grid point and the observation, and filter parameter $f(dn)$ defines the smoothness of the interpolation. If only one observation of a variable exists, the variable is uniformly distributed instead of interpolation. (Liston and Elder, 2006b).

### 2.1.3 Air temperature

The station air temperatures are first calculated to a common reference level using a linear lapse rate dependence

$$T_r = T_{stn} - \Gamma(z_r - z_{stn}), \tag{2.2}$$

where $T_r$ (°C) is the air temperature at the reference level $z_r$ (m), $T_{stn}$ (°C) is the station air temperature, $\Gamma$ (°C km$^{-1}$) is the monthly varying air temperature lapse rate (in Table 2.1), and $z_{stn}$ (m) is the station elevation.

**Table 2.1:** The monthly air temperature lapse rate, vapour pressure coefficient (Kunkel, 1989), and precipitation adjustment factors (Thornton et al., 1997). (Liston and Elder, 2006b)

| Month | Air temperature lapse rate, $\Gamma$ (°C km$^{-1}$) | Vapor pressure coefficient, $\lambda$ (km$^{-1}$) | Precipitation adjustment factor, $\chi$ (km$^{-1}$) |
|---|---|---|---|
| Jan | 4.4 | 0.41 | 0.35 |
| Feb | 5.9 | 0.42 | 0.35 |
| Mar | 7.1 | 0.40 | 0.35 |
| Apr | 7.8 | 0.39 | 0.30 |
| May | 8.1 | 0.38 | 0.25 |
| Jun | 8.2 | 0.36 | 0.20 |
| Jul | 8.1 | 0.33 | 0.20 |
| Aug | 8.1 | 0.33 | 0.20 |
| Sep | 7.7 | 0.36 | 0.20 |
| Oct | 6.8 | 0.37 | 0.25 |
| Nov | 5.5 | 0.40 | 0.30 |
| Dec | 4.7 | 0.40 | 0.35 |

The reference level air temperatures are then interpolated to the model grid and finally adjusted to the topographic height:

$$T_a = T_r - \Gamma(z - z_r), \tag{2.3}$$

where $T_a$ (°C) is the air temperature at the topographic height $z$ (m) (Liston and Elder, 2006b).

### 2.1.4 Relative humidity

As can be seen in the following equations, relative humidity, RH (%), is a nonlinear function of elevation. Therefore, rather linear dewpoint temperature, $T_d$ (°C), is used instead to adjust the station relative humidity to the actual topographic height. (Liston and Elder, 2006b).

The saturation vapour pressure, $e_s$ (Pa), is

$$e_s = a \exp\left(\frac{bT_a}{c+T_a}\right), \tag{2.4}$$

where the constants are for water $a = 611.21$ Pa, $b = 17.502$, and $c = 240.97$ °C, and for ice $a = 611.15$ Pa, $b = 22.452$, and $c = 272.55$ °C (Buck, 1981).

With the saturation vapour pressure, the actual vapour pressure, $e$ (Pa), can be solved using

$$\mathrm{RH} = 100\frac{e}{e_s}. \tag{2.5}$$

The dewpoint temperature is then

$$T_d = \frac{c \ln\left(\frac{e}{a}\right)}{b - \ln\left(\frac{e}{a}\right)}. \tag{2.6}$$

Now using procedure similar to adjusting the station air temperature to the elevation of the topographic dataset in Eqs. (2.2) and (2.3), the dewpoint temperature can be adjusted to a common reference level, interpolated and adjusted again to the topographic height when using the dewpoint temperature lapse rate, $\Gamma_d$ (°C km$^{-1}$), (Kunkel, 1989)

$$\Gamma_d = \lambda\frac{c}{b}, \tag{2.7}$$

where $\lambda$ is the monthly varying vapour pressure coefficient in Table 2.1. The adjusted dewpoint temperature values are then converted back to relative humidity with Eqs. (2.4) and (2.5) but now using dewpoint temperature to calculate the vapour pressure. (Liston and Elder, 2006b).

### 2.1.5 Wind speed and direction

The station wind speed, $W$ (m s$^{-1}$), is divided into zonal, $u$ (m s$^{-1}$), and meridional, $v$ (m s$^{-1}$), components using the wind direction, $\theta$ (°), to avoid interpolation errors with the 360°/0° direction line

$$u = -W \sin\theta, \tag{2.8}$$

$$v = -W \cos\theta. \tag{2.9}$$

After interpolation the components are converted back to speed and direction using the following equations (Liston and Elder, 2006b)

$$W = \left(u^2 + v^2\right)^{\frac{1}{2}}, \tag{2.10}$$

$$\theta = \frac{3\pi}{2} - \tan^{-1}\left(\frac{v}{u}\right). \tag{2.11}$$

The resulting gridded values are then modified by the topographic slope and curvature (Liston and Sturm, 1998). The terrain slope, $\beta$, is

$$\beta = \tan^{-1}\left[\left(\frac{\partial z}{\partial x}\right)^2 + \left(\frac{\partial z}{\partial y}\right)^2\right]^{\frac{1}{2}}, \tag{2.12}$$

where $x$ (m) is the horizontal east coordinate, and $y$ (m) is the horizontal north coordinate. The terrain slope azimuth, $\xi_s$, is given by

$$\xi_s = \frac{3\pi}{2} - \tan^{-1}\left(\frac{\partial z/\partial y}{\partial z/\partial x}\right) \tag{2.13}$$

(where north has zero azimuth, note the difference to subsequent Eq. (2.27)).

The curvature, $\Omega_c$, is computed for each model grid cell by calculating the difference in elevation for that grid cell and the average elevation of the two grid cells that are at a distance of one length scale, $\eta$ (m), on opposite sides of the main grid cell. The length scale approximates half the wavelength of the topographic features. The elevation difference is calculated for all of the four opposite directions that the eight cardinal and intercardinal directions form and finally averaged. Therefore,

$$\begin{aligned}\Omega_c =& \frac{1}{4}\left[\frac{z - \frac{1}{2}\left(z_W + z_E\right)}{2\eta} + \frac{z - \frac{1}{2}\left(z_S + z_N\right)}{2\eta}\right.\\ &\left. + \frac{z - \frac{1}{2}\left(z_{SW} + z_{NE}\right)}{2\sqrt{2}\eta} + \frac{z - \frac{1}{2}\left(z_{NW} + z_{SE}\right)}{2\sqrt{2}\eta}\right],\end{aligned} \tag{2.14}$$

where the subscripts $N, S, E, W, NE, SW, NW, SE$ are the abbreviations for the eight cardinal and intercardinal directions and refer to the grid cells in the corresponding direction from the main grid cell. (Liston and Elder, 2006b).

The slope in the direction of the wind, $\Omega_s$, is defined

$$\Omega_s = \beta \cos(\theta - \xi_s)\,. \tag{2.15}$$

The wind weighting factor, $W_w$, is then

$$W_w = 1 + \gamma_s \Omega_s + \gamma_c \Omega_c, \tag{2.16}$$

where $\gamma_s$ is the slope weight and $\gamma_c$ the curvature weight with values $0 \leq \gamma_s, \gamma_c \leq 1$, and it is suggested to set the values so that $\gamma_s + \gamma_c = 1.0$. Both $\Omega_s$ and $\Omega_c$ are scaled such that $-0.5 \leq \Omega_s, \Omega_c \leq 0.5$ where negative values correspond to lee and concave slopes with reduced wind speeds and positive values to windward and convex slope with increased wind speeds. The terrain modified wind speed, $W_t$ (m s$^{-1}$), is (Liston and Sturm, 1998; Liston and Elder, 2006b)

$$W_t = W_w W. \tag{2.17}$$

Modification for wind speed below the forest canopy, $u_c$ (m s$^{-1}$), is given by (Cionco, 1978)

$$u_c = W_t \exp\left[-a\left(1 - \frac{z_r}{h_c}\right)\right], \tag{2.18}$$

where the reference height is linked to the canopy height, $h_c$ (m), through $z_r = 0.6h_c$ assumed by Essery et al. (2003). The canopy flow index, $a$ is

$$a = \beta \mathrm{LAI}^*, \tag{2.19}$$

where $\beta = 0.9$ is a scaling factor (not slope) to adjust the leaf-area index, LAI$^*$ (m$^2$ m$^{-2}$), values to match Cionco's 1978 canopy flow indices. The LAI$^*$ values can be found in Table 2.2.

The wind direction diverting factor, $\theta_d$ (°), is according to Ryan (1977)

$$\theta_d = -0.5\Omega_s \sin\left[2\left(\xi_s - \theta\right)\right], \tag{2.20}$$

which is simply added to the wind direction to derive the terrain-modified wind direction, $\theta_t$ (°),

$$\theta_t = \theta + \theta_d. \tag{2.21}$$

### 2.1.6 Solar radiation

The model calculates the incoming solar radiation, $Q_{si}$ (W m$^{-2}$), considering both direct and diffuse radiation, the effect of cloud cover, and the topography using

$$Q_{si} = S^* \left(\Psi_{dir} \cos i + \Psi_{dif} \cos Z\right), \tag{2.22}$$

where $S^* = 1370$ W m$^{-2}$ (Kyle et al., 1985) is the solar constant i.e. the solar irradiance at the top of the atmosphere on a surface perpendicular to the solar beam, $\Psi_{dir}$ is the direct net sky transmissivity, $\Psi_{dif}$ is the diffuse net sky transmissivity, and the angle $i$ is between direct solar radiation and a slope. The solar zenith angle, $Z$, is given by

$$\cos Z = \sin\delta \sin\phi + \cos\delta \cos\phi \cos\tau, \tag{2.23}$$

where $\phi$ is latitude and $\tau$ is the hour angle

$$\tau = \pi\left(\frac{h}{12} - 1\right), \tag{2.24}$$

where $h$ is the hour of the day. The solar declination angle, $\delta$, is

$$\delta = \phi_T \cos\left[2\pi\left(\frac{d - d_r}{d_y}\right)\right], \tag{2.25}$$

where $\phi_T$ is the latitude of the Tropic of Cancer, $d$ is the day of the year, $d_r$ is the day of the summer solstice, and $d_y$ is the average number of days in a year. (Liston and Elder, 2006b).

The previously mentioned angle $i$ is

$$\cos i = \cos\beta \cos Z + \sin\beta \sin Z \cos(\mu - \xi_s) \tag{2.26}$$

where $\beta$ is the terrain slope by Eq. (2.12), and the terrain slope azimuth, $\xi_s$, has now south as zero azimuth (note difference to Eq. (2.13))

$$\xi_s = \frac{\pi}{2} - \tan^{-1}\left(\frac{\partial z/\partial y}{\partial z/\partial x}\right), \tag{2.27}$$

The solar azimuth, $\mu$, is calculated using

$$\mu = \sin^{-1}\left(\frac{\cos\delta \sin\tau}{\sin Z}\right), \tag{2.28}$$

where south has zero azimuth. (Liston and Elder, 2006b).

The fraction of solar radiation reaching the surface considering scattering, absorption, and reflection by clouds according to Burridge and Gadd (1974) is

$$\Psi_{dir} = (0.6 - 0.2\cos Z)\,(1.0 - \sigma_c) \tag{2.29}$$

for direct solar radiation and

$$\Psi_{dif} = (0.3 - 0.1\cos Z)\,\sigma_c \tag{2.30}$$

for diffuse solar radiation. $\sigma_c$ is the cloud-cover fraction following Walcek (1994)

$$\sigma_c = 0.832\exp\left(\frac{\mathrm{RH}_{700} - 100}{41.6}\right), \tag{2.31}$$

where $\mathrm{RH}_{700}$ is the relative humidity for the 700 hPa level and calculated by $T_a$ and $T_d$ of the same pressure level with Eqs. in Sections 2.1.3 and 2.1.4.

The solar radiation modification for forests follows the Beer-Lambert law (Hellström, 2000)

$$Q_{sif} = \tau_v Q_{si}, \tag{2.32}$$

where $Q_{sif}$ (W m$^{-2}$) is the solar radiation reaching the surface underneath the forest canopy, and $\tau_v$ is the fraction of incoming solar radiation transmitted through the forest canopy

$$\tau_v = \exp\left(-k\mathrm{LAI}^*\right), \tag{2.33}$$

where $k$ is a vegetation-dependent extinction coefficient. The model considers also unmodified solar radiation through gaps in the canopy with the canopy gap fraction, $G$, by

$$\tau_v = \tau_v\,(1 - G) + G, \tag{2.34}$$

where the $\tau_v$ on the right-hand side is defined by Eq. (2.33). (Liston and Elder, 2006a).

### 2.1.7 Longwave radiation

Incoming longwave radiation, $Q_{li}$ (W m$^{-2}$), is calculated considering cloud cover and variation related to elevation in the following manner according to Iziomon et al. (2003)

$$Q_{li} = \varepsilon_a \sigma T_a^4, \tag{2.35}$$

where $\sigma$ is the Stefan-Boltzmann constant and $T_a$ is the air temperature now in Kelvin scale (K). The atmospheric emissivity, $\varepsilon_a$, is

$$\varepsilon_a = \kappa\left(1 + Z_s\sigma_c^2\right)\left[1 - X_s\exp\left(\frac{-Y_s e}{T_a}\right)\right]. \tag{2.36}$$

Here $\kappa$ is an adjustable constant (not von Kármán's constant), the cloud-cover fraction $\sigma_c$ is by Eq. (2.31), and the atmospheric vapour pressure, $e$ (Pa), is by Eqs. (2.4). The coefficients $X_s$, $Y_s$, and $Z_s$ are defined by

$$C_s = \begin{cases} C_1, & \text{if } z < 200, \quad (2.37a) \\ C_1 + (z - z_1)\left(\dfrac{C_2 - C_1}{z_2 - z_1}\right), & \text{if } 200 \le z \le 3000, \quad (2.37b) \\ C_2, & \text{if } z > 3000, \quad (2.37c) \end{cases}$$

where $C$ can be replaced with $X$, $Y$, and $Z$, with $X_1 = 0.35$, $X_2 = 0.51$, $Y_1 = 0.100$ K Pa$^{-1}$, $Y_2 = 0.130$ K Pa$^{-1}$, $Z_1 = 0.224$, $Z_2 = 1.100$, $z_1 = 200$ m, and $z_2 = 3000$ m. (Liston and Elder, 2006b).

The incoming longwave radiation underneath the forest canopy, $Q_{lif}$ (W m$^{-2}$), is assumed to be a fractional sum of the unmodified longwave radiation through the canopy gaps and the longwave radiation emitted by the forest canopy (Liston and Elder, 2006a)

$$Q_{lif} = (1 - F_c)\, Q_{li} + F_c \sigma T_c^4, \tag{2.38}$$

where canopy emissivity is assumed to be unity (Sicart et al., 2004) and the canopy temperature equals the air temperature, $T_c = T_a$ (K). The canopy fraction, $F_c$, is

$$F_c = a + b \ln\left(\mathrm{LAI}^*\right), \tag{2.39}$$

where $a = 0.55$ and $b = 0.29$ are constants by Pomeroy et al. (2002).

### 2.1.8 Surface pressure

If observations are not available, atmospheric pressure, $p_a$ (Pa), is given by

$$p_a = p_0 \exp\left(-\frac{z}{H}\right), \tag{2.40}$$

where $p_0$ is the sea level pressure, and $H$ is the scale height of the atmosphere (Wallace and Hobbs, 1977). This produces time-independent pressure distribution. Surface pressure observations can be merged as a part of the data assimilation. (Liston and Elder, 2006b).

### 2.1.9 Precipitation

The station precipitation values are interpolated together with the station elevation and finally to the topographic height using a precipitation adjustment factor, $\chi$, to define the liquid-water precipitation rate, $P$ (mm h$^{-1}$),

$$P = P_r \left[ \frac{1 + \chi (z - z_r)}{1 - \chi (z - z_r)} \right], \tag{2.41}$$

where $P_r$ is the interpolated station precipitation, $z_r$ is interpolated station elevation, and $\chi$ is the monthly varying precipitation adjustment factor (Table 2.1). (Liston and Elder, 2006b).

## 2.2 SnowModel

SnowModel is a spatially distributed high-resolution snow-evolution modelling system that includes processes such as snow accumulation; blowing snow redistribution and sublimation; forest canopy interception, unloading, and sublimation; snow density evolution; and snowpack melt (Fig. 2.1). It consists of four submodels – EnBal, SnowPack, SnowTran-3D, and SnowAssim – which are described more closely in the subsequent sections. The model is designed to be applicable to various landscapes and climates where snow occurs and on grid sizes of 1 to 200 m and temporal increments of 10 min to 1 day. SnowModel input requirements are spatially distributed temporally varying meteorological forcing data of air temperature, relative humidity, wind speed, wind direction, and precipitation, which are provided by MicroMet (described in Section 2.1), in addition to spatially distributed topography and vegetation type data. The model can perform simulations also on sea ice, but that does not fall into the scope of this study. SnowModel can be run with different configurations together with MicroMet: MicroMet and EnBal; MicroMet, EnBal, and SnowPack; MicroMet and SnowTran-3D; or MicroMet, EnBal, SnowPack, and SnowTran-3D in addition to SnowAssim, which is used in any configuration if there are observations to assimilate to the simulations (Fig. 2.2). (Liston and Elder, 2006a; Liston and Hiemstra, 2008; Liston, 2016).

### 2.2.1 EnBal

The submodel EnBal does the surface energy balance calculations that simulate surface temperature and energy fluxes using the equation

$$(1 - \alpha_s) Q_{si} + Q_{li} + Q_{le} + Q_h + Q_e + Q_c = Q_m, \tag{2.42}$$

where $\alpha_s$ is the surface albedo, $Q_{si}$ is the incoming solar radiation reaching the surface, $Q_{li}$ is the incoming longwave radiation reaching the surface, $Q_{le}$ is the emitted longwave radiation, $Q_h$ is the turbulent exchange of sensible heat, $Q_e$ is the turbulent exchange of latent heat, $Q_c$ is the conductive heat flux, and $Q_m$ is the available melt energy. All of

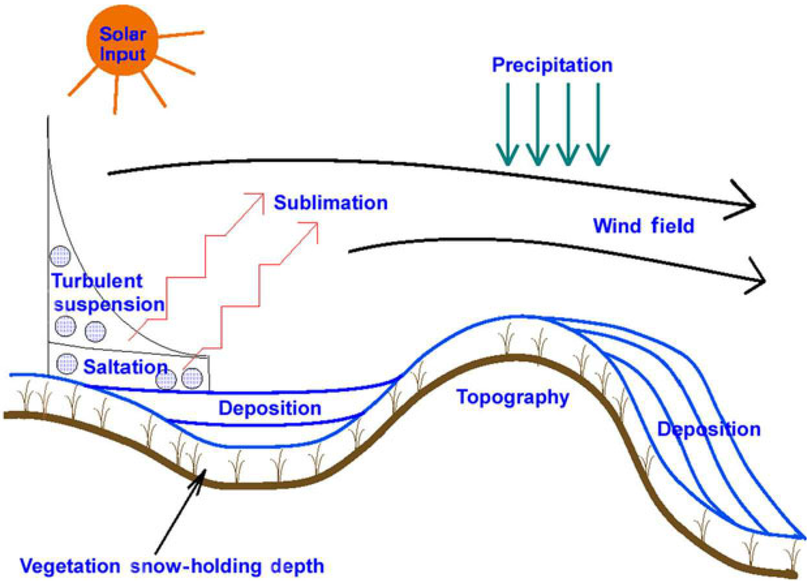

**Figure 2.1:** Illustration of the key features in SnowModel, reprinted from the Journal of Glaciology with permission of the International Glaciological Society. (Liston et al., 2007)

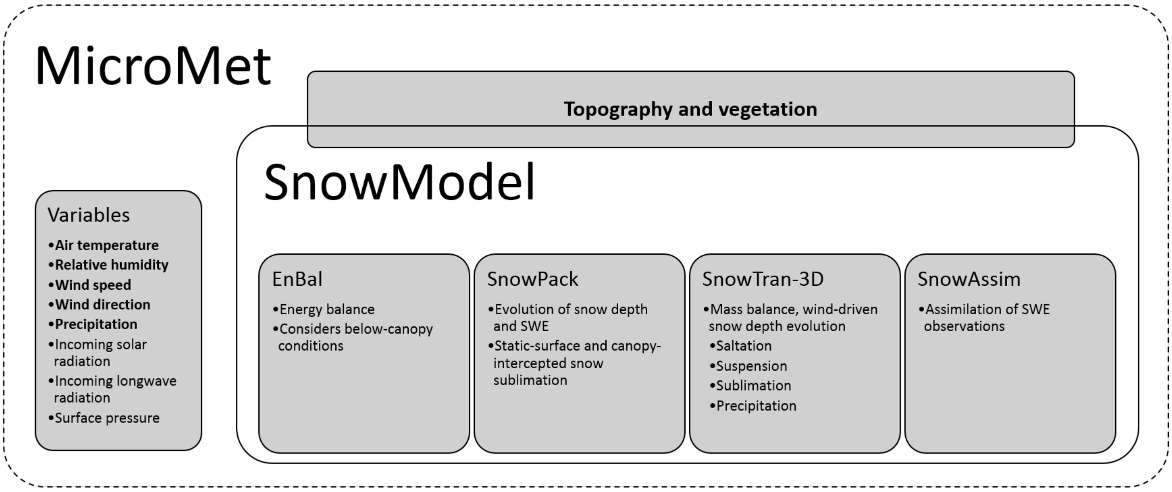

**Figure 2.2:** Illustration of the MicroMet and SnowModel modelling systems describing the main functions of the submodels. The variables in bold are the minimum input variables.

the energy terms have units of W $m^{-2}$. The energy terms are set in the form where the surface temperature $T_0$ (°C) is the only unknown variable. The melt energy $Q_m$ is first set to zero and the surface balance equation (2.42) is solved iteratively for $T_0$ using the Newton-Raphson method. If there is snow and $T_0 > 0$ °C, it indicates that there is energy available for melting. In that case $T_0$ is fixed at 0 °C and the energy balance is solved for $Q_m$. The model uses different time-independent values for the albedo of non-melting snow, melting snow in forest-free areas, melting snow underneath the forest canopy, and glacier ice. Energy fluxes towards the surface are positive. (Liston and Hall, 1995; Liston et al., 1999; Liston and Elder, 2006b).

The first two terms are calculated already in MicroMet: the incoming solar radiation $Q_{si}$ in Section 2.1.6 and the incoming longwave radiation $Q_{li}$ in Section 2.1.7.

The longwave radiation emitted by the surface, $Q_{le}$, is

$$Q_{le} = -\varepsilon_0 \sigma T_0^4. \tag{2.43}$$

where $T_0$ is the surface temperature now in Kelvin degrees. The surface is assumed to emit as a grey body, which has the emissivity $\varepsilon_0 = 0.98$. (Liston and Hall, 1995).

The turbulent exchange of sensible and latent heat, $Q_h$ and $Q_e$, respectively, are defined according to Price and Dunne (1976) as

$$Q_h = \rho_a C_p D_h \zeta \left(T_a - T_0\right), \tag{2.44}$$

$$Q_e = \rho_a L_s D_e \zeta \left(0.622 \frac{e_a - e_0}{p_a}\right), \tag{2.45}$$

where $\rho_a$ (kg m$^{-3}$) is the air density, $C_p$ (J kg$^{-1}$ K$^{-1}$) is the specific heat of air, and $L_s$ (J kg$^{-1}$) is the latent heat of sublimation. The vapour pressure of air and the surface, $e_a$ and $e_0$, respectively, are calculated as Eq. (2.4) with corresponding temperatures, and atmospheric pressure, $p_a$, as Eq. (2.40). The exchange coefficients, $D_h$ and $D_e$, are

$$D_{h,e} = \frac{\kappa^2 u_r}{\left[\ln\left(\frac{z_r}{z_0}\right)\right]^2}, \tag{2.46}$$

where $\kappa$ is the von Kármán's constant, $u_r$ (m s$^{-1}$) is the wind speed at reference height $z_r$ (m), and $z_0$ is the roughness length (m). The non-dimensional stability function, $\zeta$, is defined for different atmospheric conditions following Louis (1979)

$$\zeta = \begin{cases} 1 - \dfrac{\eta \mathrm{Ri}}{1 + \gamma |\mathrm{Ri}|^{\frac{1}{2}}}, & \text{if Ri} < 0 \text{ (unstable)}, \quad (2.47a) \\ 1, & \text{if Ri} = 0 \text{ (neutrally stable)}, \quad (2.47b) \\ \dfrac{1}{\left(1 + \eta^* \mathrm{Ri}\right)^2}, & \text{if Ri} > 0 \text{ (stable)}, \quad (2.47c) \end{cases}$$

where $\eta = 9.4$ and $\eta^* = \frac{\eta}{2}$ are constants (not related to curvature length scale), and

$$\gamma = \psi \eta \frac{D_{h,e}}{u_r} \left(\frac{z_r}{z_0}\right)^{\frac{1}{2}}, \tag{2.48}$$

where $\psi = 5.3$ is a constant (not sublimation rate coefficient). The Richardson number, Ri, is calculated using

$$\mathrm{Ri} = \frac{g}{T_r} \frac{\Delta T_r / \Delta z}{\left(\Delta u_r / \Delta z\right)^2}, \tag{2.49}$$

where $g$ (m s$^{-2}$) is the gravitational acceleration. The difference marked by $\Delta$ is between the reference level and the surface. (Liston and Hall, 1995; Liston et al., 1999).

The conductive heat flux at the surface, $Q_c$, is

$$Q_c = -k_{eff} \left. \frac{\mathrm{d}T_s}{\mathrm{d}z} \right|_{z=0}, \tag{2.50}$$

where $T_s$ (K) is the snow temperature. The effective thermal conductivity of snow, $k_{eff}$ (W m$^{-1}$ K$^{-1}$), is calculated in the submodel SnowPack, Eq. (2.57). (Liston and Hall, 1995).

## 2.2.2 SnowPack

SnowPack is a submodel of SnowModel which simulates the evolution of snow depth and snow water equivalent (SWE) in the snowpack. SnowPack should not be mixed with SNOWPACK by (Bartelt and Lehning, 2002). In the model the snow density evolves due to the weight of the overlying snow and the snow temperature and also due to sublimation of non-blowing snow and melting. SnowPack also calculates the density of new snow and deals with sublimation of canopy-intercepted snow. The model can be run with multiple layers, but for simplicity the following equations are for the one-layer case. (Liston and Hall, 1995; Liston and Elder, 2006a).

The density increase due to compaction follows Anderson (1976)

$$\frac{\partial \rho_s}{\partial t} = A_1 h_w^* \rho_s \exp\left[-B\left(T_f - T_s\right)\right] \exp\left(-A_2 \rho_s\right), \tag{2.51}$$

where $\rho_s$ (kg m$^{-3}$) is the snow density, $t$ (s) is time, $h_w^* = \frac{1}{2} h_w$ (m) is the weight of snow defined as half of the snow water equivalent $h_w$, $T_f$ (K) is the freezing temperature of water, and the snow temperature is calculated as the average temperature of the snow-ground interface and surface temperatures $T_s = \frac{1}{2}\left(T_g + T_0\right)$ (in Kelvin). The constants $A_1$, $A_2$ and $B$ are based on Kojima (1967): $A_1 = 0.0013$ m$^{-1}$ s$^{-1}$, $A_2 = 0.021$ m$^3$ kg$^{-1}$, and $B = 0.08$ K$^{-1}$. The snow water equivalent, $h_w$ (m), is defined as

$$h_w = \frac{\rho_s}{\rho_w} \zeta_s, \tag{2.52}$$

where $\rho_w$ (kg m$^{-3}$) is the water density, and $\zeta_s$ (m) is the snow depth. (Liston and Hall, 1995).

The snow depth is reduced due to static-surface sublimation and melt through equations

$$\rho_w L_s \frac{\mathrm{d}S_p}{\mathrm{d}t} = -Q_e, \tag{2.53}$$

$$\rho_w L_f \frac{\mathrm{d}M_p}{\mathrm{d}t} = Q_m, \tag{2.54}$$

where $L_f$ (J kg$^{-1}$) is the latent heat of freezing, $S_p$ (m) is the potential snow sublimation, and $M_p$ (m) is the potential snow melt. The new snow depth is adjusted accordingly. (Liston and Hall, 1995; Liston, 2016).

Precipitation is assumed to be snow, if the wet-bulb temperature $T_{wb} < 1$ °C. According to Rogers (1979) the wet-bulb temperature is

$$T_{wb} = T_a + [e - e_s(T_{wb})]\left(\frac{0.622}{p_a}\frac{L_s}{C_p}\right), \tag{2.55}$$

where $e$ and $e_s$ (Pa) are the atmospheric and saturation vapour pressure, respectively, calculated with Eqs. (2.4) and (2.5), and $p_a$ (Pa) is the atmospheric pressure using Eq. (2.40). The equation is solved iteratively using the Newton-Raphson method.

The new snow density, $\rho_{ns}$ (kg m$^{-3}$), is calculated using the equation by Anderson (1976)

$$\rho_{ns} = 50 + 1.7\,(T_{wb} - 258.16)^{1.5}. \tag{2.56}$$

Changes in density also modify the effective thermal conductivity of snow, $k_{eff}$, which according to Sturm et al. (1997) varies by

$$k_{eff} = \begin{cases} 0.023 + 0.234\rho_s, & \rho_s < 0.156, \qquad (2.57a) \\ 0.138 - 1.01\rho_s + 3.233\rho_s^2, & 0.156 \le \rho_s \le 0.6, \qquad (2.57b) \end{cases}$$

where the unit of $\rho_s$ is g cm$^{-3}$.

SnowPack calculates the sublimation of canopy-intercepted snow, $Q_{cs}$ (kg m$^{-2}$), using the following set of equations (Liston and Elder, 2006a)

$$Q_{cs} = C_e I \Psi \mathrm{d}t, \tag{2.58}$$

where d$t$ is the time increment and the canopy-intercepted load, $I$ (kg m$^{-2}$), at time $t$ follows Pomeroy et al. (1998)

$$I = I^{t-1} + 0.7\left(I_{max} - I^{t-1}\right)\left[1 - \exp\left(-\frac{P_s}{I_{max}}\right)\right], \tag{2.59}$$

where the superscript $t-1$ indicates the previous timestep, $P_s$ (kg m$^{-2}$) is the snow precipitation. The maximum interception storage, $I_{max}$ (kg m$^{-2}$), is defined by Hedstrom and

Pomeroy (1998) as

$$I_{max} = 4.4\mathrm{LAI}^{*}. \tag{2.60}$$

According to Pomeroy and Schmidt (1993), the canopy exposure coefficient, $C_e$, is

$$C_e = k_c \left( \frac{I^t}{I_{max}} \right)^{-0.4}, \tag{2.61}$$

where the superscript $t$ indicates the current timestep. Liston (2016) defines the dimensionless constant as $k_c = 0.00995$.

The sublimation-loss rate coefficient, $\Psi$ ($\mathrm{s}^{-1}$), for a spherical ice particle is calculated using

$$\Psi = \frac{1}{m}\frac{\mathrm{d}m}{\mathrm{d}t}, \tag{2.62}$$

where $m$ (kg) is the particle mass

$$m = \frac{4}{3}\pi \rho_i r^3, \tag{2.63}$$

where $\rho_i$ (kg $\mathrm{m}^{-3}$) is ice density and $r = 5 \cdot 10^{-6}$ m is the assumed particle radius (Liston and Elder, 2006a).

Thorpe and Mason (1966) and Schmidt (1972) describe the rate of mass loss from an spherical ice particle with humidity difference between the particle and the atmosphere, solar radiation absorbed by the particle, particle size, and ventilation effects using

$$\frac{\mathrm{d}m}{\mathrm{d}t} = \frac{2\pi r \left( \frac{\mathrm{RH}}{100} - 1 \right) - Q_p \Omega}{L_s \Omega + \frac{1}{D \rho_v \mathrm{Sh}}}, \tag{2.64}$$

where RH (%) is the relative humidity given by MicroMet Eq. (2.5), and $\Omega$ is

$$\Omega = \frac{1}{\lambda_t T_a \mathrm{Nu}} \left( \frac{L_s M_w}{R T_a} - 1 \right), \tag{2.65}$$

where $M_w$ (kg $\mathrm{kmol}^{-1}$) is the molecular weight of water, $R$ (J $\mathrm{kmol}^{-1}$ $\mathrm{K}^{-1}$) is the universal gas constant, and $\lambda_t$ (W $\mathrm{m}^{-1}$ $\mathrm{K}^{-1}$) is the atmospheric thermal conductivity. The relative humidity and the air temperature are assumed to be constant with height through the canopy. (Liston and Elder, 2006a).

The diffusivity of water vapour in the atmosphere, $D$ ($\mathrm{m}^2$ $\mathrm{s}^{-1}$), follows Thorpe and Mason (1966)

$$D = 2.06 \cdot 10^{-5} \left( \frac{T_a}{273} \right)^{1.75}, \tag{2.66}$$

and the saturation density of water vapour, $\rho_v$ (kg $\mathrm{m}^{-3}$), is defined by Fleagle and Businger

(1980)

$$\rho_v = 0.622\frac{e_s}{R_d T_a}, \tag{2.67}$$

where $R_d$ (J kg$^{-1}$ K$^{-1}$) is the gas constant for dry air and the saturation vapour pressure over ice, $e_s$ (Pa), is calculated by Eq. (2.4).

According to Lee (1975), the Nusselt (Nu) and Sherwood (Sh) numbers are linked with the Reynolds number (Re)

$$\mathrm{Nu} = \mathrm{Sh} = 1.79 + 0.606\mathrm{Re}^{0.5} \qquad 0.7 < \mathrm{Re} < 10, \tag{2.68}$$

where

$$\mathrm{Re} = \frac{2 r u_c}{v}, \tag{2.69}$$

where $v$ (m$^2$ s$^{-1}$) is the kinematic viscosity of air, and $u_c$ is the canopy wind speed which is calculated by Eq. (2.18) in MicroMet.

The snow particle absorbs solar radiation the amount of $Q_p$ (W) following the equation

$$Q_p = \pi r^2 \left(1 - \alpha_p\right) Q_{si} \tag{2.70}$$

where the snow particle albedo is assumed to be equal to the simulated albedo $\alpha_p = \alpha_s$, and $Q_{si}$ is the incoming solar radiation calculated in MicroMet Eq. (2.22) (Liston and Elder, 2006a).

If the air temperature within the forest canopy rises above freezing, the intercepted snow is unloaded assuming a rate of 5 kg m$^{-2}$ day$^{-1}$ K$^{-1}$. This leads to a melt-unloading rate, $L_m$ (kg m$^{-2}$), of

$$L_m = 5.8 \cdot 10^{-5} \left(T_a - 273.16\right) \mathrm{d}t, \qquad T_a > 0\,^{\circ}\mathrm{C}. \tag{2.71}$$

The model does not yet include unloading by wind, which is a complex process. (Liston and Elder, 2006a).

### 2.2.3 SnowTran-3D

The three-dimensional submodel SnowTran-3D calculates wind-driven snow depth evolution, and its primary components are

1. the wind forcing field,
2. the wind shear stress on the surface,
3. the transport of snow by saltation and suspension,
4. the sublimation of saltating and suspended snow, and
5. the accumulation and erosion of snow at the snow surface,

which will be described more closely in the following subsections. Snow-vegetation interactions are important when simulating blowing snow, which is why each grid cell has a single vegetation type. The vegetation types are assigned a canopy height, which equals the snow-holding depth. In other words, snow becomes available for wind transport only when the snow depth exceeds the snow-holding depth. The vegetation types and associated snow-holding depths included in SnowModel are listed in Table 2.2. (Liston and Sturm, 1998; Liston and Elder, 2006a; Liston et al., 2007).

#### 2.2.3.1 Wind forcing field

The wind forcing field is calculated already in MicroMet, Section 2.1.5.

#### 2.2.3.2 Wind shear stress on the surface

The shear stress exerted to the surface by the wind is formulated using wind-shear velocity, $u_*$ (m s$^{-1}$), (Liston and Sturm, 1998)

$$u_* = u_r \frac{\kappa}{\ln\left(\dfrac{z_r}{z_0}\right)}. \tag{2.72}$$

If the wind-shear velocity exceeds the threshold shear velocity, $u_{*t}$ (m s$^{-1}$), and if there is snow available for transport, saltation will begin.

Snow is available for transport, if the snow depth, $\zeta_s$ (m), exceeds the snow-holding depth, $C_v$ (m). Where the snow depth does not exceed the snow-holding depth, the depth-fraction of vegetation covered by snow, $F_s$, is defined as

$$F_s = \frac{\zeta_s}{C_v} \tag{2.73}$$

and used to linearly weigh the constant roughness lengths of snow and vegetation, $z_0^{snow}$ and $z_0^{veg}$, respectively, using

$$z_0 = \begin{cases} F_s z_0^{snow} + (1 - F_s)\, z_0^{veg}, & \text{if } \zeta_s \le C_v \text{ (no saltation)}, \quad (2.74\text{a}) \\ 0.12 \dfrac{u_*^2}{2g}, & \text{if } \zeta_s > C_v \text{ (saltation)}, \quad (2.74\text{b}) \end{cases}$$

where Eq. (2.74b) is by Owen (1964); Tabler (1980). Saltation is determined by solving Eqs. (2.72) and (2.74b) for $u_*$ and $z_0$ using Newton-Raphson iteration. If $u_* > u_{*t}$, saltation occurs. $u_{*t}$ can be constant or vary with density, of which the latter case is described next. (Liston and Sturm, 1998; Liston et al., 2007).

The snowpack in SnowTran-3D is composed of two layers, soft top layer and hard immobile under layer. $u_{*t}$ of the soft top layer can be determined through the temporal

**Table 2.2:** SnowModel vegetation types, snow-holding depths ($C_v$), and effective leaf area index values (LAI$^*$) for the forest types in summer (maximum) and in winter (minimum). (Liston and Elder, 2006a; Liston, 2016)

| Code | Class | Description | Example | $C_v$ (m) | LAI* max/min |
|---|---|---|---|---|---|
| 1 | Forest | Coniferous forest | Spruce-fir/taiga/lodgepole | 15.00 | 2.5/2.5 |
| 2 | Forest | Deciduous forest | Aspen forest | 12.00 | 2.5/0.5 |
| 3 | Forest | Mixed forest | Aspen/spruce-fir/low taiga | 14.00 | 2.5/1.5 |
| 4 | Forest | Scattered short-conifer | Pinyon-juniper | 8.00 | 1.5/1.5 |
| 5 | Forest | Clearcut conifer | Stumps and regenerating | 4.00 | 1.0/1.0 |
| 6 | Shrub | Mesic upland shrub | Deeper soils, less rocky | 0.50 | |
| 7 | Shrub | Xeric upland shrub | Rocky, windblown soils | 0.25 | |
| 8 | Shrub | Playa shrubland | Greasewood, saltbush | 1.00 | |
| 9 | Shrub | Shrub wetland/riparian | Willow along streams | 1.75 | |
| 10 | Shrub | Erect shrub tundra | Arctic shrubland | 0.65 | |
| 11 | Shrub | Low shrub tundra | Low to medium arctic shrubs | 0.30 | |
| 12 | Grass | Grassland rangeland | Graminoids and forbs | 0.15 | |
| 13 | Grass | Subalpine meadow | Meadows below treeline | 0.25 | |
| 14 | Grass | Tundra (non-tussock) | Alpine, high arctic | 0.15 | |
| 15 | Grass | Tundra (tussock) | Graminoid and dwarf shrubs | 0.20 | |
| 16 | Grass | Prostrate shrub tundra | Graminoid dominated | 0.10 | |
| 17 | Grass | Arctic graminid wetland | Grassy wetlands, wet tundra | 0.20 | |
| 18 | Bare | Bare | | 0.01 | |
| 19 | Water | Water/possibly frozen | | 0.01 | |
| 20 | Water | Permanent snow/glacier | | 0.01 | |
| 21 | Human | Residential/urban | | 0.01 | |
| 22 | Human | Tall crops | Corn stubble | 0.40 | |
| 23 | Human | Short crops | Wheat stubble | 0.25 | |
| 24 | Water | Ocean | | 0.01 | |
| 25-30 | | User defined | | | |

evolution of density and snow hardness. The soft layer density, $\rho_s$ (kg m$^{-3}$), can change during precipitation events through two processes: adding new snow without wind-induced compaction or increasing density with compaction by wind

$$\rho_s = \begin{cases} \rho_{ns}, & \text{if } W_t < 5 \text{ m s}^{-1}, \quad (2.75a) \\ \rho_{ns} + \rho_{wo}, & \text{if } W_t \geq 5 \text{ m s}^{-1}, \quad (2.75b) \end{cases}$$

where $\rho_{ns}$ (kg m$^{-3}$) is the new snow density calculated in SnowPack, Eq. (2.56), and $\rho_{wo}$ (kg m$^{-3}$) is the wind-induced density offset

$$\rho_{wo} = D_1 + D_2 \left\{1.0 - \exp\left[-D_3 \left(W_t - 5.0\right)\right]\right\}, \tag{2.76}$$

where $D_1 = 25.0$ kg m$^{-3}$, $D_2 = 250.0$ kg m$^{-3}$, and $D_3 = 0.2$ m$^{-1}$ s. (Liston et al., 2007).

During periods of no precipitation, density evolves similarly to Eq. (2.51) (Anderson, 1976) but now wind-induced

$$\frac{\partial \rho_s}{\partial t} = C A_1 U \rho_s \exp\left[-B\left(T_f - T_s\right)\right] \exp\left(-A_2 \rho_s\right) \tag{2.77}$$

where $A_1 = 0.0013$ m$^{-1}$, $A_2 = 0.021$ m$^3$ kg$^{-1}$, and $B = 0.08$ K$^{-1}$ are constants based on (Kojima, 1967), $C = 0.10$ is a non-dimensional constant controlling the density change rate, $T_f$ (K) is the water freezing temperature, and $T_s$ (K) is the soft layer snow temperature which is set to be the lesser of the air temperature or the freezing temperature. The wind speed contribution $U$ is given by

$$U = \begin{cases} 1.0 \text{ m s}^{-1} & \text{if } W_t < 5 \text{ m s}^{-1} \quad (2.78a) \\ E_1 + E_2 \left\{1.0 - \exp\left[-E_3 \left(W_t - 5.0\right)\right]\right\} & \text{if } W_t \geq 5 \text{ m s}^{-1} \quad (2.78b) \end{cases}$$

where $E_1 = 5.0$ m s$^{-1}$, $E_2 = 15.0$ m s$^{-1}$, and $E_3 = 0.2$ m$^{-1}$ s. (Liston et al., 2007).

An equation fitted to compression measurements by Abele and Gow (1975) gives a relationship

$$\sigma_s = 1.36 \exp\left(0.013 \rho_s\right) \tag{2.79}$$

where $\sigma_s$ (kPa) is the snow hardness. The data of Kotlyakov (1961) is used to describe the relationship between the snow hardness and the threshold shear velocity for snow densities 300 kg m$^{-3}$ < $\rho_s \leq$ 450 kg m$^{-3}$:

$$\sigma_s = 267 u_{*t}. \tag{2.80}$$

Setting Eqs. (2.79) and (2.80) equal gives a relationship between the threshold shear velocity and the snow density for the range 300 kg m$^{-3}$ < $\rho_s \leq$ 450 kg m$^{-3}$ but also a similar formulation for smaller densities (Liston et al., 2007)

$$u_{*t} = \begin{cases} 0.10\exp\left(0.003\rho_s\right), & \text{if } 50\ \mathrm{kg\,m^{-3}} < \rho_s \leq 300\ \mathrm{kg\,m^{-3}}, \quad (2.81a) \\ 0.005\exp\left(0.013\rho_s\right), & \text{if } 300\ \mathrm{kg\,m^{-3}} < \rho_s \leq 450\ \mathrm{kg\,m^{-3}}. \quad (2.81b) \end{cases}$$

#### 2.2.3.3 Transport of snow by saltation and suspension

Pomeroy and Gray (1990) describe the saltation-transport rate under equilibrium conditions, $Q^{max}_{salt}$ ($\mathrm{kg\,m^{-1}\,s^{-1}}$), as

$$Q^{max}_{salt} = \frac{0.68}{u_*}\frac{\rho_a}{g}u_{*t}\left(u_*^2 - u_{*t}^2\right). \tag{2.82}$$

$Q^{max}_{salt}$ is divided into $x$ and $y$ components using the corresponding wind velocity components

$$Q^{max}_{salt}(x) = Q^{max}_{salt}\frac{|u|}{\sqrt{u^2+v^2}}, \tag{2.83}$$

$$Q^{max}_{salt}\left(y\right) = Q^{max}_{salt}\frac{|v|}{\sqrt{u^2+v^2}}. \tag{2.84}$$

To include also the non-equilibrium conditions, the saltation-transport rate is formulated (for the $x$ direction) differentiating cases for increasing and decreasing wind-shear velocity

$$Q_{salt}(x) = \begin{cases} Q_{salt}(x-\Delta x) + \frac{\mu}{f}\Delta x\left[Q^{max}_{salt}(x) - Q_{salt}(x-\Delta x)\right], & \text{if } \frac{\partial u_*}{\partial x} \geq 0, \quad (2.85a) \\ \min\begin{cases} Q_{salt}(x-\Delta x), \\ Q^{max}_{salt}(x), \end{cases} & \text{if } \frac{\partial u_*}{\partial x} < 0. \quad (2.85b) \end{cases}$$

where $\Delta x$ is the horizontal grid resolution in the $x$ direction, $\mu = 3.0$ is a scaling constant (not solar azimuth), and $f = 500$ m is equilibrium-fetch distance by Pomeroy et al. (1993). The saltation-transport rate is calculated similarly for the $y$ direction, and finally they are summed to get the total value (Liston and Sturm, 1998)

$$Q_{salt} = Q_{salt}(x) + Q_{salt}\left(y\right). \tag{2.86}$$

Greeley and Iversen (1985) estimate the height of the saltation layer, $h_*$ (m), to be

$$h_* = 1.6\frac{u_*^2}{2g}. \tag{2.87}$$

If there is saltation, turbulent-suspension is possible. The transport rate for turbulent-suspended snow, $Q_{turb}$ (kg m$^{-1}$ s$^{-1}$), is

$$Q_{turb} = \int_{h_*}^{z_t} \phi_t(z)\, u(z)\, \mathrm{d}z, \tag{2.88}$$

where $\phi_t(z)$ (kg m$^{-3}$) is the mass concentration of the blowing snow in the turbulent-suspension layer, and $u(z)$ (m s$^{-1}$) is the wind velocity given by Eqs. (2.72). The integration limits are the bottom of the turbulent-suspension layer i.e. the top of the saltation layer, $h_*$, and the top of the turbulent-suspension layer, $z_t$ (m). (Liston and Sturm, 1998).

Kind (1992) defines the mass concentration of the turbulent-suspension layer as

$$\phi_t(z) = \phi_r \left[ \left( \frac{\phi^*}{\phi_r} \frac{u_*}{w_f} + 1 \right) \left( \frac{z}{z_r} \right)^{-\frac{w_f}{\kappa u_*}} - \frac{\phi^*}{\phi_r} \frac{u_*}{w_f} \right], \tag{2.89}$$

where $\phi_r$ is the mass concentration at the reference level $z_r$, $w_f = 0.3$ m s$^{-1}$ is the particle settling velocity (Schmidt, 1982b), and $\phi^*$ is a scaling parameter, which relates to the reference mass concentration as

$$\frac{\phi^*}{\phi_r} = \beta \frac{u_*}{u_r}, \tag{2.90}$$

where $\beta = 0.5$ is a coefficient (not slope) (Kind, 1992). To solve Eq. (2.89), the reference level is defined $z_r = h_*$. (Liston and Sturm, 1998).

According to Pomeroy and Gray (1990), the horizontal particle velocity in the saltation layer, $u_p$ (m s$^{-1}$), is independent of height

$$u_p = 2.8 u_{*t}. \tag{2.91}$$

Assuming that the mass-transport rate of the saltation layer does not depend on height either, the reference level mass-concentration is

$$\phi_r = \frac{Q_{salt}}{h_* u_p}, \tag{2.92}$$

where $Q_{salt}$ is by Eq. (2.86). (Liston and Sturm, 1998).

#### 2.2.3.4 Sublimation of saltating and suspended snow

The following section describes only the sublimation during wind transport – the static-surface sublimation is presented by Eq. (2.53) and from canopy-intercepted snow by Eq. (2.58).

The sublimation rate of wind-transported snow, $Q_v$ (kg m$^{-2}$ s$^{-1}$), is

$$\begin{aligned} Q_v &= \int_0^{z_t} \Psi(z)\,\phi(z)\,\mathrm{d}z \\ &= \Psi_s \phi_s h_* + \int_{h_*}^{z_t} \Psi_t(z)\,\phi_t(z)\,\mathrm{d}z, \end{aligned} \tag{2.93}$$

where $\Psi$ (s$^{-1}$) is the sublimation-loss rate coefficient and $\phi$ (kg m$^{-3}$) is the vertical mass-concentration distribution. The subscripts $s$ and $t$ refer to the saltation and the turbulent-suspension layers, respectively. The integration limits are the snow surface, $z = 0$, the saltation layer height, $h_*$, and the top of the turbulent-suspension layer, $z_t$. The second line of Eq. (2.93) describes the situation where the properties in the saltation layers are assumed to be constant with height. (Liston and Sturm, 1998).

The formulation of the sublimation rate of wind-transported snow presented in Liston and Sturm (1998), and now here, follows the work of Schmidt (1972, 1991); Pomeroy et al. (1993); and Pomeroy and Gray (1995). Note the differences in the subsequent equations compared to Eqs. (2.62)-(2.70).

The sublimation-loss rate coefficient, $\Psi(z)$ (s$^{-1}$), is given by

$$\Psi(z) = \frac{1}{\bar{m}(z)} \frac{\mathrm{d}\bar{m}(z)}{\mathrm{d}t}, \tag{2.94}$$

where $\bar{m}(z)$ (kg) is the mean particle mass at height $z$ approximated as

$$\bar{m}(z) = \frac{4}{3}\pi \rho_i \bar{r}(z)^3 \left(1 + \frac{3}{\alpha} + \frac{2}{\alpha^2}\right), \tag{2.95}$$

where $\bar{r}(z)$ (m) is the mean radius of snow particle given by

$$\bar{r}(z) = 4.6 \cdot 10^{-5} z^{-0.258}, \tag{2.96}$$

and $\alpha$ is a coefficient (not albedo) (Liston and Sturm, 1998)

$$\alpha = 4.08 + 12.6z. \tag{2.97}$$

Similarly to Eq. (2.64), the rate of mass loss is (Thorpe and Mason, 1966; Schmidt, 1972)

$$\frac{\mathrm{d}\bar{m}(z)}{\mathrm{d}t} = \frac{2\pi \bar{r}(z)\,\sigma_{us}(z) - Q_p \Omega}{L_s \Omega + \dfrac{1}{D \rho_v \mathrm{Sh}(z)}}, \tag{2.98}$$

where $\Omega$ is by Eq. (2.65), $D$ by Eq. (2.66), and $\rho_v$ by Eq. (2.67), where, however, the saturation vapour pressure over ice, $e_s$ (Pa), follows Murray (1967),

$$e_s = 610.78 \exp\left[\frac{21.875\left(T_a - 273.16\right)}{T_a - 7.66}\right]. \tag{2.99}$$

The radius of a snow particle, $\bar{r}(z)$ (m), of mean particle mass, $\bar{m}(z)$, is given by (Liston and Sturm, 1998)

$$\bar{r}(z) = \left[\frac{3\bar{m}(z)}{4\pi\rho_i}\right]^{\frac{1}{3}}. \tag{2.100}$$

The vertical distribution of the atmospheric undersaturation of water vapour with respect to ice, $\sigma_{us}(z)$, follows Pomeroy et al. (1993) and Déry and Taylor (1996) with a modification by Liston and Sturm (1998)

$$\sigma_{us}(z) = \sigma_r\left[\Gamma_{RH} + 0.027\ln(z)\right], \tag{2.101}$$

where $\sigma_r$ is the undersaturation at the height of the relative humidity observations, $z_{RH}$ (m),

$$\sigma_r = RH(z_{RH}) - 1, \tag{2.102}$$

and $\Gamma_{RH}$ is relative humidity offset

$$\Gamma_{RH} = 1 - 0.027\ln(z_{RH}). \tag{2.103}$$

When calculating the Nusselt and the Sherwood numbers, it must be noted that the mean particle radius and the ventilation velocity have vertical distribution. In addition, the ventilation velocity is different for the suspension and for the turbulent-suspension layers. According to Lee (1975)

$$\mathrm{Nu}(z) = \mathrm{Sh}(z) = 1.79 + 0.606\mathrm{Re}(z)^{0.5}, \tag{2.104}$$

with

$$\mathrm{Re}(z) = \frac{2\bar{r}(z)V_v(z)}{v}, \tag{2.105}$$

where $V_v(z)$ (m s$^{-1}$) is the ventilation velocity. For turbulent suspension $V_v = V_t$ and modeled by Lee (1975)

$$V_t(z) = \bar{w}(z) + 3x_r(z)\cos\left(\frac{\pi}{4}\right), \tag{2.106}$$

where the mean terminal-fall velocity of suspended snow, $\bar{w}(z)$ (m s$^{-1}$), is (Pomeroy and Male, 1986)

$$\bar{w}(z) = 1.1\cdot 10^{7}\,\bar{r}(z)^{1.8}, \tag{2.107}$$

and the fluctuating component, $x_r(z)$, is (Pomeroy, 1988)

$$x_r(z) = 0.005u(z)^{1.36}. \tag{2.108}$$

For saltation $V_v = V_s$ and is given by Pomeroy and Gray (1995) as

$$V_s = 0.68u_* + 2.3u_{*t}. \tag{2.109}$$

The snow particle absorbs solar radiation following the formulation

$$Q_p = \pi \bar{r}(z)^2 \left(1 - \alpha_p\right)(1 + \alpha_s) Q_{si}, \tag{2.110}$$

where $\alpha_p$ is the snow particle albedo and $\alpha_s$ is the snow surface albedo with values of 0.5 and 0.8, respectively, by Schmidt (1972). The incoming solar radiation, $Q_{si}$, is calculated in MicroMet, Eq. (2.22). (Liston and Sturm, 1998).

#### 2.2.3.5 Accumulation and erosion of snow at the snow surface

All the components of SnowTran-3D described above are put together to form a mass-balance equation which gives the temporal variation of snow depth, $\zeta_s$ (m). Changes in snow depth are the result of

1. changes in horizontal mass-transport rates of saltation, $Q_{salt}$ (kg m$^{-1}$ s$^{-1}$),
2. changes in horizontal mass-transport rates of turbulent-suspended snow, $Q_{turb}$ (kg m$^{-1}$ s$^{-1}$),
3. sublimation of transported snow particles, $Q_v$ (kg m$^{-2}$ s$^{-1}$), and
4. the water-equivalent precipitation rate, $P$ (m s$^{-1}$).

The different factors which lead to deposition and erosion are marked with a corresponding number to the mass-balance equation

$$\frac{\mathrm{d}\left(\rho_s \zeta_s\right)}{\mathrm{d}t} = \underbrace{\rho_w P}_{4.} - \left( \underbrace{\frac{\mathrm{d}Q_{salt}}{\mathrm{d}x} + \frac{\mathrm{d}Q_{salt}}{\mathrm{d}y}}_{1.} + \underbrace{\frac{\mathrm{d}Q_{turb}}{\mathrm{d}x} + \frac{\mathrm{d}Q_{turb}}{\mathrm{d}y}}_{2.} \right) + \underbrace{Q_v}_{3.}, \tag{2.111}$$

where $\rho_s$ and $\rho_w$ (kg m$^{-3}$) are the snow and water densities, respectively, and $t$ (s) is time. Also the schema in Fig. 2.3 illustrates the mass balance calculation. (Liston and Sturm, 1998).

### 2.2.4 SnowAssim

The data assimilation scheme SnowAssim is used to calculate the difference between the observed and modeled snow water equivalent distributions (although the submodel

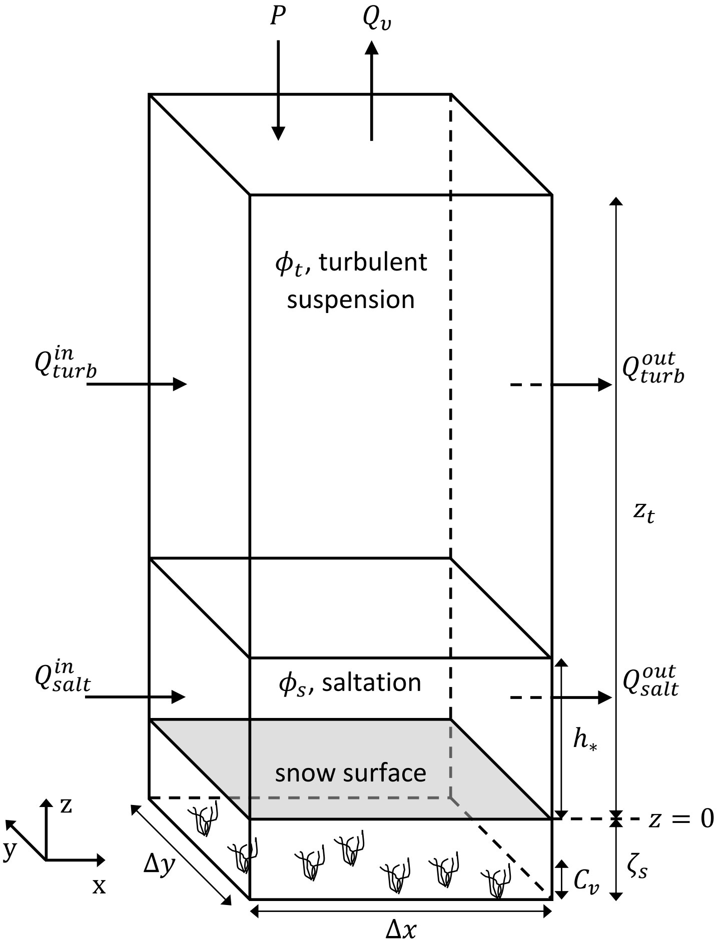

**Figure 2.3:** Schematic illustration of the mass-balance calculation in SnowTran-3D, redrawn and adapted from the Journal of Glaciology with permission of the International Glaciological Society. (Liston and Sturm, 1998)

is applicable to other variables, too). The corrections are used retroactively to improve the accuracy of the modelled fields before the observations. Calculating and applying the corrections require at most twice the computational resources/time required to run SnowModel by itself. The corrections are concentrated on the two elemental processes, accumulation and ablation, which are described next. (Liston and Hiemstra, 2008).

Accumulation is dominantly controlled by precipitation, $P$, which is modified with a precipitation adjustment factor, $P_{fact}$, to get the precipitation required to produce the observed SWE values:

$$P_{assim} = P_{fact}P. \tag{2.112}$$

The adjustment factor is calculated

$$ {}^{t}_{t-1}P_{fact} = \frac{\Delta h^{obs}_w}{\Delta h^{mod}_w} = \frac{{}^{t}h^{obs}_w - {}^{t-1}h^{obs}_w}{{}^{t}h^{mod}_w - {}^{t-1}h^{mod}_w} \tag{2.113}$$

where $h_w$ is the snow water equivalent and the superscript $t$ indicates the current timestep, $t-1$ the previous timestep, $obs$ the observed value of SWE, and $mod$ the modelled value of SWE. Further assuming

$$\sum_{t-1}^{t} P \approx {}^{t}h_w^{mod} - {}^{t-1}h_w^{mod}, \tag{2.114}$$

the Eq. (2.113) gets the form

$${}_{t-1}^{t}P_{fact} = 1 + \frac{\left({}^{t}h_w^{obs} - {}^{t}h_w^{mod}\right) - \left({}^{t-1}h_w^{obs} - {}^{t-1}h_w^{mod}\right)}{\sum\limits_{t-1}^{t} P}. \tag{2.115}$$

If the denominator $\sum_{t-1}^{t} P \approx {}^{t}h_w^{mod} - {}^{t-1}h_w^{mod} = 0$, the adjustment factor is set ${}_{t-1}^{t}P_{fact} = 1$. (Liston and Hiemstra, 2008).

A similar correction factor is defined for melt. Assuming that melt, $M$, equals

$$\sum_{t-1}^{t} M \approx -\left({}^{t}h_w^{mod} - {}^{t-1}h_w^{mod}\right), \tag{2.116}$$

the melt correction factor, $M_{fact}$, is

$${}_{t-1}^{t}M_{fact} = 1 - \frac{\left({}^{t}h_w^{obs} - {}^{t}h_w^{mod}\right) - \left({}^{t-1}h_w^{obs} - {}^{t-1}h_w^{mod}\right)}{\sum\limits_{t-1}^{t} M}. \tag{2.117}$$

Again, if the denominator equals zero, the factor is set to unity. The correction factor is then used to modify the melting (Liston and Hiemstra, 2008)

$${}_{t-1}^{t}M_{assim} = {}_{t-1}^{t}M_{fact}\ {}_{t-1}^{t}M. \tag{2.118}$$

The submodel assesses with relative contribution variables, $R_{prec}$ and $R_{melt}$, which correction to perform, precipitation or melt, respectively

$${}_{t-1}^{t}R_{prec} = \frac{\sum\limits_{t-1}^{t} P}{\sum\limits_{t-1}^{t} P + \sum\limits_{t-1}^{t} M}, \tag{2.119}$$

$${}_{t-1}^{t}R_{melt} = 1 - {}_{t-1}^{t}R_{prec}. \tag{2.120}$$

The greater value of these two indicates which correction to perform. If both precipitation and melt are zero or there are no future observations available, the correction factor is set to unity. (Liston and Hiemstra, 2008).

# Chapter 3

# Data and methods

This chapter introduces first the model domain, the input data and how it was processed. Next, the simulation runs and methods of analysis are described.

## 3.1 Area of interest

The area of interest of this study was chosen to be within the borders of my home country, Finland, because it is rather well studied and documented in many ways and most of the datasets are available for free. When choosing the domain, four key features were considered:

1. variability of topography,
2. variability of vegetation,
3. number of weather stations at different elevations, and
4. number of snow courses.

Domain sizes from 30 km up to 60 km were considered. The best possible combination of all the previously mentioned features was found in a 60 km by 60 km domain in the Saariselkä region in the municipalities of Inari and Sodankylä in North-East Lapland (Fig. 3.1). The domain is located between the parallels 68.08° N and 68.61° N, and the meridians 26.95° E and 28.43° E. In the ETRS-TM35FIN coordinate system, which will be used from now on and actually required by the SnowModel, the coordinates of the lower left corner are E 498160 N 7551340 and of the upper right corner E 558220 N 7611400. The domain is bordered by Russian wilderness in the east, by the Lokka reservoir in the south, by more wilderness of gently rolling fells in the west, and by Lake Inari to the north. Most of the areas east of the major road belong either to the national park named after the former President of the Republic of Finland Urho Kekkonen or to the Sompio Nature Reserve.

The following sections describe the key features from input data perspective: topography in Section 3.2, vegetation in Section 3.3, weather stations in Section 3.4, and snow courses in Section 3.5.

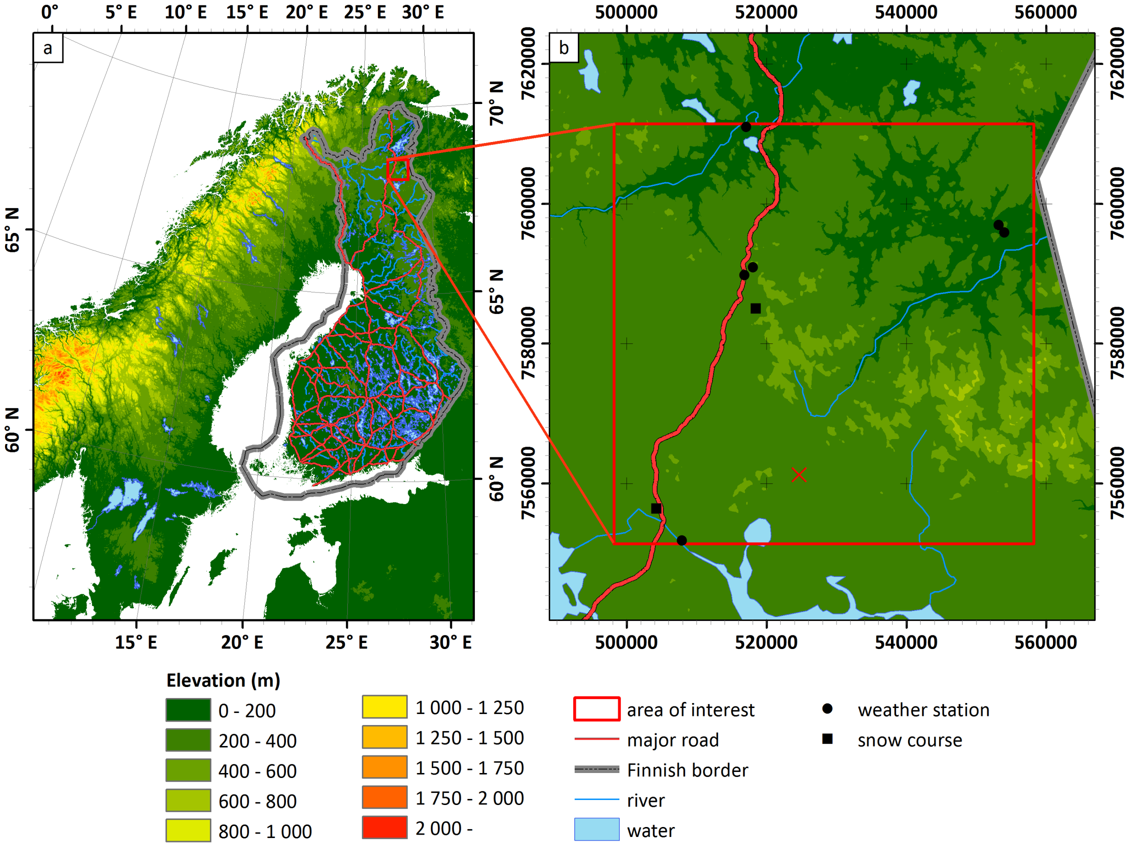

**Figure 3.1:** a) The location of the area of interest in Fennoscandia together with elevation, major roads, the Finnish borders, and water bodies. b) A close-up of the surroundings together with weather stations and snow courses within the area of interest. The red "X" marks the spot, where Figure 3.3 was taken. Note that the coordinates are now in UTM (ETRS-TM35FIN).

## 3.2 Topography data

The topography data is provided by the elevation model 2015 by the National Land Survey of Finland, NLS (Maanmittauslaitos, MML) (5 April 2016). The data in question is the most accurate digital elevation model available for whole Finland, and it has the grid size of 10 m by 10 m and the vertical accuracy of approximately 1.4 m. The topography data was processed with ArcGIS 10.3.1 software. The sheets of data were mosaicked together, clipped to exactly cover the domain, and finally resampled to 60 m by 60 m grid cell size due to computational restrictions.

The fells in Saariselkä area are mostly made of Lapland granulite that formed 1900 million years ago. The fells themselves and gorges between them were formed by block movements about 30-50 million years ago, and later shaped to more gently rolling features

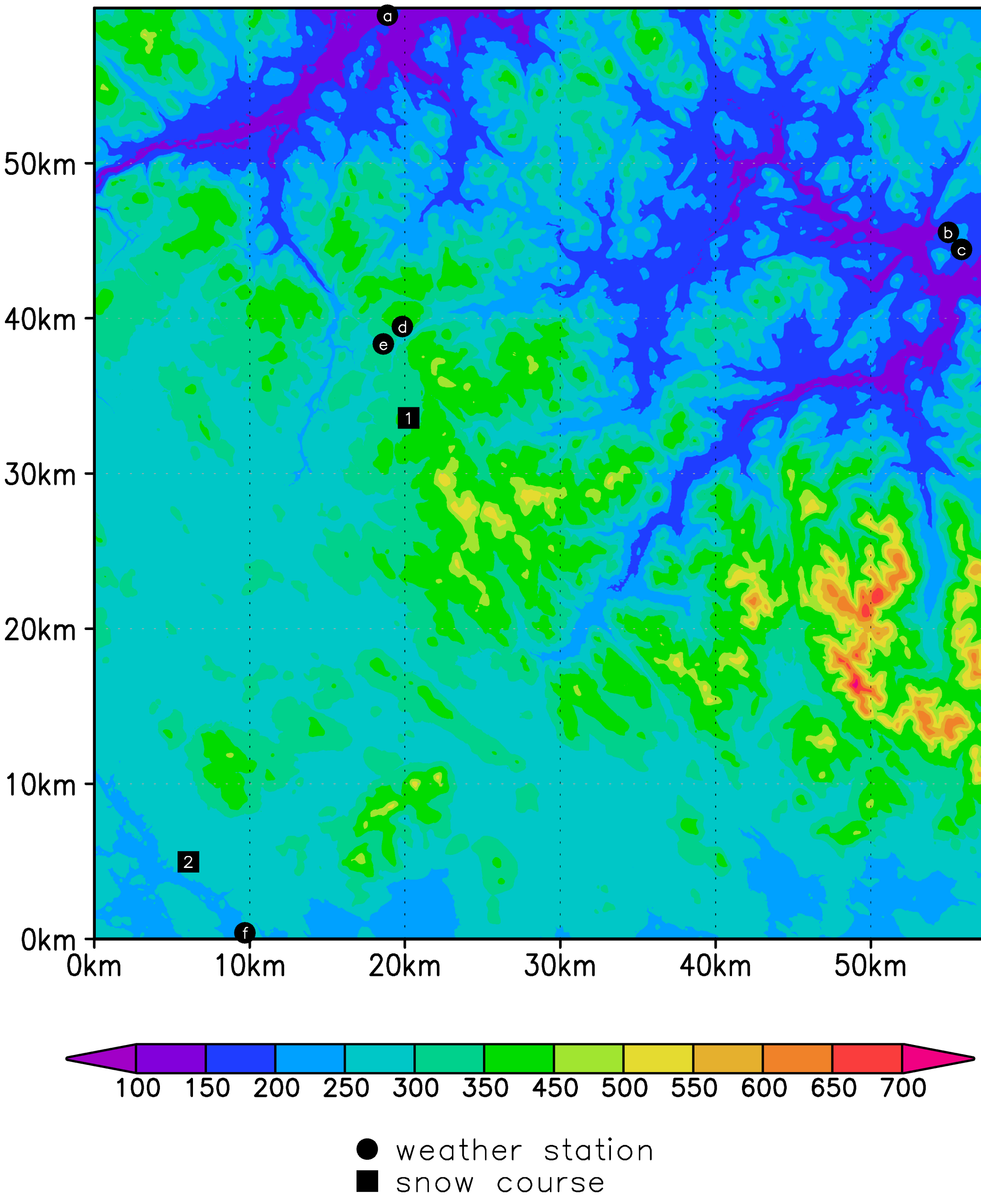

**Figure 3.2:** Topography of the domain in meters, together with the locations of the weather stations and the snow courses within the domain.

by the last ice age, which retreated from the area 9500 years ago. (State Forest Enterprise (Metsähallitus), 2017). Figure 3.2 shows the topography of the domain. The lowest point of elevation is 110 m in the Ivalojoki river valley near the northwest corner of the domain and the highest 718 m at the top of the Sokosti fell (Fig. 3.3) around the southeast part of the domain. Other main topographic features are the Ivalojoki river valley in the northwest corner of the domain and the Suomujoki/Lutto river valley in near the northeast corner.

**Figure 3.3:** The photograph was taken by the author on a flight from Helsinki to Ivalo on 18 December 2016 at 11.03 (UTC+2) at the location marked with the red "X" in Figure 3.1b looking east-northeast at the altitude of approximately 4000 m. The photograph shows the group of the highest fells in the domain, the highest one being the Sokosti fell 718 m above sea level.

## 3.3 Vegetation data

The vegetation data is the CORINE Land Cover 2012 dataset provided by the Finnish Environment Institute (Suomen ympäristökeskus, SYKE) (29 September 2016). The vegetation is classified into four hierarchy levels including 48 classes in total. The data has the resolution of 20 m by 20 m.

The data was processed with ArcGIS 10.3.1 software. The dataset was clipped to exactly cover the domain, and finally resampled to 60 m by 60 m grid cell size due to computational restrictions and to match the topography data. Finally the data was reclassified to match the vegetation classification in SnowModel (Table 3.1). Within the domain there are vegetation from 14 different classes with one user-defined vegetation class. The largest classes by area are coniferous forest (56 % of the domain), scattered short-conifer (12 %), and arctic wetland (11 %) while other classes cover less than 10 % of the domain area each (Fig. 3.4).

**Table 3.1:** Reclassification of Corine Land Cover 2012 vegetation data into SnowModel vegetation classes. More detailed description of the SnowModel vegetation classes in Table 2.2.

| SnowModel | | Corine Land Cover 2012 | |
|---|---|---|---|
| Code | Description | Code | Description |
| 1 | Coniferous forest | 24 | Coniferous forest on mineral soil |
| | | 25 | Coniferous forest on peatland |
| | | 26 | Coniferous forest on rocky soil |
| 2 | Deciduous forest | 22 | Broad-leaved forest on mineral soil |
| | | 23 | Broad-leaved forest on peatland |
| 3 | Mixed forest | 27 | Mixed forest on mineral soil |
| | | 28 | Mixed forest on peatland |
| | | 29 | Mixed forest on rocky soil |
| 4 | Scattered short-conifer | 20 | Land principally occupied by agriculture, with significant areas of natural vegetation |
| | | 21 | Agro-forestry areas |
| | | 32 | Transitional woodland / shrub, tree cover <10 % |
| | | 33 | Transitional woodland / shrub, tree cover 10–30 %, on mineral soil |
| | | 34 | Transitional woodland / shrub, tree cover 10–30 %, on peatland |
| | | 35 | Transitional woodland / shrub, tree cover 10–30 %, on rocky soil |
| | | 36 | Transitional woodland / shrub, under power lines |
| 5 | Clearcut conifer | | |
| 6 | Mesic upland shrub | | |
| 7 | Xeric upland shrub | | |
| 8 | Playa shrubland | | |
| 9 | Shrub wetland / riparian | | |
| 10 | Erect shrub tundra | | |
| 11 | Low shrub tundra | | |
| 12 | Grassland rangeland | 18 | Pastures |
| | | 19 | Natural pastures |
| 13 | Subalpine meadow | 30 | Natural grassland |
| 14 | Tundra (non-tussock) | 39 | Sparsely vegetated areas |
| 15 | Tundra (tussock) | 31 | Moors and heathland |
| 16 | Prostrate shrub tundra | | |

*continued*

| SnowModel | | Corine Land Cover 2012 | |
|---|---|---|---|
| Code | Description | Code | Description |
| 17 | Arctic graminid wetland | 40 | Inland marshes, terrestrial |
| | | 42 | Peatbogs |
| | | 43 | Peat production sites |
| | | 44 | Salt marshes, terrestrial |
| 18 | Bare | 38 | Bare rock |
| 19 | Water / possibly frozen | 41 | Inland marshes, aquatic |
| | | 45 | Salt marshes, aquatic |
| | | 46 | Water courses |
| | | 47 | Water bodies |
| | | 48 | Sea and ocean |
| 20 | Permanent snow / glacier | | |
| 21 | Residential / urban | 1 | Continuous urban fabric |
| | | 2 | Discontinuous urban fabric |
| | | 3 | Commercial units |
| | | 4 | Industrial units |
| | | 5 | Road and rail networks and associated land |
| | | 6 | Port areas |
| | | 7 | Airports |
| | | 8 | Mineral extraction sites |
| | | 9 | Open cast mines |
| | | 10 | Dump sites |
| | | 11 | Construction sites |
| | | 12 | Summer cottages |
| | | 13 | Sport and leisure areas |
| | | 14 | Golf courses |
| | | 15 | Trotting tracks |
| 22 | Tall crops | 17 | Fruit trees and berry plantations |
| 23 | Short crops | 16 | Non-irrigated arable land |
| 24 | Ocean | | |
| 25 | User defined | 37 | Beaches, dunes, and sand plains |

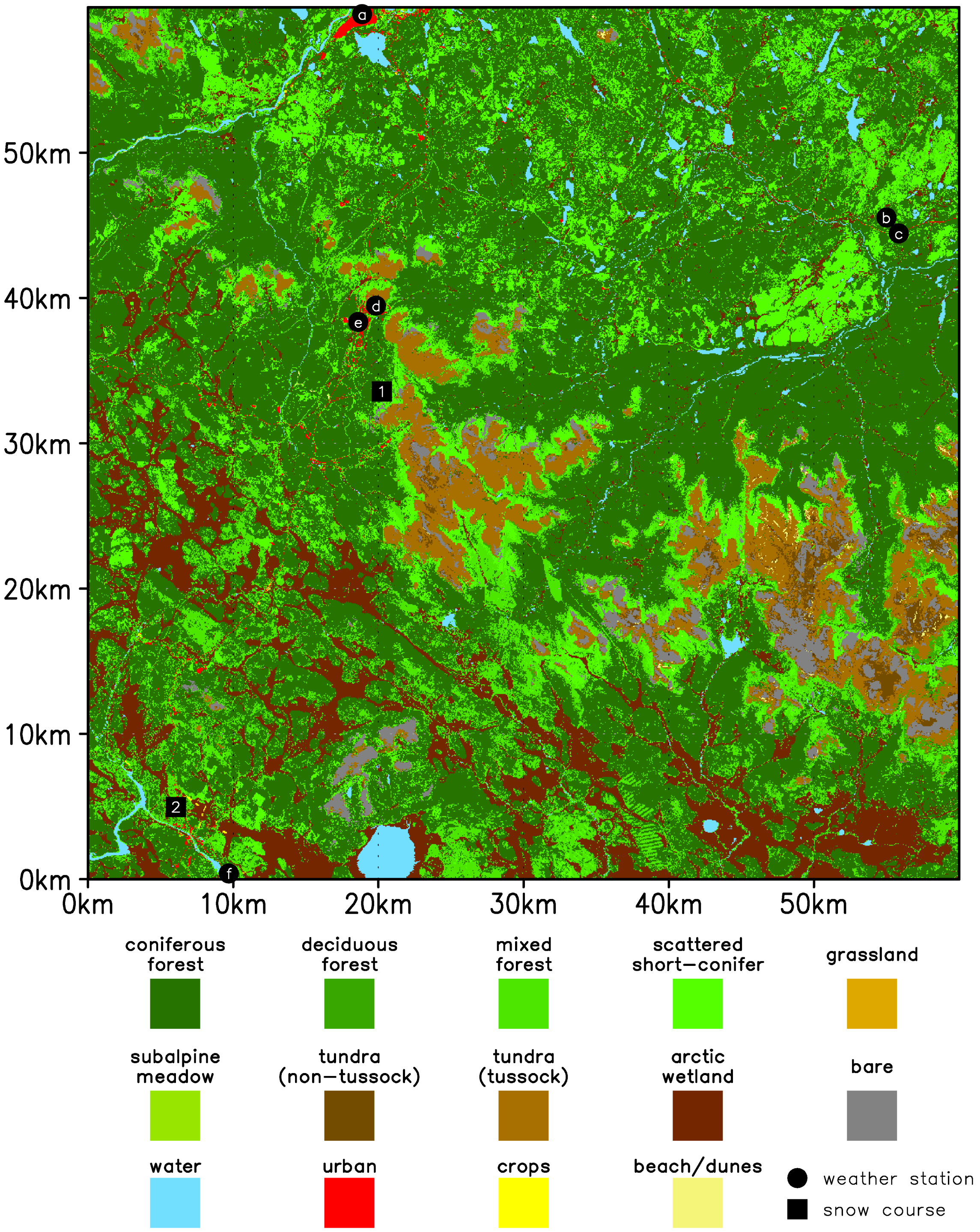

**Figure 3.4:** Distribution of different vegetation classes of the domain, together with the locations of the weather stations and the snow courses within the domain.

## 3.4 Meteorological data

The climate in the area of interest is temperate, belonging to the coniferous-mixed forest zone with cold, wet winters in the Köppen's climate classification. It is characterized by the prevailing westerly winds and the possibly rapid alternation of low and high pressure weather systems. (Finnish Meteorological Institute (Ilmatieteen laitos, FMI), 2017a).

There are five automatic weather stations (AWS) and one manual rain station within the study domain maintained by the Finnish Meteorological Institute (Ilmatieteen laitos, FMI). Their locations and measured variables are listed in Table 3.2, with increasing alphabetical ID from north to south. An AWS records meteorological variables every 10 minutes whereas a manual rain station only once a day (at 06 UTC) by a human observer (Finnish Meteorological Institute (Ilmatieteen laitos, FMI), 2017c).

**Table 3.2:** Meteorological data sites of the domain

| ID | Weather station | Easting (m) | Northing (m) | Elevation (m) | Variables[1] |
|---|---|---|---|---|---|
| (a) | Inari Ivalo lentoasema | 517095 | 7610935 | 140 | T,RH,W,D |
| (b) | Inari Raja-Jooseppi | 553215 | 7596943 | 253 | T,RH,W,D |
| (c) | Inari Raja-Jooseppi Kontiojärvi | 554058 | 7595846 | 185 | P,S |
| (d) | Inari Saariselkä Kaunispää | 518052 | 7590871 | 437 | T,RH,W,D |
| (e) | Inari Saariselkä matkailukeskus | 516829 | 7589748 | 302 | T,RH,P,S |
| (f) | Sodankylä Vuotso | 507915 | 7551796 | 248 | T,RH,W,D,P,S |

[1] Meteorological variables available at each site: T = air temperature, RH = relative humidity, W = wind speed, D = wind direction, P = precipitation, and S = snow depth.

The meteorological data is free and distributed by the FMI open data service. The retrieved data includes measurements of air temperature, relative humidity, wind speed (10-minute average), wind direction, and precipitation (hourly sum) from 1 August 2015 to 31 July 2016 (except the data for the AWS-(b) ends already on 27 July 2016), and covers well the study period, the winter 2015–2016. Some stations also provide snow depth data, which can be used later to assess the accuracy of the simulations. The subhourly AWS data was averaged to hourly and processed using the MicroMet preprocessor (Section 2.1.1). Before preprocessing the AWS data included only two major gaps: AWS-(e) had a 19-hour gap in precipitation, and AWS-(f) a 10-hour gap in wind speed and direction. Otherwise gaps in the AWS data lasted three hours or less. The data of the manual rain station (c) did not have gaps at all. For the simulations the daily precipitation values from the manual rain station (c) were halved and distributed with a 12-hour interval (06 and 18 UTC) to avoid using daily precipitation as an hourly forcing.

Figures A.1–A.6 in Appendix A show the daily values of observed meteorological variables for each station. A statistical summary is presented in Table 3.3.

**Table 3.3:** Basic statistics for air temperature, relative humidity, wind speed, wind direction, and precipitation observed at each station within the study domain over the study period. The last column lists the date of first snow (snow depth at least 1 cm), the start and end dates of permanent seasonal snow cover, and the length of the snow season in days derived from those two latter dates.

| ID | Fig. | | $T_a$ (°C) | RH (%) | $W$ (m s$^{-1}$) | $\theta$ | $P$ (mm) | $t_{snow}$ | |
|---|---|---|---|---|---|---|---|---|---|
| (a) | A.1 | min | -36.6 | 21.0 | 0.0 | | | | |
| | | max | 27.8 | 100.0 | 13.4 | | | | |
| | | avg[1] | 1.8 | 79.8 | 2.7 | SW | | | |
| (b) | A.2 | min | -32.9 | 22.0 | 0.0 | | | | |
| | | max | 27.4 | 100.0 | 12.7 | | | | |
| | | avg[1] | 1.8 | 83.5 | 3.2 | SW | | | |
| (c) | A.3 | min | | | | | 0.0 | first | 27 Oct 2015 |
| | | max | | | | | 50.0[2] | start | 6 Nov 2015 |
| | | avg | | | | | 1.7[2] | end | 4 May 2016 |
| | | sum | | | | | 635.2 | length | 181 d |
| (d) | A.4 | min | -29.1 | 23.0 | 0.0 | | | | |
| | | max | 25.6 | 100.0 | 21.0 | | | | |
| | | avg[1] | 0.8 | 86.6 | 6.3 | SW | | | |
| (e) | A.5 | min | -33.7 | 23.0 | | | 0.0 | first | 4 Oct 2015 |
| | | max | 26.7 | 100.0 | | | 7.8[3] | start | 7 Nov 2015 |
| | | avg | 0.9 | 83.5 | | | 0.1[3] | end | 6 May 2016[4] |
| | | sum | | | | | 639.0 | length | 182 d |
| (f) | A.6 | min | -39.4 | 22.0 | 0.0 | | 0.0 | first | 4 Oct 2015 |
| | | max | 27.1 | 100.0 | 8.5 | | 19.1[3] | start | 7 Nov 2015 |
| | | avg[1] | 0.9 | 85.0 | 1.9 | NW | 0.1[3] | end | 15 May 2016 |
| | | sum | | | | | 661.8 | length | 191 d |

[1] Dominant for wind direction

[2] Daily precipitation

[3] Hourly precipitation

[4] Snow on 9 June 2016 for approximately 24 hours due to a storm

## 3.5 Snow course data

The Finnish Environment Institute (Suomen ympäristökeskus, SYKE) operates approximately 150 snow courses around Finland. Snow courses are 2 to 4 km long trails along which snow depth and snow water equivalent measurements are made by a human observer covering terrains typical of the area in question. On a short snow course 50 snow depth measurements and 10 SWE weighings are made, whereas on a long snow course the number of measurements are 80 and 8, respectively. The vegetation type on the measurement location is also recorded on a long snow course. The measurements are done once or twice a month, more frequent measurements towards the spring. The measurements of each day are averaged to a single vegetation-weighted SWE value representing the whole snow course. Between the measurement days SYKE calculates the evolution of SWE for a snow course using a grid point model. These observations and modelled SWE values are freely available from the SYKE open data service. (Finnish Environment Institute (Suomen ympäristökeskus, SYKE), 2013; Sjöblom, 2015).

**Table 3.4:** Snow course sites of the domain

| ID | Snow course | Easting (m) | Northing (m) | Elevation[1] (m) | Length (m) | Measurements Depth | Measurements SWE |
|---|---|---|---|---|---|---|---|
| (1) | Inari Laanioja | 517153 | 7585239 | 340 | 2700 | 50 | 10 |
| (2) | Sodankylä Vuotso | 504238 | 7556354 | 260 | 2500 | 80 | 8 |

[1] Derived from the topography data

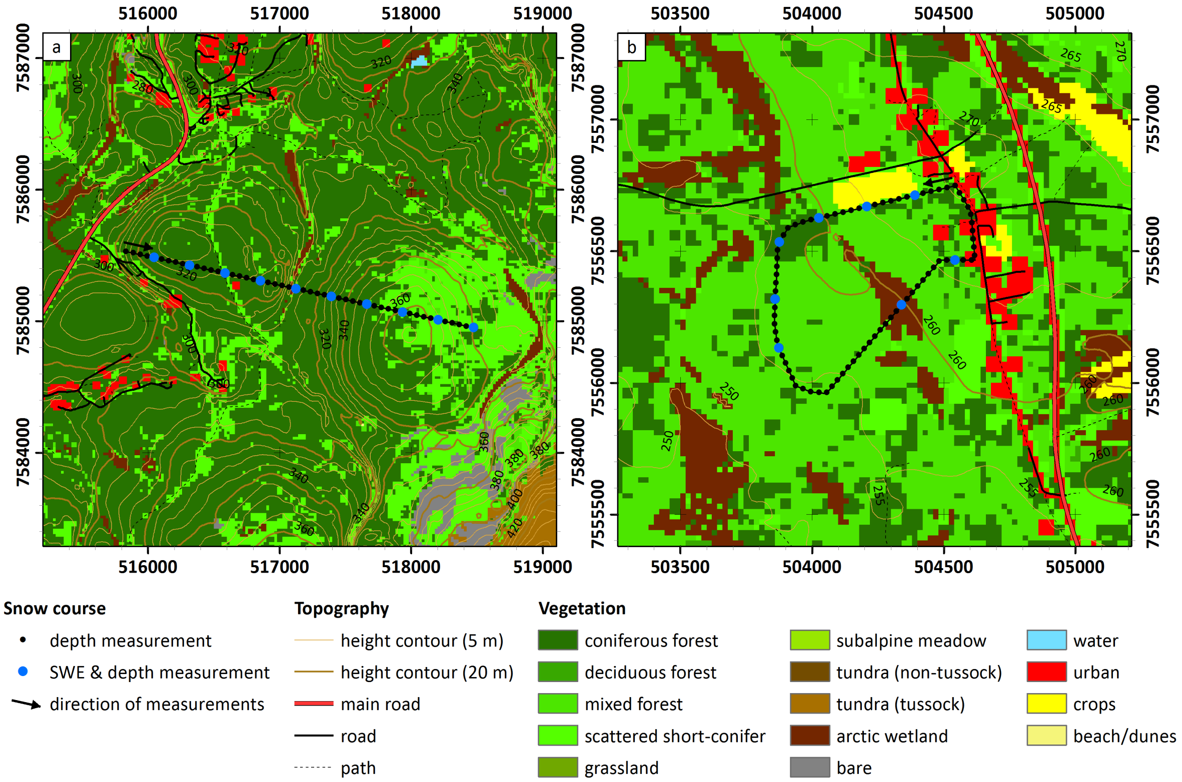

**Figure 3.5:** a) The snow course (1) in Laanioja, Inari. b) The snow course (2) in Vuotso, Sodankylä. The snow courses are marked with the approximate locations of depth and SWE measurements, height contours, roads, and vegetation. The coordinates are in UTM.

Within the study domain there are two snow courses: Inari Laanioja and Sodankylä Vuotso. Table 3.4 lists the location information of the two snow courses together with the number of measurements with increasing numerical ID from north to south. The snow course (1) is categorised as a short snow course, whereas the snow course (2) is regarded as a long snow course, although it has the lesser length of only about 2500 m. Hydrologist Heidi Sjöblom from the SYKE Freshwater Centre/Hydrological Monitoring provided the separate, non-averaged SWE values in addition to information about the route and the direction of measurements for both snow courses. The locations of snow depth and SWE measurements are put on a map assuming that the measurements are approximately equidistant (Fig. 3.5). The locations are not exact also for the reason that the measurements have to be done in undisturbed snow (Sjöblom, 2015). With the simulation grid size being 60 m by 60 m, the resulting error in location is assumed to be negligible and the equidistant measurement locations are used for assimilating the SWE values to the simulation.

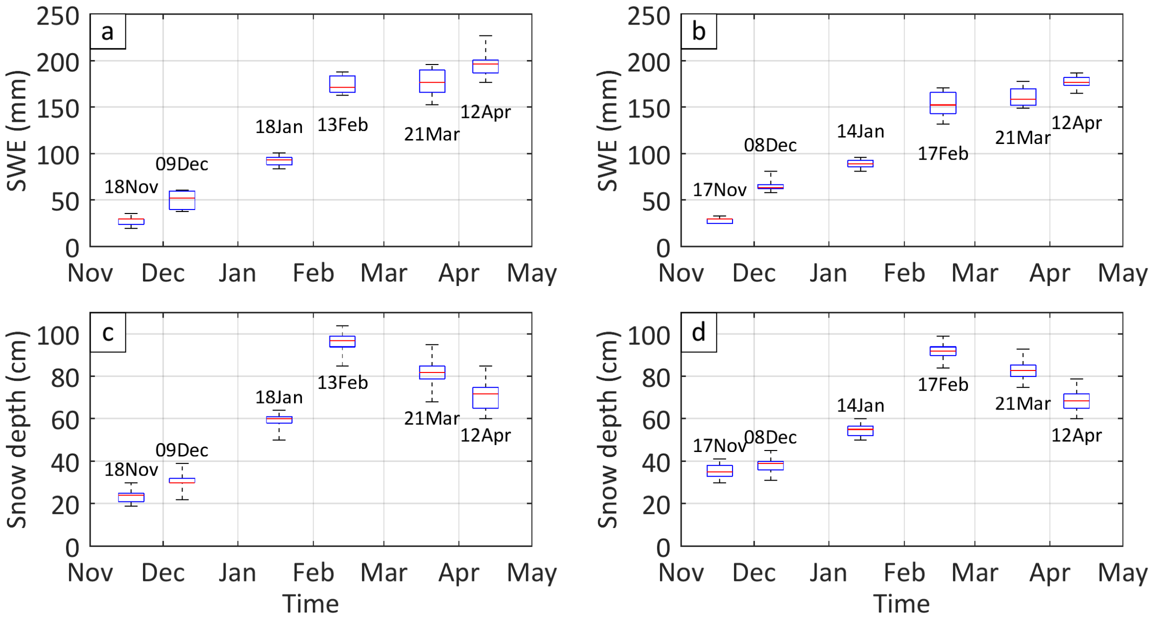

**Figure 3.6:** SWE observations at a) the snow course (1) and b) the snow course (2), and snow depth observations at c) the snow course (1) and d) the snow course (2). Due to numerous observations, the measurements are described with box plots. The horizontal red line is the median value, the box top and bottom represent the 75th and 25th percentiles, and the bars indicate the extreme values. The observations are marked with the date of the measurement in winter 2015–2016.

During the winter 2015–2016 there were six measurement days, and the observations are plotted with corresponding measurement points and dates in Figure 3.6. However, observations being so close in time (i.e. consecutive days) causes unrealistic corrections to precipitation when running the assimilation submodel SnowAssim (Liston, personal communication, 2017). To avoid overestimating the precipitation, the SWE observations are combined to produce data on observation dates 18 November 2015, 9 December 2015, 16 January 2016, 15 February 2016, 21 March 2016, and 12 April 2016. Shifting the observations forwards or backwards a maximum of two days is not regarded as such a significant modification that could alter the results more than for example a different observer doing the measurements would. Luckily, according to Sjöblom (personal communication, 2016), the measurer for both the snow course (1) and (2) is the very same in this case. The SWE observations are used with confidence to improve the accuracy of the simulation and to assess the need of SWE observations.

## 3.6 Simulations and analysis

The simulations cover the aforedescribed 60 km by 60 km domain and the time period from 1 August 2015 to 31 July 2016 with main interest in the winter season of 2015–2016. The modelling will include two simulation runs: first with only meteorological input data without SWE assimilation, and second with SWE assimilation to modify the original simulation to match the SWE observations. Table 3.5 lists the user-defined constants used in the simulations. The constants are mainly recommended default values, except for the curvature length scale, which is approximated from the topography data, and the typical snow density, which is adapted to the snow properties observed in Finland (e.g. McKay and Gray (1981); Rasmus (2013)). The simulations were run with a 60-m horizontal grid size and an hourly time increment storing end-of-day output values. With a rather standard desktop computer one simulation run took several hours and the assimilation run took double the time.

**Table 3.5:** User-defined constants used in the model simulations

| Description | Symbol | Value |
|---|---|---|
| Curvature length scale (m) | $\eta$ | 2500 |
| Topographic slope weighting factor | $\gamma_s$ | 0.58* |
| Topographic curvature weighting factor | $\gamma_c$ | 0.42* |
| Canopy gap fraction | $G$ | 0.2* |
| Cloud-cover fraction factor | | 1.0* |
| Threshold surface shear velocity (m s$^{-1}$) | $u_{*t}$ | 0.25* |
| Height of the wind observations (m) | $z_W$ | 10 |
| Height of the relative humidity observations (m) | $z_{RH}$ | 2 |
| Typical snow density (kg m$^{-3}$) | $\rho_s$ | 250 |
| Albedo for melting snow under forest canopy | $\alpha_{sf}$ | 0.45* |
| Albedo for melting snow in non-forested areas | $\alpha_{snf}$ | 0.60* |

* Default value

The model performance and the need of SWE observations will be assessed by comparing the original and assimilation simulation runs to the observed values considering amongst other things

- the temporal evolution of SWE and snow depth,

- the snow dates (first snow, length of the snow season, maximum SWE), and
- the snow occurrence on 9 June 2016.

In addition, the model gives information about sublimation and precipitation, which are notoriously difficult to measure.

# Chapter 4

# Results and discussion

This chapter includes the review of the simulation results, comparison to observations, discussion about results, and possible improvements together with future prospects.

## 4.1 SWE and snow depth

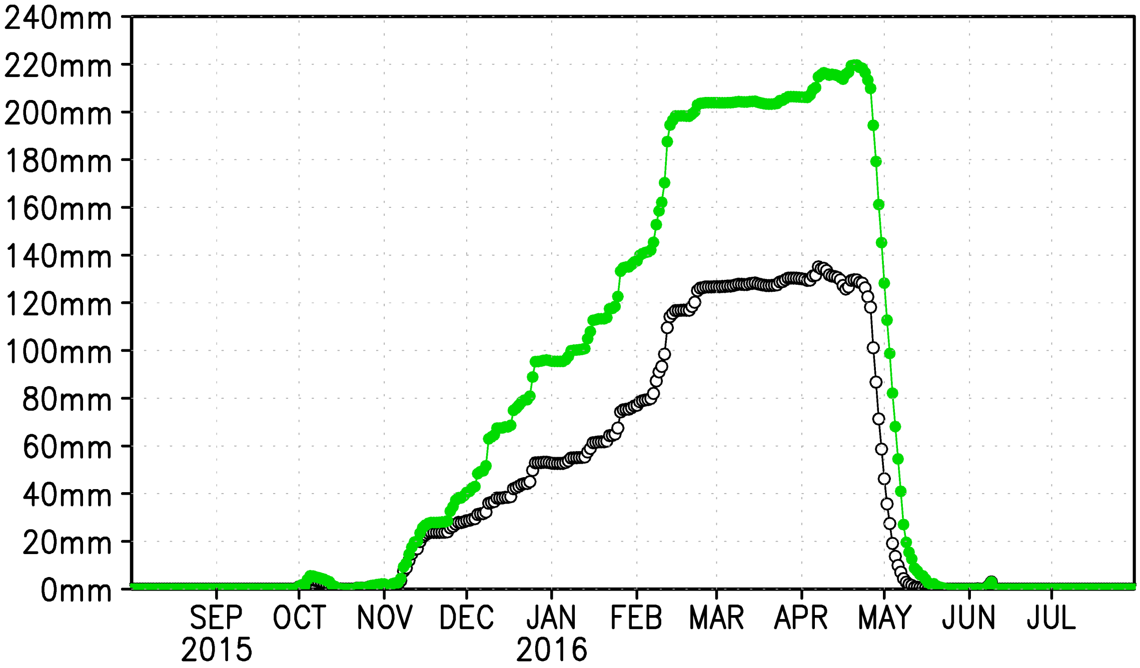

**Figure 4.1:** The simulated domain-averaged SWE in the assimilation run in green and without assimilation in black line.

The time series of domain-averaged snow water equivalent is shown in Figure 4.1. The first snow on 4 October 2015 is correctly simulated by both simulation runs. The permanent seasonal snow cover starts to accumulate in both simulations on 20 October

2015. Ablation starts in late April, and the snow cover has completely melted away on 25 May 2016 in the simulation without assimilation, and five days later on 30 May 2016 in the assimilation run resulting in snow season lengths of 218 and 223 days, respectively.

Figures 4.2 and 4.3 show the simulated SWE and snow depth evolution together with the observations at the snow courses and at the weather stations. Figures 4.2a)–4.2d) show the evolution at the midpoint of the snow course. The assimilated and non-assimilated SWE values differ the most by approximately 100 mm at the snow course (1) but only about 20 mm at the snow course (2). As expected, the simulated values of the assimilation run fall well within the range of the observations. The assimilated observations increase the SWE to the observed level except for the snow course (2) on 18 November 2015, when the model actually restricts the SWE evolution. The non-assimilated SWE values are far smaller, at most down to half the value, than the observed values at the snow course (1).

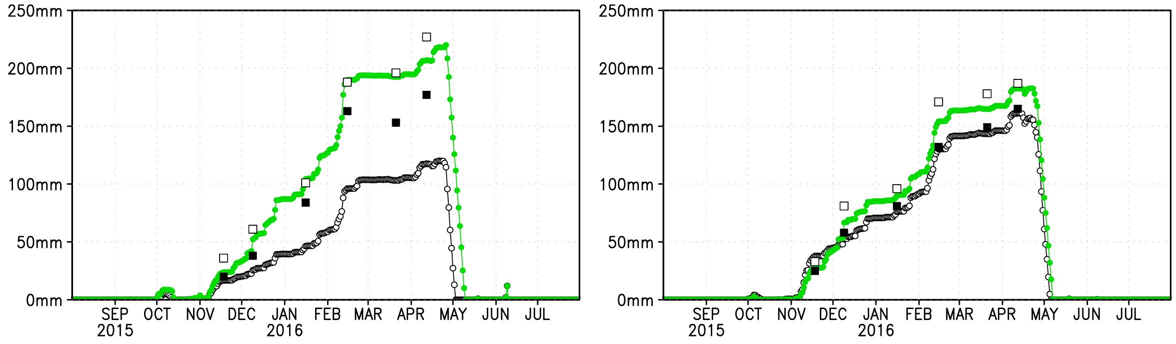

a) SWE at the snow course (1)

b) SWE at the snow course (2)

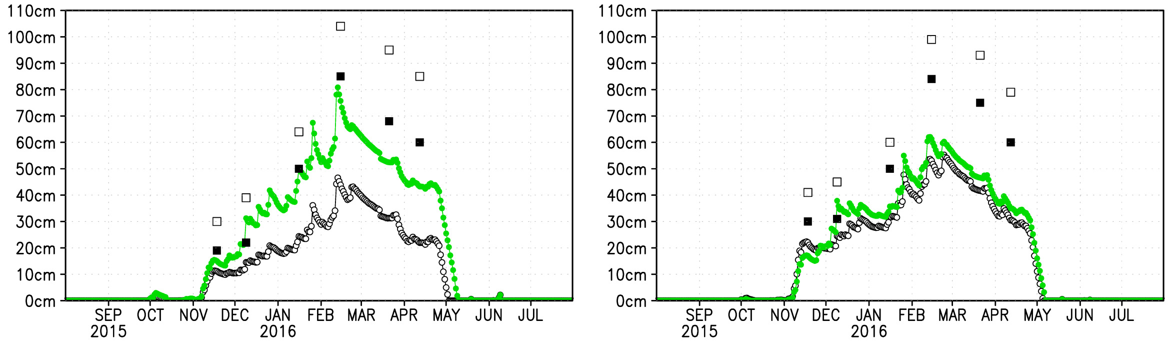

c) Snow depth at the snow course (1)

d) Snow depth at the snow course (2)

**Figure 4.2:** Simulated SWE in millimetres and snow depth in centimetres at the midpoint of the snow courses. The values of the assimilation run are marked with green and the values without assimilation are black. The observations are marked with squares: filled squares are the lowest values of the day and the open squares are the highest.

In the snow depth simulations the values fall below the observed values at almost any time of the winter, especially in spring after the maximum snow depth is reached. Also the selected simulated snow depth data show a peculiar spike and a subsequent low at the end of January, which are not present in any of the observations. At the manual weather station (c) (Fig. 4.3a)) the simulated permanent seasonal snow cover start and end dates are correct, but maximum occurs slightly earlier than the observed. The snow depth evolution during the accumulation period is quite accurate, and the maximum depth of the assimilation run is almost the same. At the AWS-(e) (Fig. 4.3b)) the timing of the first snow, the start and end of the permanent seasonal snow cover, and the maximum snow depth are simulated rather well. There is another strange feature, a sudden loss of snow depth, at the beginning of January, which is not evident in the observations. In the simulation without assimilation the snow depth decreases erroneously really close to zero. The timing of the snow season beginning is also correct at the AWS-(f) (Fig. 4.3c)), and the snow depth results of the two simulations differ only by 5 cm at most. However, the spring melt is simulated to be two weeks faster than the observed due to the drastically underestimated snow depth in the simulation.

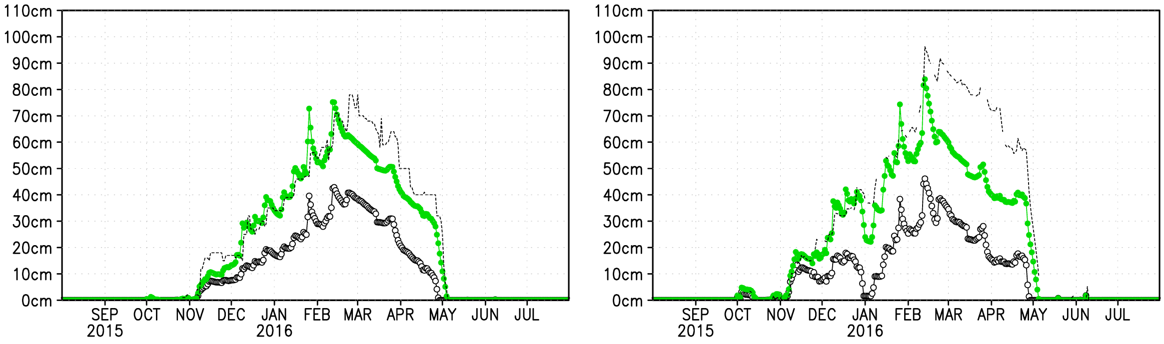

a) Snow depth at the manual weather station (c)

b) Snow depth at the AWS-(e)

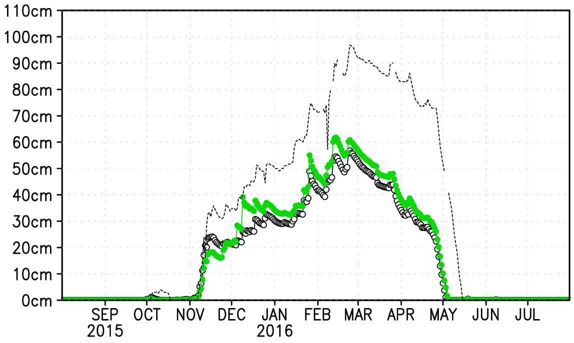

c) Snow depth at the AWS-(f)

**Figure 4.3:** Simulated snow depth values in centimetres at the weather stations, where the green line is the assimilation run and the black line is the simulation without assimilation. The observed snow depth is marked with the dashed line.

All in all, the snow depth does not look like a reliable variable to compare the simulation results to observations, except perhaps for the timing of major changes during the accumulation period. This is caused by the fact that in the model SWE is converted to snow depth with a simple density ratio (Eq. 2.52) and the model runs used in this study include only two layers of snow (a soft movable layer of new snow at the surface and the rest is hard immobile snow). In reality, the layering of snow is much more complex. Also, the snow depth observations represent only that one point in question and the spatial variability of snow depth is known to be significant.

It is clear that the simulation without assimilation significantly underestimates also the SWE values during the permanent seasonal snow cover. The overall evolution pattern is similar in both simulations, but the difference in SWE increases towards the spring. The domain-averaged maximum, the end-of-winter SWE value is reached in April. The simulation run without assimilation gets its highest value, 300 mm, on 7 April 2016 (Fig. 4.4a)), whereas the assimilation run reaches its peak, 450 mm, a whole two weeks later on 21 April 2016 (Fig. 4.4b)). This is due to the fact that there are assimilated SWE observations after the maximum SWE value of the first simulation run on 12 April 2016. The patterns in the simulated SWE distributions are also similar, higher elevations have higher SWE values than the lower elevations, but the range of values is larger in the assimilation run. The SWE contours also follow closely the different vegetation types depicting more snow in open areas than in forests (cf. Fig. 3.4). The difference between the SWE values of the two simulation runs decreases towards the south-west corner of the domain (Fig. 4.4c)). That can also be seen when comparing the simulated SWE values of the two snow courses (Figs. 4.2a) and 4.2b)).

The winter 2015–2016 included one snowfall event after the permanent seasonal snow cover had already completely melted away. The AWS-(e) records snow on ground from 9 June 2016 at 02 (UTC+3) until 10 June 2016 at 02 (UTC+3) (not shown). Figure 4.5 shows the simulated SWE on that day, with which both simulation runs concur. Snow had accumulated on higher elevations on the northwest-southeast line through the domain. The snowfall is also present in the snow depth simulation results of the AWS-(e) (Fig. 4.3b)), although the amount of snow is less than the observed, and in the SWE simulation of the snow course (1) (Fig. 4.2a)).

To assess the simulation results more closely, a cross-section was chosen at the 50 km line in the east-west direction from 0 km to 30 km in the north-south direction near the date of the maximum SWE value (Fig. 4.6). The simulated SWE is varying as expected: lower values of SWE correspond to forested low elevation areas (vegetation classes 1–5) and higher values to open high elevation areas (vegetation classes 12–24). The areal difference between the assimilation run and the simulation run without assimilation is clearly visible in the cross-section, too: the difference of the SWE curves increases from the south (left in the figure) to the north (right in the figure), approximately from 50 mm to 100 mm.

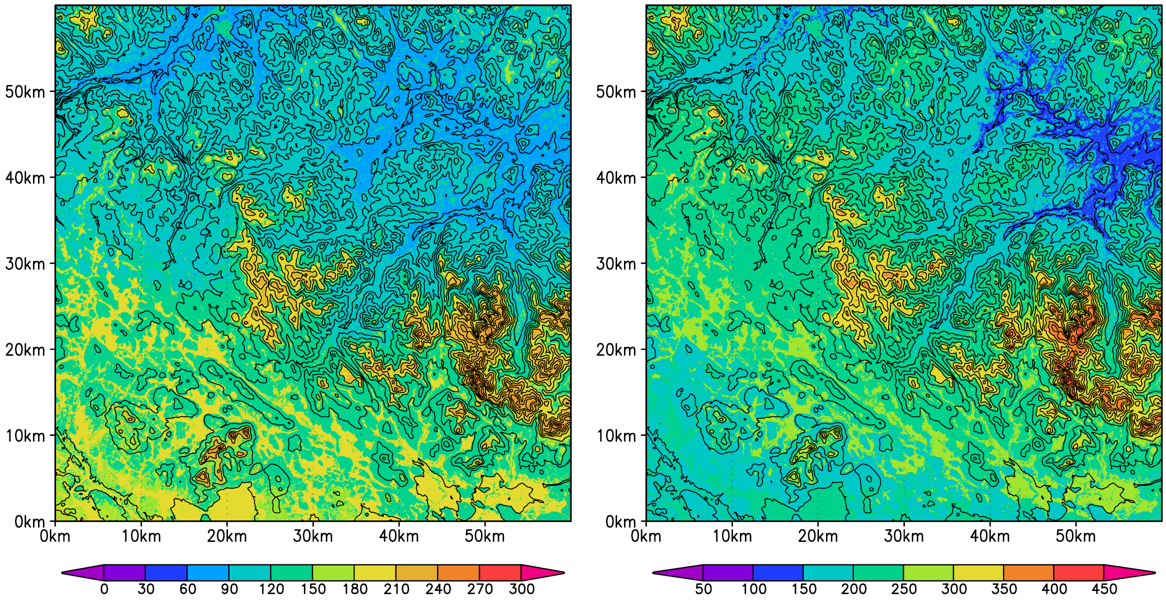

a) Without assimilation 7 April 2016

b) With assimilation 21 April 2016

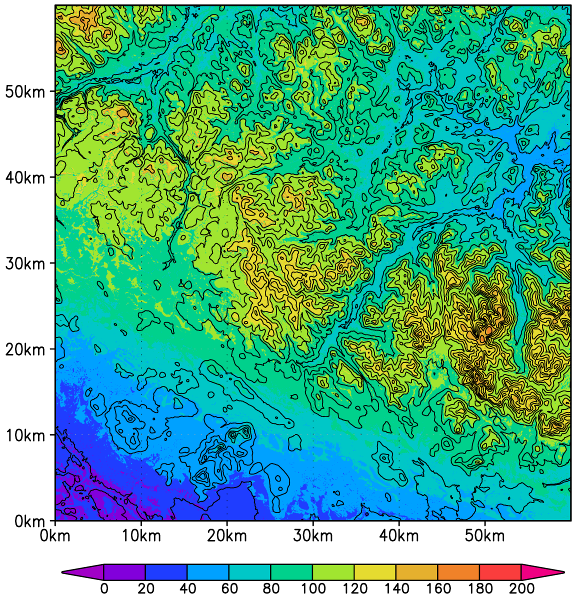

c) Difference between the end-of-winter SWE values, b)-a)

**Figure 4.4:** The simulated end-of-winter SWE distribution in millimetres. The black contours represent the topographic elevation with 50 m increment.

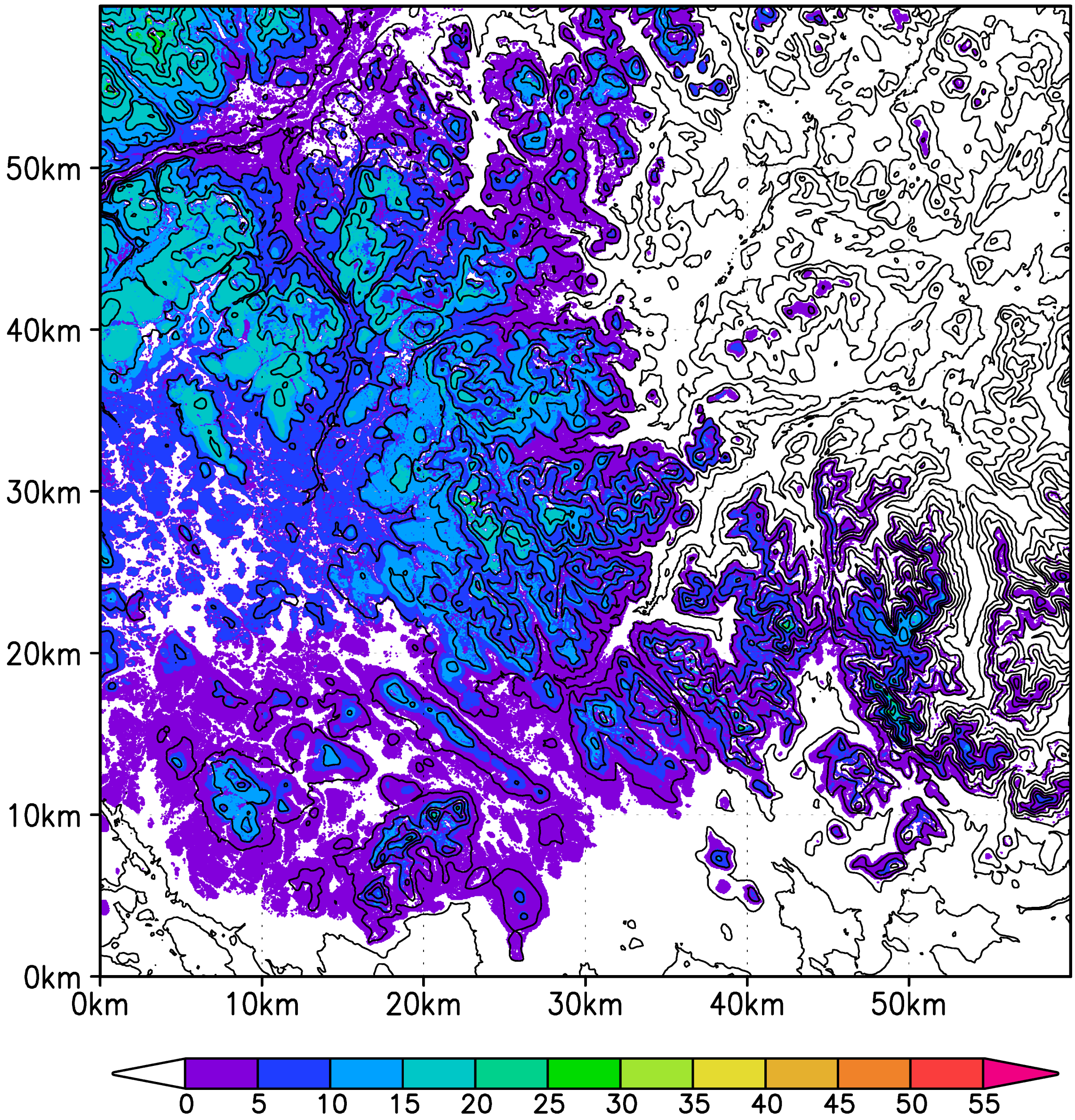

**Figure 4.5:** The simulated SWE in millimetres accumulated by the snowfall on 9 June 2016 after the permanent snow cover had already melted away. The black contours represent the topographic elevation with 50 m increment.

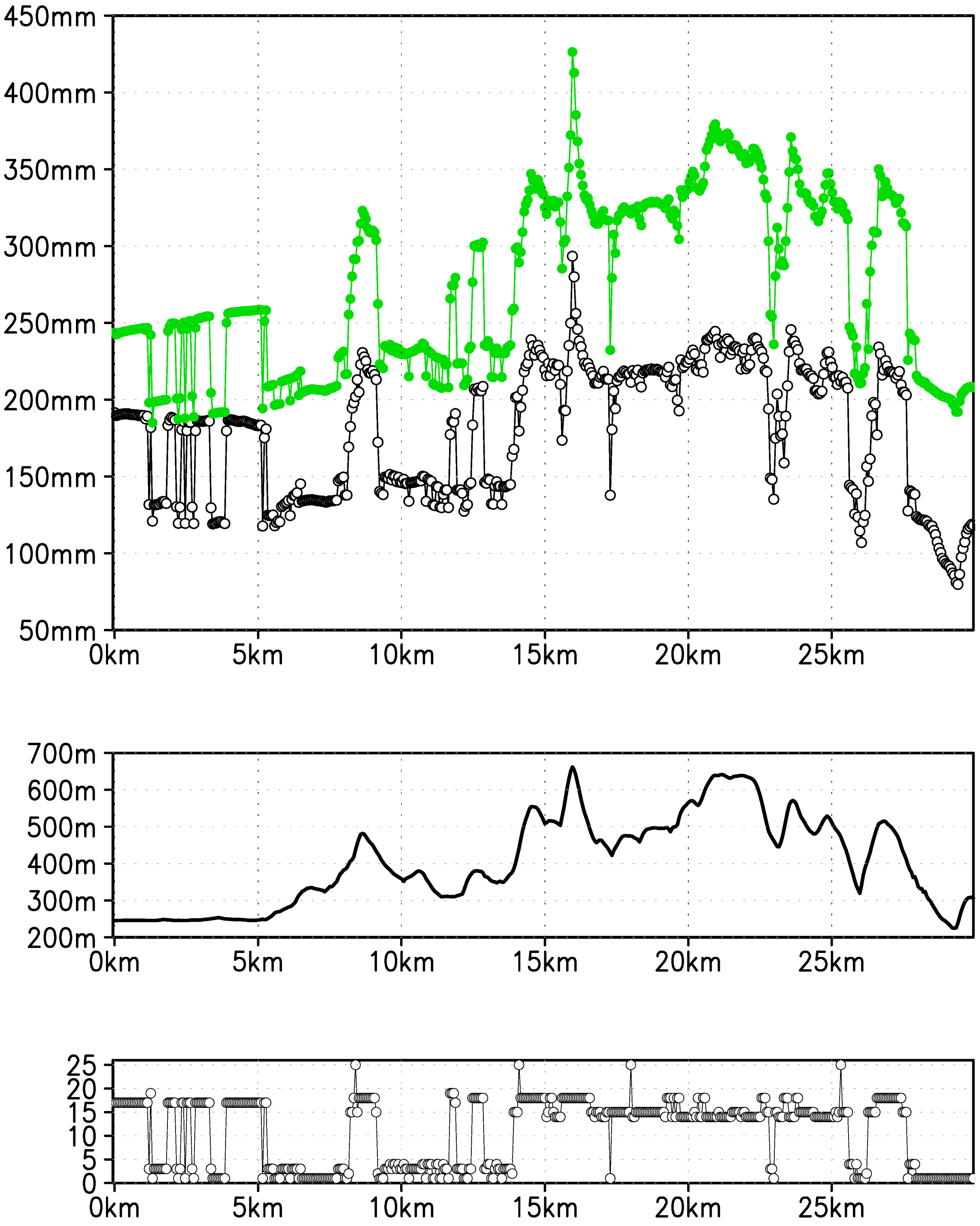

**Figure 4.6:** The top figure shows the simulated SWE of the cross section (location described in the text) on 15 April 2016. The green line is the assimilation run and the black line represents the values without assimilation. The curve in the middle figure is the topography of the cross section and the bottom figure shows the corresponding vegetation class code of the grid cell.

## 4.2 Precipitation and snow transport

Possible ways for SWE to increase are precipitation and snow transportation. Figure 4.7a) shows the summed precipitation distribution of the assimilation run. It varies between 690 and 930 mm in the domain, the highest values located around the highest elevations. The Finnish Meteorological Institute's interpolated annual precipitation observations in the area shows values between 560 mm to 740 mm in 2015 and 2016 (Finnish Meteorological Institute (Ilmatieteen laitos, FMI), 2017b). Because the assimilation submodel SnowAssim adjusts only the precipitation (or melt), the precipitation values shown in the figure represent the precipitation needed to replicate the observed and assimilated SWE values in the model. Figure 4.7b) tells that summed precipitation of the assimilation run is 2 % to 18 % greater than the total precipitation using the interpolated forcing from the weather stations, indicating the well-known difficulty to measure precipitation especially in winter. This figure explains nicely why the SWE and snow depth values of the different model runs differ more in the north than in the south, as the precipitation correction due to the assimilation is increasing towards northeast.

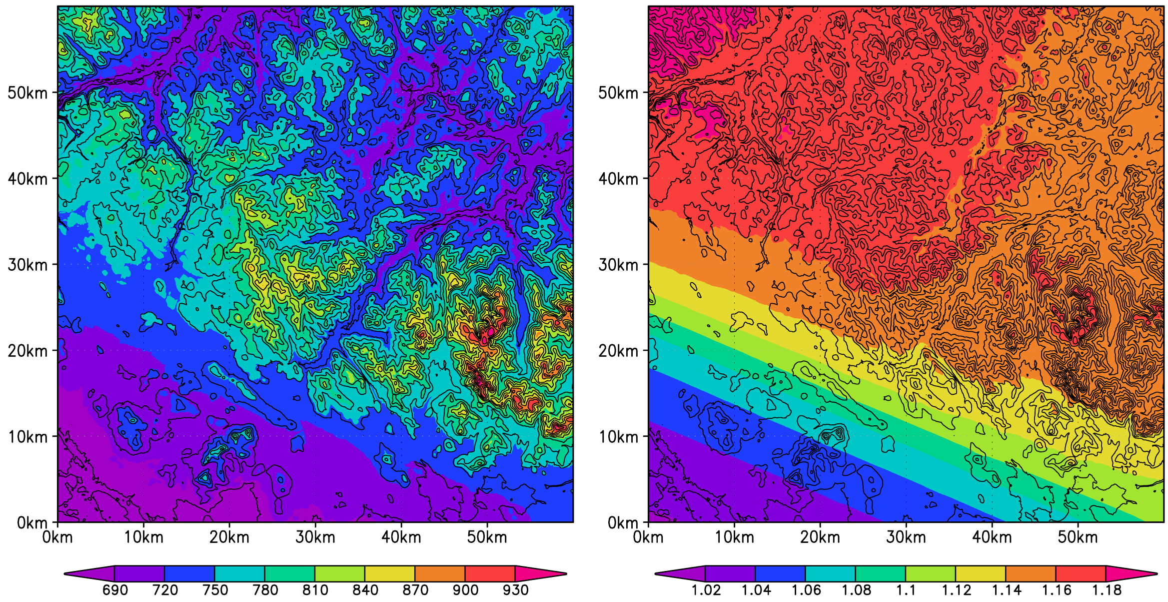

a) Precipitation with correction/assimilation in millimetres

b) Ratio for summed precipitation, $\frac{\sum P_{assim}}{\sum P}$

**Figure 4.7:** The simulated total precipitation and precipitation correction distributions. The black contours represent the topographic elevation with 50 m increment.

Part of the precipitation is intercepted and stored by the forest canopy. It was expected to play a major role, since the study domain is mainly covered in forests. The canopy-intercepted snow can be unloaded down to the surface induced by melting (Fig. 4.8) or sublimated back to the atmosphere. Over the simulation period up to 50 mm is added to the snow pack by unloading, and the largest values concentrate on the Ivalojoki river valley in the northwest of the domain probably due to more variable temperature and therefore more extensive melt. Approximately double the unloaded amount of the canopy-intercepted snow is actually sublimated (described in the next Section 4.3).

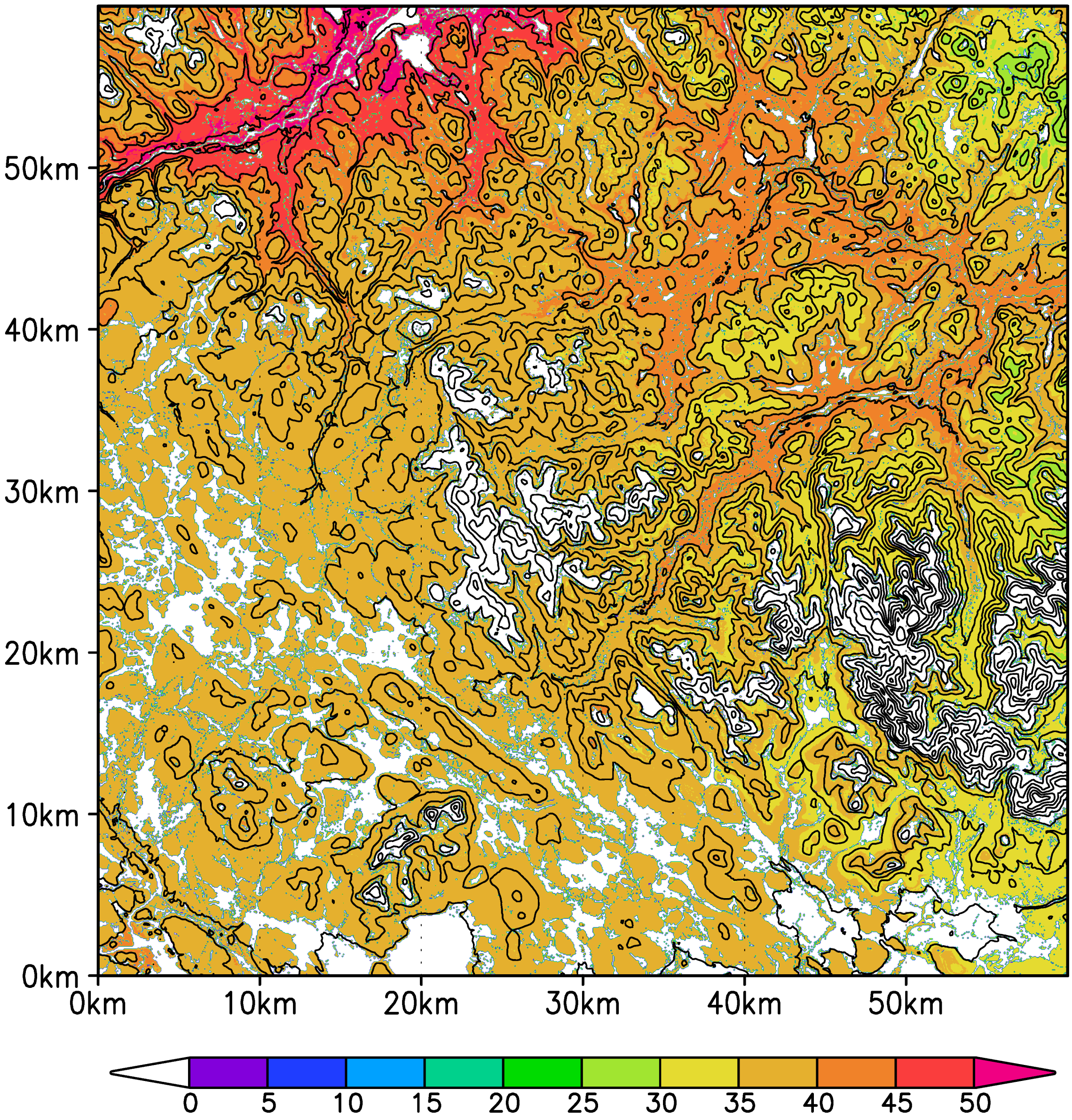

**Figure 4.8:** Simulated assimilation run canopy unloading distribution in SWE millimetres summed over the simulation period. The black contours represent the topographic elevation with 50 m increment.

The simulated blowing-snow transport summed over the period in a close-up area is shown in Figure 4.9. The negative values are shown in blue colours and mean snow ablation due to snow transport, and the positive values are red meaning snow accumulation. During the simulation period the blowing-snow transport varies between -150 mm to 90 mm. The dominant wind direction is the southwest, which is evident also in the ablation-accumulation patterns. The slopes facing southwest are mainly losing snow to wind

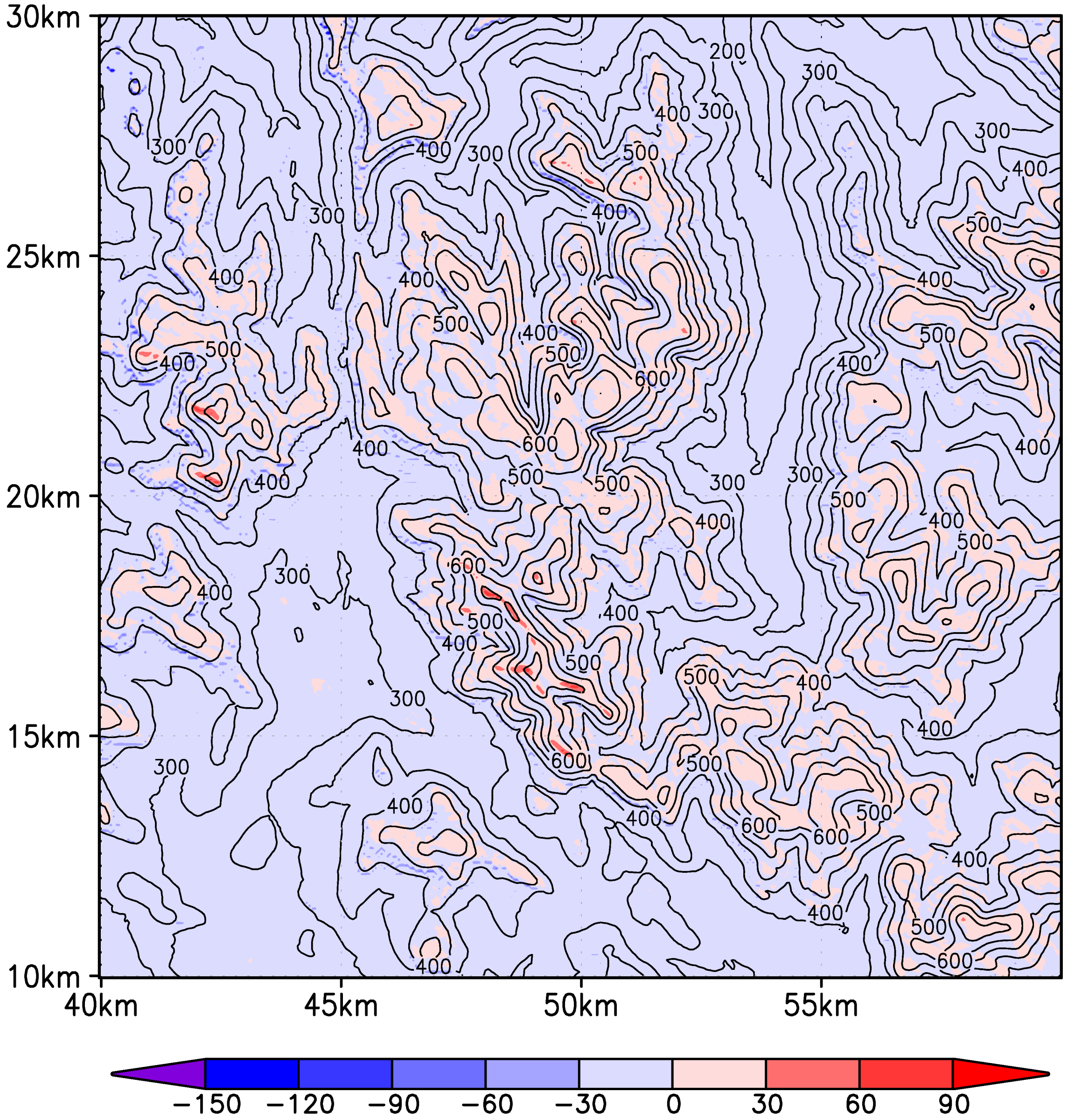

**Figure 4.9:** A close-up of the simulated blowing-snow transport distribution in SWE millimetres summed over the simulation period in the assimilation run. The dominant wind direction is the southwest. The black contours represent the topographic elevation with 50 m increment.

transport, and the snow is deposited on the lee side of the slope resulting in snow gain. In most areas the ablation and accumulation effects of the blowing-snow transportation balances out to approximately zero with this grid cell size, also considering the fact that the fetch lengths are not significant in the domain.

## 4.3 Melt and sublimation

Phenomena decreasing SWE include snow transportation, melting, and sublimation, of which the snow transportation is described in the previous section.

Figure 4.10a) shows the assimilation run melt distribution summed over the study period together with the ratio to the non-assimilated melt distribution in Figure 4.10b). The domain experiences total melt of 300 mm in the low elevations up to 850 mm in the high elevations, which is 10 % to 70 % more than what is needed to melt the snow cover simulated without assimilation. The simulated melt pattern is naturally similar to the SWE distribution (cf. Fig. 4.4). The ratio between the melt distributions of the simulation runs resembles closely the similar variable of precipitation ratio in Figure 4.7b) increasing in the northeast.

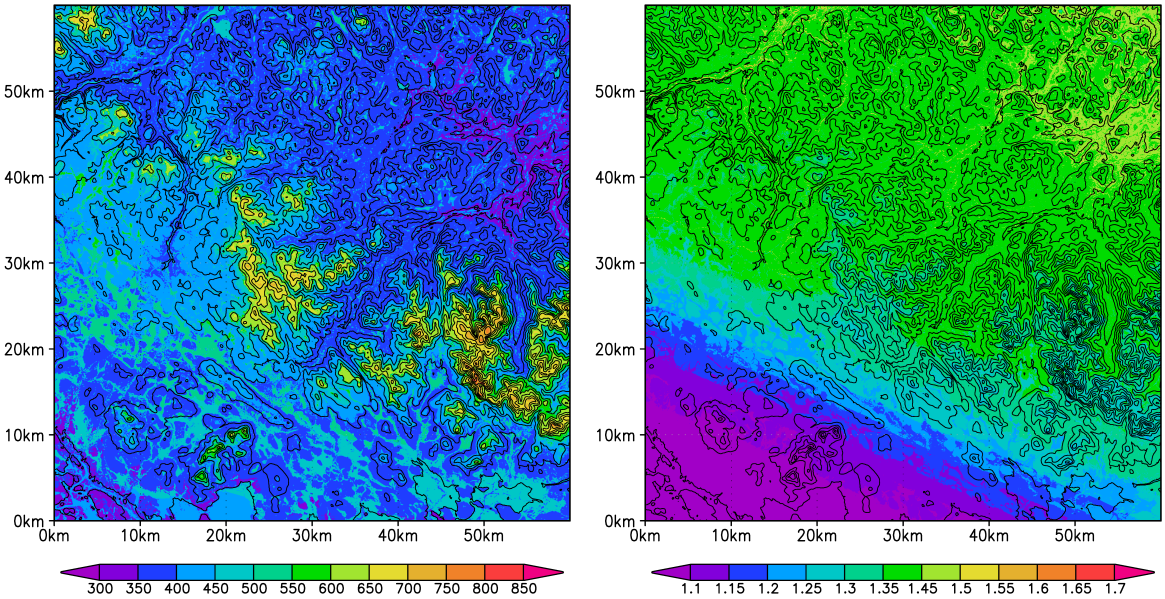

a) Melt with correction/assimilation in SWE millimetres

b) Ratio for summed melt, $\frac{\sum M_{assim}}{\sum M}$

**Figure 4.10:** The simulated melt and melt correction distributions summed over the simulation period. The black contours represent the topographic elevation with 50 m increment.

Figures 4.11a)–4.11c) show the three components of sublimation: blowing-snow, static-surface and canopy sublimation, respectively. The static-surface and blowing-snow sub-

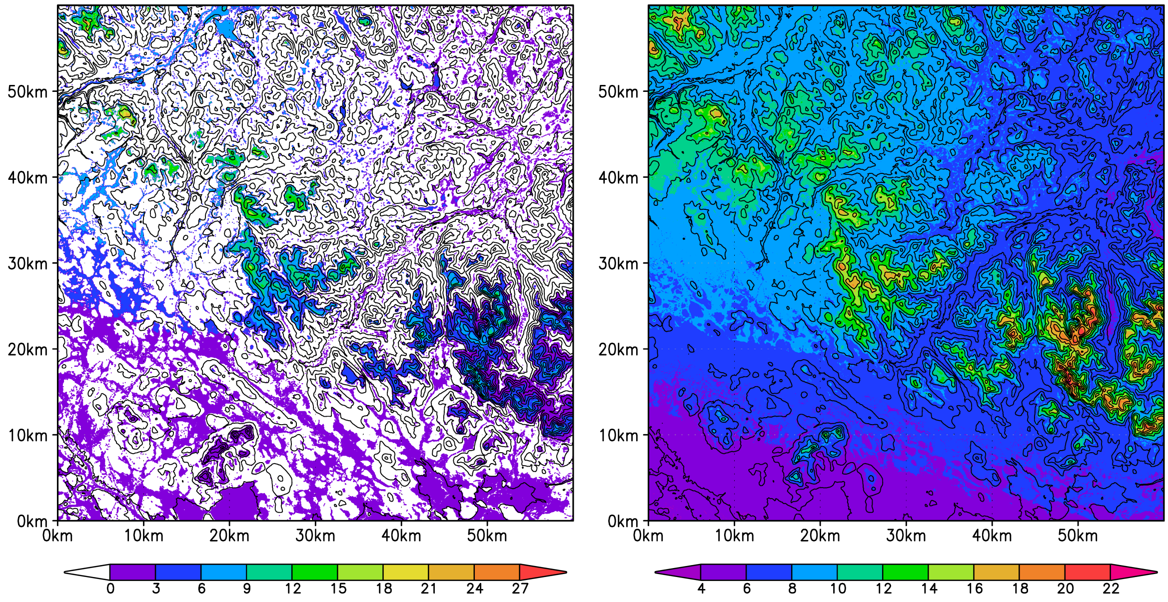

a) Blowing-snow sublimation

b) Static-surface sublimation

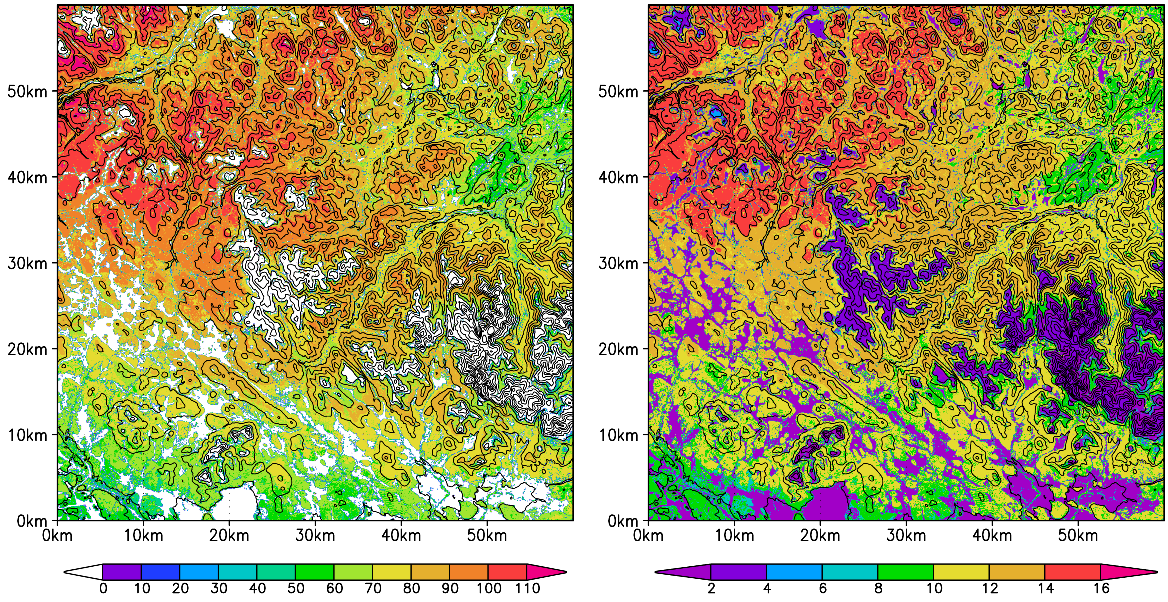

c) Canopy sublimation

d) Sublimation-to-precipitation fraction in %

**Figure 4.11:** The simulated sublimation loss distributions in SWE millimetres summed over the simulation period, positive values meaning loss of snow from the surface. Figure d) shows the ratio of the summed total sublimation to summed precipitation. The black contours represent the topographic elevation with 50 m increment.

limation are the same magnitude, under 30 mm. The blowing-snow sublimation has much smaller areal influence, because the snow depth does not exceed the vegetation holding depth in forest, hence there is no blowing-snow sublimation. However, areas affected by the wind transport experience sublimation that is roughly equal in magnitude to static-surface sublimation. In open areas the combined effect of the two equals up to a 45-mm loss through sublimation. In addition, the canopy-intercepted snow sublimates reaching values up to 110 mm, which is more than double the aforementioned combined sublimation that originates from the snow pack surface. Forests dominate the vegetation, they are exposed to higher wind speeds and they receive more radiation than the snow underneath the forest canopy, which explains the difference in magnitude. Also, the default values of the variables describing the intercepting canopy in the formulation might not be accurate in the study domain. The fraction of the total precipitation that sublimated varies between 2 % and 16 % (Fig. 4.11d)), and is at most 5.8 % if excluding the canopy sublimation (not shown).

## 4.4 Discussion

The simulation results, including the values and the distribution patterns, are mainly physically sensible. The SWE values are the most reliable, because observations were available for comparison and assimilation. After SWE assimilation the timing of the end-of-winter maximum SWE and the SWE values were significantly improved. In the initial simulation run without assimilation the results are not reliable. The model simulates the presence of snow quite accurately, the timing of first snow better than the melt of snow, which is dependent on the amount of snow.

The snow depths were almost constantly underestimated, because the model simulations were run with only two layers in the snow pack and the real stratigraphy is much more complex. This could be improved by running the simulation in multilayer configuration, however it does take more computational resources.

The model suggests that the measured precipitation is not adequate to accumulate the observed SWE, which was expected given how difficult it is to measure solid precipitation. The accuracy of simulated sublimation or canopy-intercepted snow is hard to assess, since there are no observations available. However, sublimation estimates could be enhanced by allowing temporally varying threshold surface shear velocity $u_{*t}$, which is available in the model but a constant value was chosen for this study.

Liston and Elder (2006a,b) mention that MicroMet and SnowModel include many limitations and simplifications, though the work for model development is still ongoing. The majority of the modifications made to the meteorological fields is due to simple topographic relationships, which act without any feedback between the atmosphere and the ground, and which are highly reliable on the various lapse rates. The simulated canopy-intercepted-snow sublimation rate is often over- or underestimated, but during summation it usually balances out, which is why only the summed sublimation values were studied earlier.

In Liston and Elder (2006a) it was supposed that the underestimation of simulated subcanopy solar radiation in summer and overestimation in spring and autumn could be related to the vegetation-dependent extinction coefficient $k$ (i.e. canopy structure) and its dependence on the solar zenith angle. This suggests that the coefficient $k$ could depend also on the forest type, although it is a constant in the model. Additionally, the model assumes a uniform single-type vegetation in a grid cell, which is not reality. Using canopy gap fraction $G$ is an attempt to allow solar radiation penetrate the forest canopy without modification. Varying vegetation can also affect the near-surface atmospheric conditions.

Many of the constants used in the model are left in their default value, for example the monthly lapse rates, and the weighting factors for slope and curvature, in addition to the earlier mentioned vegetation-dependent extinction coefficient $k$ and the canopy gap fraction $G$. Maybe one of the biggest deficiencies in the model might be the coarse constant values for albedo. The dry snow albedo is 0.8, whereas melting snow has values 0.6 and 0.45 for open and forested areas, respectively, glacier ice has albedo of 0.4 and vegetation 0.15. In many other respects the model seems to be built in a highly sophisticated way using physical and empirical relationships.

It is axiomatic that decreasing the grid cell size would increase the resolution and possibly increase the accuracy, but that can only be done with more computational resources. The accuracy of the simulation could be made better by using for example more frequent SWE observations for assimilation both spatially and temporally; observations of pressure and solar and longwave radiation to also assimilate into the model; temperature and relative humidity observations at 700 hPa level for cloud fraction calculation; spatial and temporal data of the lapse rates; and spatially detailed vegetation data including vegetation height, canopy gaps and forest effect on radiation to mention a few. With these corrections the model could produce more accurate results without assimilation and be used for example for forecasting the timing and magnitude of the spring runoff and the possibility of floods. Then it would be also convenient to model for example the effect of global warming on snow cover by just adding a shift or trend to the atmospheric forcing variables.

# Chapter 5

# Conclusions

In this thesis the winter 2015–2016 in the Saariselkä region in Northern Finland was studied using the spatially distributed high-resolution snow-evolution modelling system SnowModel. The model uses air temperature, relative humidity, wind speed, wind direction, and precipitation as input together with topography and vegetation data to produce a wide variety of snow cover related output variables, such as SWE, depth, density, sublimation, melt, and snow transport to name a few. The main objective was to assess the model performance in a 60 km by 60 km domain including varying topography and vegetation. The secondary aim was to put together the theory of SnowModel and the high-resolution meteorological distribution model MicroMet. The objectives set for this thesis work were achieved.

The simulations were run first with only available meteorological forcing data and then assimilating available SWE observations. The simulation results show that the simulation run without assimilation underestimates the results, especially in high elevations and in the northern part of the domain. Assimilating SWE observations enhanced the SWE results and the timing of SWE changes. Both simulations replicate the first snowfalls correctly, including the late snowfall on 9 June 2016, however they constantly underestimate the snow depth.

The study domain got first snow on 4 October 2015 and the permanent seasonal snow cover started accumulating on 20 October 2015, which agree with the observations. The snow season started to end locally at the beginning of May 2016, and the whole domain is snow-free at the end of May 2016. On 21 April 2016 the domain-averaged SWE reached its maximum of 220 mm, peaking locally in higher elevations at 450 mm, which was two weeks later than in the initial simulation run without assimilation. The simulated SWE values show the expected elevation and vegetation dependencies. Ablation by blowing-snow transport is present on slopes facing the dominant wind direction southwest.

The modified precipitation of the assimilation run suggests that up to 18 % more precipitation is needed to replicate the SWE observations compared to the interpolated observations. The precipitation correction increases towards the northeast of the domain, and a similar increasing pattern can be noted also from the difference between the SWE values of the two simulation runs. The needed melt in the assimilation run is locally as much as 70 % larger than the initial simulation.

The model results include also canopy unloading and three sublimation components, however there are no observations to compare them with. Blowing-snow sublimation occurs on open areas and its summed value reaches 27 mm locally. The sublimation from the surface of the snow cover takes place everywhere in the domain and it sums up to 4–22 mm with largest values in open areas. The summed canopy sublimation values are multiple compared to the other two sublimation components peaking at 110 mm. Together the sublimation processes return up to 16 % of the precipitation back to the atmosphere over the study period.

To conclude, SnowModel performs well in the study domain provided that there are SWE observations available for assimilation. The need of SWE observations was proven essential, but additionally their timing was noted to be crucial. Observations help especially to simulate the end-of-winter maximum SWE values and their timing, so more frequent observations towards the spring are suggested. The model results could be improved already in the model's current state by running it in a more complex configuration. However, a model is always a simplification of the real world and the models used in this study include them too. There is a lot of room for improvement, for example changing the hard-coded constants to better suit the conditions observed at the study domain. This also acquires more detailed data from the study domain than what was used in this study. These modifications and additions could allow the model to produce reliable results already without assimilation.

# Acknowledgements

The work for the thesis was done as a part of the project Modeling of the active surface layer of Himalayan glaciers (268107) funded by the Academy of Finland.

First and foremost I want to thank my supervisor, professor Matti Leppäranta, for introducing me to the wonderful world of geophysics, especially snow and ice. I am forever grateful that you asked me to join your research group. Thank you for the numerous interesting duties and challenging responsibilities this work has included and for the freedom with which you allowed me to carry them out. I appreciate all the advice and guidance over the years and with the thesis work.

Dr Glen E. Liston, to you I am probably as grateful as to my supervisor. Thank you for agreeing to meet me in Tromsø, for allowing me to use SnowModel, and especially for patiently giving advice and answering my questions innumerable times in spite of me being green in modelling.

Hydrologist Heidi Sjöblom from the Finnish Environment Institute provided the detailed snow course observations, which made the assimilation simulation possible and more reliable. The cooperation and handing over the data is very much appreciated.

The final push to finish the thesis started at the Kilpisjärvi Biological Station of the University of Helsinki during a scholarship period at the end of February 2017. I thank the University of Helsinki for this grant and the station staff for providing the excellent board and lodging in the sunny arctic.

MA Katariina Vihervalli checked the language of this thesis with due care. I thank Katariina for continuing the era of the Vihervalli sisters checking the language of my theses.

I want to thank all of my dear friends, especially my fellow students MSc Katriina Juva and MSc Elisa Lindgren and the lunch group in Dynamicum, for peer support. Studying the life cycle of a snow flake would not have been as fun without you. My beloved student organisation Pohjois-Pohjalainen Osakunta and its people have given me many great friends, lots of joy, and something else to think about besides studying, for which I am very grateful.

I appreciate the endless support and encouragement from my parents, brother, and relatives. Above all, I thank my mum and dad for choosing snow-rich Inari as their place of residence to raise a family, the place I to this day call home.

# Bibliography

Abele, G. and Gow, A. J. (1975). Compressibility characteristics of undisturbed snow. Technical Report 336, U.S. Army Cold Regions Research and Engineering Laboratory, Hanover, New Hampshire.

Anderson, E. A. (1976). A Point Energy and Mass Balance Model of a Snow Cover. *NOAA Technical Report,* **NWS-19**.

Barnes, S. L. (1964). A Technique for Maximizing Details in Numerical Weather Map Analysis. *Journal of Applied Meteorology,* **3**(4), 396–409.

Barnes, S. L. (1973). Mesoscale objective map analysis using weighted time-series observations. Technical Report NOAA-TM-ERL-NSSL-62.

Bartelt, P. and Lehning, M. (2002). A physical SNOWPACK model for the Swiss avalanche warning: Part I: numerical model. *Cold Regions Science and Technology,* **35**(3), 123–145.

Berg, N. H. (1986). A deterministic model for snowdrift accumulation. In *Proceedings of the International Snow Science Workshop, Lake Tahoe, California,* (pp. 29–36).

Berg, N. H. and Caine, N. (1975). *Prediction of natural snowdrift accumulation in alpine areas.* Boulder, Colorado: Department of Geography, University of Colorado.

Box, G. E. P. and Jenkins, G. M. (1976). *Time series analysis: forecasting and control.* Holden-Day.

Buck, A. L. (1981). New Equations for Computing Vapor Pressure and Enhancement Factor. *Journal of Applied Meteorology,* **20**(12), 1527–1532.

Burridge, D. M. and Gadd, A. J. (1974). The Meteorological Office operational 10 level numerical weather prediction model. *U.K. Meteorological Office Technical Notes 12 and 48,* 57.

Cionco, R. M. (1978). Analysis of canopy index values for various canopy densities. *Boundary-Layer Meteorology,* **15**(1), 81–93.

Déry, S. J. and Yau, M. K. (2001). Simulation of an Arctic Ground Blizzard Using a Coupled Blowing Snow–Atmosphere Model. *Journal of Hydrometeorology,* **2**(6), 579–598.

Déry, S. J. and Taylor, P. A. (1996). Some aspects of the interaction of blowing snow with the atmospheric boundary layer. *Hydrological Processes,* **10**(10), 1345–1358.

Essery, R., Pomeroy, J., Parviainen, J., and Storck, P. (2003). Sublimation of Snow from Coniferous Forests in a Climate Model. *Journal of Climate,* **16**(11), 1855.

Finney, E. A. (1934). *Snow control on the highways.* East Lansing: Michigan State College of Agriculture and Applied Science.

Finnish Environment Institute (Suomen ympäristökeskus, SYKE) (2013). Measuring snow water equivalent. http://www.ymparisto.fi/download/noname/%7B671EF5A4-4B52-4E75-B68B-609792E94A70%7D/92726. Accessed: 19 January 2017.

Finnish Meteorological Institute (Ilmatieteen laitos, FMI) (2017a). Climate in Finland. http://en.ilmatieteenlaitos.fi/climate. Accessed: 8 March 2017.

Finnish Meteorological Institute (Ilmatieteen laitos, FMI) (2017b). Lämpötila- ja sadekarttoja vuodesta 1961. http://ilmatieteenlaitos.fi/karttoja-vuodesta-1961. Accessed: 6 March 2017.

Finnish Meteorological Institute (Ilmatieteen laitos, FMI) (2017c). Miten säätä havainnoidaan Ilmatieteen laitoksessa? http://ilmatieteenlaitos.fi/saahavainnot. Accessed: 26 February 2017.

Fleagle, R. G. and Businger, J. A. (1980). *An Introduction to Atmospheric Physics* (2nd ed.)., volume 25 of *International Geophysics Series.* Academic Press.

Greeley, R. and Iversen, J. D. (1985). *Wind as a geological process on Earth, Mars, Venus and Titan,* volume 4 of *Cambridge Planetary Science Series.* Cambridge University Press.

Hedstrom, N. R. and Pomeroy, J. W. (1998). Measurements and modelling of snow interception in the boreal forest. *Hydrological Processes,* **12**(10-11), 1611–1625.

Hellström, R. Å. (2000). Forest cover algorithms for estimating meteorological forcing in a numerical snow model. *Hydrological Processes,* **14**(18), 3239–3256.

Iziomon, M. G., Mayer, H., and Matzarakis, A. (2003). Downward atmospheric longwave irradiance under clear and cloudy skies: Measurement and parameterization. *Journal of Atmospheric and Solar-Terrestrial Physics,* **65**(10), 1107–1116.

Jolliffe, I. T. and Stephenson, D. B. (2003). *Forecast Verification: A Practitioner's Guide in Atmospheric Science*. Wiley.

Kind, R. J. (1981). *Handbook of snow: principles, processes, management & use*, chapter 8 Snow Drifting, (pp. 338–359). Toronto: Pergamon.

Kind, R. J. (1992). One-dimensional aeolian suspension above beds of loose particles – A new concentration-profile equation. *Atmospheric Environment*, **26A**(5), 927–931.

Koch, S. E., desJardins, M., and Kocin, P. J. (1983). An Interactive Barnes Objective Map Analysis Scheme for Use with Satellite and Conventional Data. *Journal of Climate and Applied Meteorology*, **22**(9), 1487–1503.

Kojima, K. (1967). Densification of Seasonal Snow Cover. In Ôura, H. (Ed.), *Physics of Snow and Ice*, volume 1, (pp. 929–952). Institute of Low Temperature Science, Hokkaido University.

Kotlyakov, V. M. (1961). Results of a study of the processes of formation and structure of the upper layer of the ice sheet in eastern Antarctica. In *General Assembly of Helsinki, Symposium on Antarctic Glaciology*, number 55 in International Association of Scientific Hydrology Publications, (pp. 88–99). International Union of Geodesy and Geophysics.

Kunkel, K. E. (1989). Simple Procedures for Extrapolation of Humidity Variables in the Mountainous Western United States. *Journal of Climate*, **2**(7), 656–669.

Kyle, H. L., Hurley, E. J., and Ardanuy, P. E. (1985). The Status of the Nimbus-7 Earth-Radiation-Budget Data Set. *Bulletin of the American Meteorological Society*, **66**(11), 1378–1388.

Lee, L. W. (1975). *Sublimation of snow in a turbulent atmosphere*. PhD thesis, University of Wyoming.

Lehning, M., Völksch, I., Gustafsson, D., Nguyen, T. A., Stähli, M., and Zappa, M. (2006). ALPINE3D: a detailed model of mountain surface processes and its application to snow hydrology. *Hydrological Processes*, **20**(10), 2111–2128.

Leppäranta, M., Makkonen, L., Palosuo, E., and Kuusisto, E. (2001). Geophysics of Snow and Ice in Finland during the 1900s. *Geophysica*, **37**(1-2), 261–285.

Liston, G. E. (1991). *A Computational Model of Two-Phase Turbulent Atmospheric Boundary Layers Containing Blowing Snow*. PhD thesis, Montana State University, Bozeman, Montana.

Liston, G. E. (1995). Local Advection of Momentum, Heat, and Moisture during the Melt of Patchy Snow Covers. *Journal of Applied Meteorology,* **34**(7), 1705–1715.

Liston, G. E. (2016). SnowModel. (Version 9 May 2016) [Computer program]. Available from the author of the program.

Liston, G. E. (2017). Personal communication. 24 January 2017.

Liston, G. E. and Elder, K. (2006a). A Distributed Snow-Evolution Modeling System (SnowModel). *Journal of Hydrometeorology,* **7**(6), 1259–1276.

Liston, G. E. and Elder, K. (2006b). A Meteorological Distribution System for High-Resolution Terrestrial Modeling (MicroMet). *Journal of Hydrometeorology,* **7**(2), 217–234.

Liston, G. E., Haehnel, R. B., Sturm, M., Hiemstra, C. A., Berezovskaya, S., and Tabler, R. D. (2007). Simulating complex snow distributions in windy environments using SnowTran-3D. *Journal of Glaciology,* **53**(181), 241–256.

Liston, G. E. and Hall, D. K. (1995). An energy-balance model of lake-ice evolution. *Journal of Glaciology,* **41**(138), 373–382.

Liston, G. E. and Hiemstra, C. A. (2008). A Simple Data Assimilation System for Complex Snow Distributions (SnowAssim). *Journal of Hydrometeorology,* **9**(5), 989–1004.

Liston, G. E. and Sturm, M. (1998). A snow-transport model for complex terrain. *Journal of Glaciology,* **44**(148), 498–516.

Liston, G. E., Winther, J.-G., Bruland, O., Elvehøy, H., and Sand, K. (1999). Below-surface ice melt on the coastal Antarctic ice sheet. *Journal of Glaciology,* **45**(150), 273–285.

Louis, J.-F. (1979). A parametric model of vertical eddy fluxes in the atmosphere. *Boundary-Layer Meteorology,* **17**(2), 187–202.

McKay, G. A. and Adams, W. P. (1981). *Handbook of snow: principles, processes, management & use,* chapter 1 Snow and Living Things, (pp. 3–31). Toronto: Pergamon.

McKay, G. A. and Gray, D. M. (1981). *Handbook of snow: principles, processes, management & use,* chapter 5 The Distribution of Snowcover, (pp. 153–190). Toronto: Pergamon.

Meek, D. W. and Hatfield, J. L. (1994). Data quality checking for single station meteorological databases. *Agricultural and Forest Meteorology,* **69**(1), 85–109.

Mellor, M. (1965). Blowing snow. *Cold Regions Science and Engineering,* **III**(A3c), 85.

Mellor, M. (1970). A brief review of snowdrifting research. In *Snow Removal and Ice Control Research*, number 115 in Highway Research Board Special Report, (pp. 196–209). National Academy of Sciences.

Merkouriadi, I., Leppäranta, M., and Järvinen, O. (2017). Interannual variability and trends in winter weather and snow conditions in Finnish Lapland. *Estonian Journal of Earth Sciences*, **66**(1), 47–57.

Murray, F. W. (1967). On the Computation of Saturation Vapor Pressure. *Journal of Applied Meteorology*, **6**(1), 203–204.

Owen, P. R. (1964). Saltation of uniform grains in air. *Journal of Fluid Mechanics*, **20**(2), 225–242.

Pomeroy, J. W. (1988). *Wind transport of snow*. PhD thesis, Division of Hydrology, Faculty of Engineering, University of Saskatchewan, Saskatoon, Saskatchewan.

Pomeroy, J. W. and Gray, D. M. (1990). Saltation of snow. *Water Resources Research*, **26**(7), 1583–1594.

Pomeroy, J. W. and Gray, D. M. (1995). *Snowcover accumulation, relocation and management*. Number 7 in NHRI science report. Saskatoon : National Hydrology Research Institute.

Pomeroy, J. W., Gray, D. M., Hedstrom, N. R., and Janowicz, J. R. (2002). Prediction of seasonal snow accumulation in cold climate forests. *Hydrological Processes*, **16**(18), 3543–3558.

Pomeroy, J. W., Gray, D. M., and Landine, P. G. (1993). The Prairie Blowing Snow Model: characteristics, validation, operation. *Journal of Hydrology*, **144**(1-4), 165–192.

Pomeroy, J. W. and Male, D. H. (1986). Physical modelling of blowing snow for agricultural properties. In Steppuhn, H. and Nicholaichuk, W. (Eds.), *Proceedings, Snow Management for Agriculture Symposium, 1985, Swift Current, Saskatchewan*, volume 120 of *Great Plains Agricultural Council Publication*, (pp. 73–108)., Lincoln, Nebraska. Water Studies Institute.

Pomeroy, J. W., Marsh, P., and Gray, D. M. (1997). Application of a distributed blowing snow model to the Arctic. *Hydrological Processes*, **11**(11), 1451–1464.

Pomeroy, J. W., Parviainen, J., Hedstrom, N., and Gray, D. M. (1998). Coupled modelling of forest snow interception and sublimation. *Hydrological Processes*, **12**(15), 2317–2337.

Pomeroy, J. W. and Schmidt, R. A. (1993). The Use of Fractal Geometry in Modeling Intercepted Snow Accumulation and Sublimation. In *Proceedings of the 50th Eastern Snow Conference, Quebec City, Quebec, Canada*, volume 50, (pp. 1–10).

Price, A. G. and Dunne, T. (1976). Energy balance computations of snowmelt in a subarctic area. *Water Resources Research*, **12**(4), 686–694.

Rasmus, S. (2013). Spatial and Temporal Variability of Snow Bulk Density and Seasonal Snow Densification Behavior in Finland. *Geophysica*, **49**(1-2), 53–74.

Rogers, R. R. (1979). *A Short Course in Cloud Physics*. Oxford ; New York : Pergamon Press.

Ryan, B. C. (1977). A Mathematical Model for Diagnosis and Prediction of Surface Winds in Mountainous Terrain. *Journal of Applied Meteorology*, **16**(6), 571–584.

Schmidt, R. (1991). Sublimation of snow intercepted by an artificial conifer. *Agricultural and Forest Meteorology*, **54**(1), 1–27.

Schmidt, R. A. (1972). Sublimation of Wind-Transported Snow – A Model. *USDA Forest Service Research Paper*, **RM-90**, 1–24.

Schmidt, R. A. (1982a). Properties of blowing snow. *Reviews of Geophysics*, **20**(1), 39–44.

Schmidt, R. A. (1982b). Vertical profiles of wind speed, snow concentration, and humidity in blowing snow. *Boundary-Layer Meteorology*, **23**(2), 223–246.

Sicart, J. E., Pomeroy, J. W., Essery, R. L. H., Hardy, J., Link, T., and Marks, D. (2004). A Sensitivity Study of Daytime Net Radiation during Snowmelt to Forest Canopy and Atmospheric Conditions. *Journal of Hydrometeorology*, **5**(5), 774–784.

Simojoki, H. J. (1978). *The history of geophysics in Finland 1828-1918*. Number 5b in The History of Learning and Science in Finland 1828-1918. Helsinki: Societas Scientiarum Fennica.

Sjöblom, H. (2015). *Hydrologisen seurannan kenttätöiden toimintakäsikirja*, chapter 4. Lumilinjamittaukset, (pp. 36–46). Hydrological Monitoring Group, Finnish Environment Institute (Suomen ympäristökeskus, SYKE) / Freshwater Centre.

Sjöblom, H. (2016). Personal communication. 21 December 2016.

State Forest Enterprise (Metsähallitus) (2017). Natural Features of Urho Kekkonen National Park. http://www.nationalparks.fi/urhokekkonennp/nature. Accessed: 23 February 2017.

Sturm, M., Holmgren, J., König, M., and Morris, K. (1997). The thermal conductivity of seasonal snow. *Journal of Glaciology*, **43**(143), 26–41.

Tabler, R. D. (1975). Estimating the transport and evaporation of blowing snow. In *Symposium on Snow Management on the Great Plains (Bismarck, North Dakota, July 29, 1975)*, number 73 in Great Plains Agricultural Council Publication, (pp. 85–104).

Tabler, R. D. (1980). Geometry and density of drifts formed by snow fences. *Journal of Glaciology*, **26**(94), 405–419.

Thornton, P. E., Running, S. W., and White, M. A. (1997). Generating surfaces of daily meteorological variables over large regions of complex terrain. *Journal of Hydrology*, **190**(3-4), 214–251.

Thorpe, A. D. and Mason, B. J. (1966). The evaporation of ice spheres and ice crystals. *British Journal of Applied Physics*, **17**(4), 541–548.

Walcek, C. J. (1994). Cloud Cover and Its Relationship to Relative Humidity during a Springtime Midlatitude Cyclone. *Monthly Weather Review*, **122**(6), 1021–1035.

Wallace, J. M. and Hobbs, P. V. (1977). *Atmospheric Science: An Introductory Survey*. Academic Press.

Walton, T. L. (1996). Fill-in of missing data in univariate coastal data. *Journal of Applied Statistics*, **23**(1), 31–40.

# Appendix A

# Meteorological observations

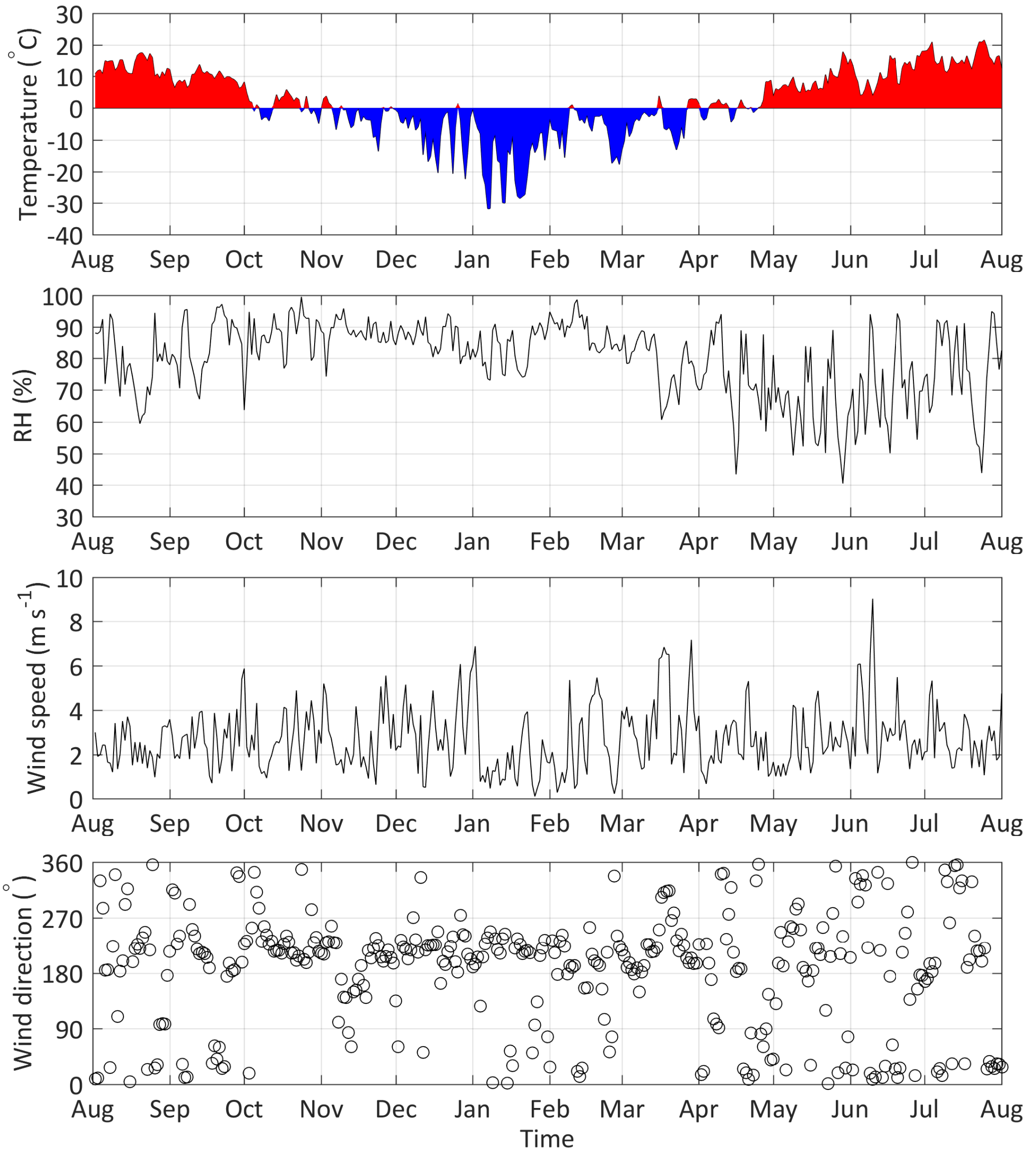

**Figure A.1:** Observed atmospheric forcing at Inari Ivalo lentoasema (airport) AWS-(a) during the winter 2015-2016. To clarify the figures only the daily values are shown.

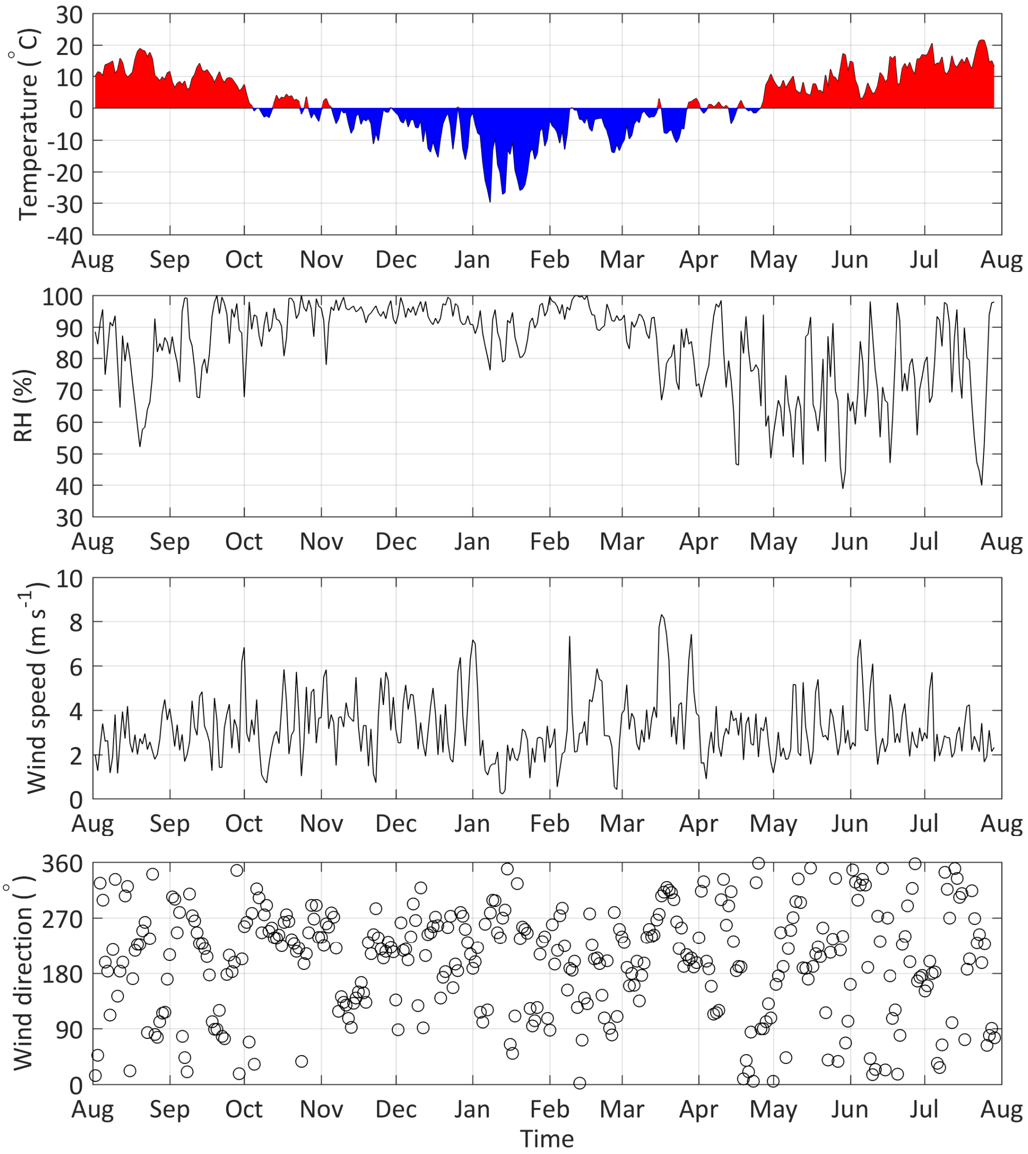

**Figure A.2:** Observed atmospheric forcing at Inari Raja-Jooseppi AWS-(b) during the winter 2015–2016. To clarify the figures only the daily values are shown.

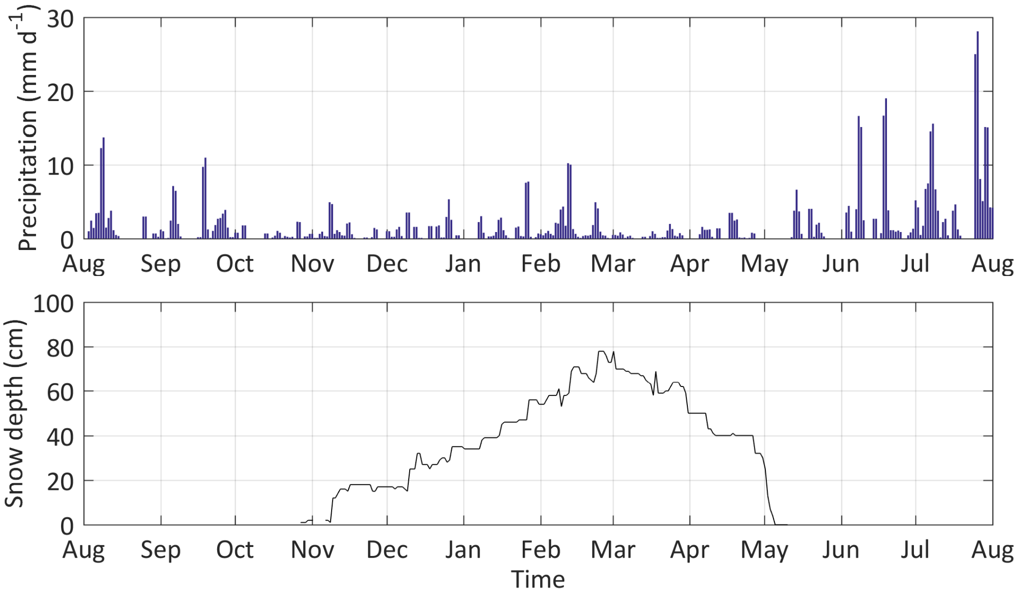

**Figure A.3:** Observed atmospheric forcing at Inari Raja-Jooseppi Kontiojärvi manual weather station (c) during the winter 2015–2016. Only daily values of precipitation and snow depth were available from this station.

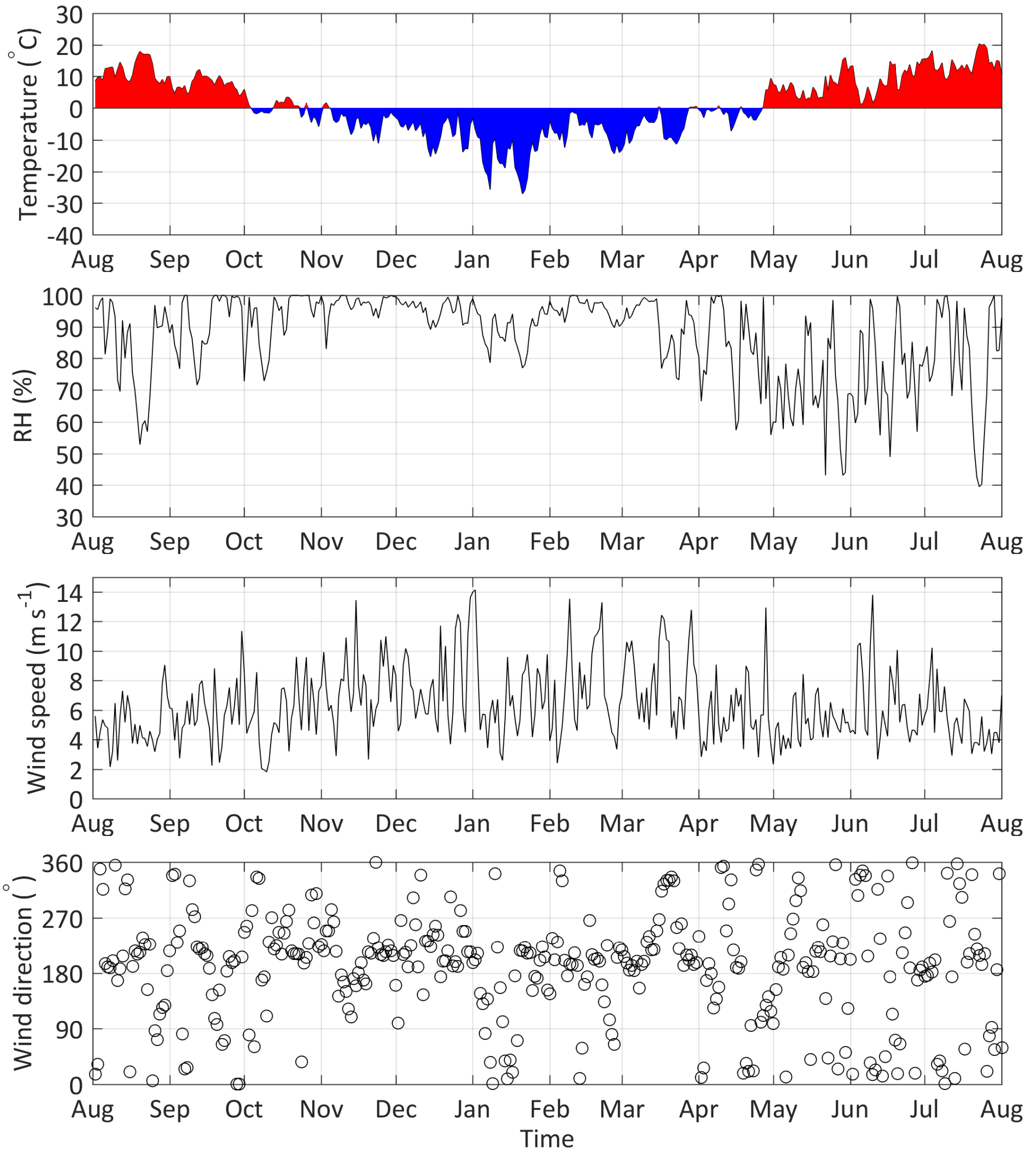

**Figure A.4:** Observed atmospheric forcing at Inari Saariselkä Kaunispää AWS-(d) during the winter 2015–2016. To clarify the figures only the daily values are shown.

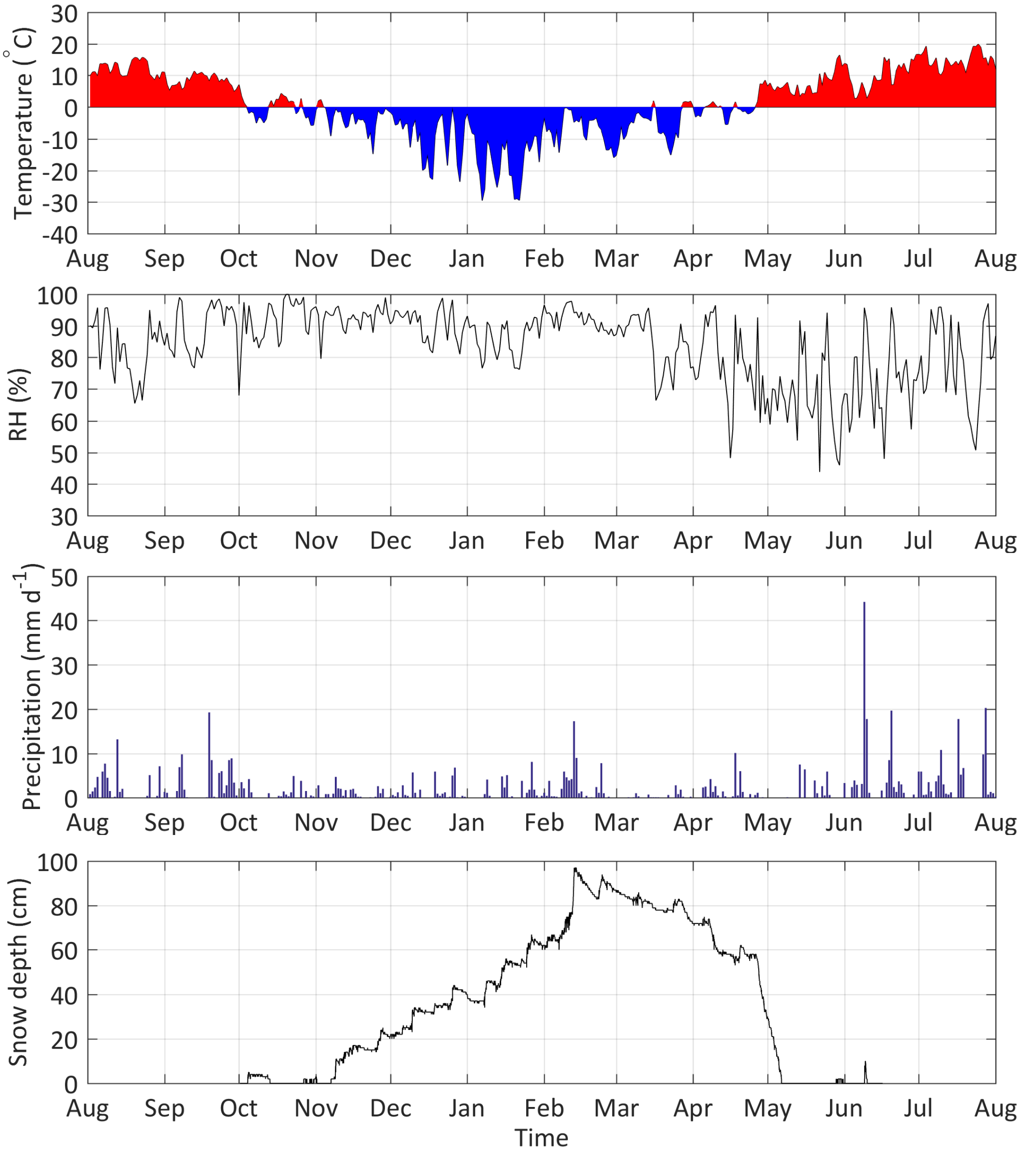

**Figure A.5:** Observed atmospheric forcing at Inari Saariselkä matkailukeskus (tourist attraction) AWS-(e) during the winter 2015–2016. To clarify the figures only the daily values are shown.

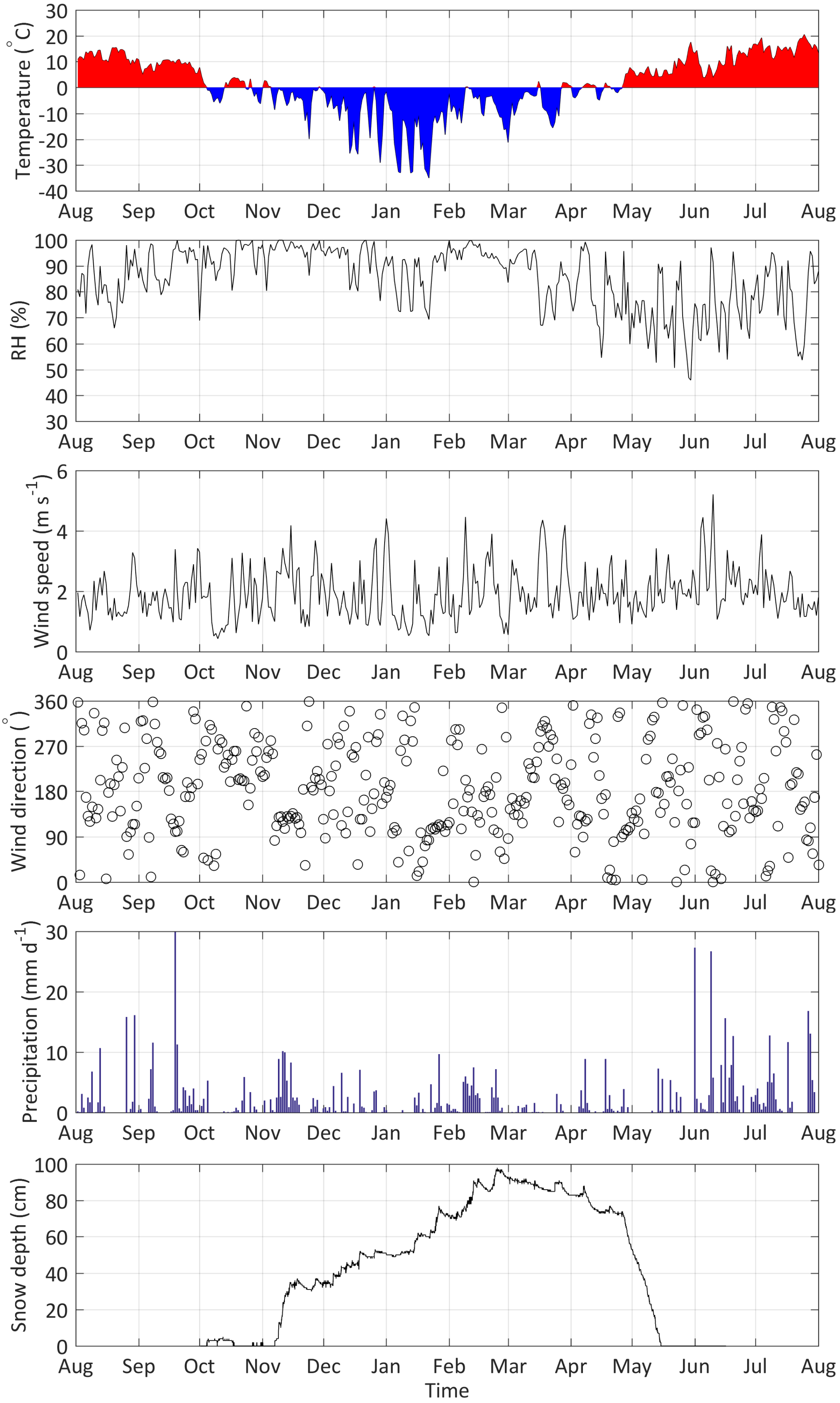

**Figure A.6:** Observed atmospheric forcing at Sodankylä Vuotso AWS-(f) during the winter 2015–2016. To clarify the figures only the daily values are shown.